

**STRUCTURAL AND MOLECULAR REGULATORS OF EMBRYONIC TISSUE
STIFFNESS**

by

Joseph Hany Shawky

B.S. in Biomedical Engineering, Rensselaer Polytechnic Institute, 2010

M.Eng. in Biomedical Engineering, Cornell University, 2011

Submitted to the Graduate Faculty of
Swanson School of Engineering in partial fulfillment
of the requirements for the degree of
Doctor of Philosophy

University of Pittsburgh

2017

UNIVERSITY OF PITTSBURGH
SWANSON SCHOOL OF ENGINEERING

This dissertation was presented

by

Joseph Hany Shawky

It was defended on

September 5, 2017

and approved by

Adam Feinberg, PhD, Associate Professor, Materials Science & Engineering and Biomedical Engineering, Carnegie Mellon University

Partha Roy, PhD, Associate Professor, Departments of Bioengineering, Cell Biology, and Pathology

James H-C. Wang, Professor, PhD, Departments of Orthopaedic Surgery and Bioengineering

Dissertation Director: Lance Davidson, PhD, Professor, Departments of Bioengineering, Developmental Biology and Computational and Systems Biology

Copyright © by Joseph Hany Shawky

2017

STRUCTURAL AND MOLECULAR REGULATORS OF EMBRYONIC TISSUE STIFFNESS

Joseph Hany Shawky, Ph.D.

University of Pittsburgh, 2017

Embryonic development involves large scale tissue movements that construct complex three-dimensional tissue structures, governed by basic physical principles. Fine-grained control of mechanical properties and force production is critical to the successful placement of tissues and organs within the embryo. Cell generated forces and passive mechanical properties not only physically construct tissue structures, but may also provide feedback to instruct cell behavior, remodel extracellular matrix, and regulate intercellular adhesions.

Early embryos of the frog *Xenopus laevis* provide a dramatic example of these physical processes with rapidly changing mechanical properties, increasing in elastic modulus by six-fold to 80 Pascal over eight hours as germ layers and the central nervous system are formed. These physical changes coincide with emergence of complex anatomical structures, several rounds of cell division and remodeling of the cytoskeleton.

We analogize the mechanics of embryonic tissues to closed-cell foams to predict the influence of tissue architecture, cell size, and cell cortex on bulk tissue mechanics. The Cellular Solids Model (CSM) relates bulk stiffness of a solid-foam to the unit-size of individual cells, their microstructural organization, and their material properties. We confirmed the central assumption of the CSM, that tissue modulus does not depend on embedded structural elements by engineering and mechanically testing a tissue devoid of large coherent 3D structures. To test the role of cell size we generated large cells by arresting the cell cycle and generated small cells by inhibiting a developmentally regulated cell cycle inhibitor. Tissues with lower and higher cell

density confirm predictions of the CSM but are only responsible for a modest 20% increase in stiffness from early to late neurulation. To modulate the composition and modulus of the "cell-wall" we enhanced and diminished cortical F-actin cross-linking. We found that levels of crosslinking regulate bulk tissue modulus. Our results indicate that large scale architecture and cell size are not likely to influence the bulk passive mechanical properties of early embryonic or progenitor tissues. Our findings suggest that regulation of F-actin cortical thickness, density, and integrity plays a central role in regulating the physical mechanics of embryonic multicellular tissues.

TABLE OF CONTENTS

PREFACE.....	XIII
1.0 INTRODUCTION.....	1
1.1 MECHANICS OF MORPHOGENESIS.....	1
1.1.1 Tissue movements during development depend on mechanics	1
1.1.2 Developmental biomechanics in <i>Xenopus laevis</i>	2
1.2 CELLULAR SOLIDS MODEL	6
1.3 GOALS AND SPECIFIC AIMS OF STUDY	9
1.4 SIGNIFICANCE.....	11
2.0 ADHESION MECHANICS IN DEVELOPMENT.....	14
2.1 TISSUE MECHANICS AND ADHESION DURING EMBRYO DEVELOPMENT.....	14
2.1.1 Introduction	14
2.1.2 Structural and mechanical function of adhesions during development.	17
2.1.3 Biophysical descriptions of adhesion	18
2.1.4 Formal definitions of the mechanics of adhesion.	20
2.1.5 Modulating Adhesions and Mechanics at Different Scales	23
2.1.5.1 At the single molecule scale.....	24
2.1.5.2 Scaling-up: from single-cells to multiple cells and aggregates	26

2.1.5.3	Sheets, aggregates, and assembly of large multi-tissue structures	30
2.1.6	New efforts to extend mechanics of molecular adhesion to tissue scales: molecular strain and tension sensors.....	34
2.1.7	Mechanics and adhesion in the embryo	35
2.1.8	Review Summary.....	39
2.2	RESULTS.....	41
2.2.1	Cdh3-ΔE expression reduces cortical actin and reduces tissue stiffness	41
3.0	TISSUE ARCHITECTURE & MECHANICAL PROPERTIES	43
3.1	INTRODUCTION	43
3.2	RESULTS.....	44
3.2.1	Embryonic dorsal tissues stiffen 150% during neurulation.....	44
3.2.2	Architecture changes in dorsal isolate are concurrent with tissue stiffening.....	46
3.2.3	Architecture of the dorsal isolate is disrupted after 'scrambling.'	47
3.2.4	Scrambled tissues parallel development of native tissue, differentiating and assembling laminin and fibrillin fibrils.....	51
3.2.5	Elastic Modulus depends on stage, not architecture	54
3.2.6	Native architecture is required for mechanical maturation.....	55
3.3	DISCUSSION.....	56
3.4	EXPERIMENTAL PROCEDURES.....	58
3.4.1	Tissue Dissociation and Reaggregation	58
3.4.2	Immunohistochemistry	59
3.4.3	Live cell and tissue imaging.....	59

3.4.4	Mechanical testing of tissue explants.....	60
4.0	CELL SIZE ON TISSUE MECHANICAL PROPERTIES	61
4.1	INTRODUCTION	61
4.2	RESULTS.....	61
4.2.1	Lower cell density reduces the modulus of dorsal isolates.	61
4.2.2	Increased cell density increases the modulus of dorsal isolates.	65
4.3	DISCUSSION.....	67
4.4	EXPERIMENTAL PROCEDURES.....	68
4.4.1	Cell Cycle Inhibition to Generate Larger Cells.....	68
4.4.2	Nuclear density measurements.....	69
4.4.3	Microinjection of morpholino	70
4.4.4	Mechanical testing of tissue explants.....	70
5.0	F-ACTIN REGULATION DURING DEVELOPMENT	71
5.1	INTRODUCTION	71
5.2	RESULTS.....	75
5.2.1	Endogenous F-actin cortex intensity and stability increase during neurulation.....	75
5.2.2	F-actin Cortex thickness unchanged during neurulation	78
5.2.2.1	Limitations of Cortex Thickness Measurement.....	80
5.2.3	ACTN1 crosslinking regulates dorsal axis stiffness	84
5.3	DISCUSSION.....	90
5.4	EXPERIMENTAL PROCEDURES	91
5.4.1	F-actin staining and intensity measurement	91

5.4.2	Fluorescence Recovery After Photobleaching	92
5.4.3	Actinin mRNA constructs.....	93
5.4.4	F-actin Cortex Thickness Measurement	94
5.4.5	Mechanical testing of tissue explants.....	95
6.0	GENERAL METHODS	96
6.1	EMBRYOS AND MICROSURGERY	96
6.2	BIOMECHANICAL TESTING- NNFMD.....	97
7.0	SUMMARY AND CONCLUSIONS	100
7.1	SUMMARY OF FINDINGS.....	100
7.2	SIGNIFICANCE OF FINDINGS	102
7.3	FUTURE DIRECTIONS	103
	APPENDIX A. PROTOCOLS AND IMAGE ANALYSIS	107
	APPENDIX B. EPITHELIAL BLASTOPORE CLOSURE STRAIN MAPPING	121
	APPENDIX C. NUCLEI TRACKING IN SPREADING ANIMAL CAP TISSUES	129
	APPENDIX D. TISSUE STRAIN ENERGY	140
	BIBLIOGRAPHY	143

LIST OF TABLES

Table 1. Techniques to measure molecular, cell and tissue level adhesion mechanics.	41
--	----

LIST OF FIGURES

Figure 1. Tissue movements during <i>Xenopus</i> gastrulation.....	4
Figure 2: Structural elements at the tissue, cell and molecular scale may be contributing to bulk tissue mechanical properties.	6
Figure 3. Mechanical properties of embryonic tissues can be modeled as cellular solids.....	8
Figure 4. Biophysical analysis of adhesion at the molecular scale.....	21
Figure 5. Strategies for measuring adhesion at the cell scale.	28
Figure 6. Investigating the biophysics of adhesion at the tissue scale.....	32
Figure 7. How molecular FRET tension sensors might probe the mechanics of adhesion at cell junctions in tissues under compression.....	35
Figure 8. Roles of adhesion at the embryo scale.	37
Figure 9. Dominant negative cadherin reduces cortical actin and tissue stiffness.....	42
Figure 10. Tissue architecture changes during neurulation.	44
Figure 11. Dorsal tissues stiffen 150% during neurulation.....	45
Figure 12. Changes in mesoderm cell shape during neurulation.	47
Figure 13. Native architecture is disrupted in “scrambled” tissues.	49
Figure 14. Scrambled tissues do not undergo bulk morphogenetic movements.....	50
Figure 15. Scrambled tissues synthesize fibrillin and laminin.	52
Figure 16. Scrambled tissues differentiate somites.....	53
Figure 17. Mesoderm cells in scrambled tissues undergo stereotypic protrusive activity.....	54
Figure 18. Elastic Modulus of scrambled tissues unchanged from stage-matched dorsal isolates.	55

Figure 19. Aged scrambled tissues stiffen, however not to the extent of native tissues.....	56
Figure 20. Cell cycle inhibition using HUA doesn't alter bulk architecture or F-actin abundance	63
Figure 21. HUA treatment reduces cell density in mesoderm tissues and decreases bulk modulus.	64
Figure 22. Wee2 depletion doesn't alter F-actin abundance.....	66
Figure 23. Wee2 depletion increases nuclear density and tissue modulus.	67
Figure 24. Examples of common F-actin cross-linkers	74
Figure 25. F-actin cross-linkers expressed during gastrulation and neurulation in <i>X. laevis</i>	74
Figure 26. F-actin enhanced and stabilized in mesoderm during neurulation.	76
Figure 27. Rock inhibition reduces modulus of stage 14 and 21 dorsal isolates.....	78
Figure 28. Scatter labeling of plasma membrane and F-actin reporters within dorsal isolates. ...	81
Figure 29. Measuring cortex thickness within mosaically labeled tissues.	82
Figure 30. Cortex thickness unchanged within mesoderm.	83
Figure 31. Theoretical effect of cortex angle skew on relative positions of actin and membrane signal.....	84
Figure 32. Δ ABD-actinin rescues blastopore closure delay caused by overexpression of α -actinin-1.	87
Figure 33. α -actinin-1 overexpression increases cortex stability in animal cap epithelium.....	88
Figure 34. α -actinin-1 cross-linking affects F-actin intensity and tissue modulus.	89
Figure 35. Fluorescence Recovery After Photo-bleaching (FRAP) Experiment.....	93
Figure 36. nano-Newton Force Measurement Device (nNFMD).	97
Figure 37. Strain Mapping of Blastopore Closure.....	124
Figure 38. Mean strain values in 4 embryos over blastopore closure.....	125
Figure 39. Strain patterns around the blastopore during gastrulation.	127
Figure 40. Cell motility within animal cap tissue spreading on 3D surfaces.	131
Figure 41. Recoil of dorsal isolates after release from constraint.....	142

PREFACE

I would like to thank the members of my dissertation committee, Dr. Adam Feinberg, Dr. Partha Roy and Dr. James H-C. Wang, for their time and constructive feedback throughout my research. In particular, I'd like to thank my PhD advisor Dr. Lance Davidson, whose patience and guidance throughout my project has been invaluable. Under Dr. Davidson's mentorship I have grown not only as a researcher but also as a person and I am grateful for this training. I'd also like to thank the Department of Bioengineering, particularly Dr. Sanjeev Shroff and Nick Mance. Dr. Shroff has always been a 'chair for the students' and has supported me on several initiatives within the department and personally in my professional career. Nick makes the Department of Bioengineering run and is a source of knowledge I have relied on throughout graduate school.

I would also like to thank the members of the Davidson Lab for helpful feedback, troubleshooting tips and an amazingly friendly lab environment. Steve, Carsten, Callie, Holley, Tim, Hye Young, Fatima, Lin, Jiho, Melis, Rafey, Uma, Ya-Wen and Deepthi – I cherish your friendship and hope to remain in touch with you all for years to come. A special thanks goes to Deepthi who entered the Davidson lab at the same time and whose moral support and friendship I leaned on during the past six years. Also, special thanks to Carsten not only for his scientific expertise but also for his mentorship and the many great conversations we've had throughout the years.

Completing a PhD would not be possible without a loving and supportive family. To my mom, dad and sister – you have all inspired and taught me in different ways and without your unwavering encouragement and support my entire life it's obvious I could have never been here writing this document today. Love you all. My deepest gratitude goes to my best friend and wife, Caroline for being there day in day out through all the ups and downs of grad school. Caroline – thank you for your unending love and for the countless sacrifices you made to be by my side.

Finally, I'd like to thank the many great friends I made in Pittsburgh. Being from upstate New York, I didn't know what to expect of the Steel City, however 6 years later I am in love with Pittsburgh mainly because of the people I've met. You all have a place in my heart.

1.0 INTRODUCTION

1.1 MECHANICS OF MORPHOGENESIS

1.1.1 Tissue movements during development depend on mechanics

Embryo development is an inherently physical process which depends on the coordination of biochemical and physical patterning (Miller and Davidson 2013). To transform from a sphere of cells into a cylinder requires anisotropic force production and/or stiffness regulation. The active cell-generated forces and passive mechanical properties not only physically construct tissue structures, but may also provide feedback to instruct cell behavior, remodel extracellular matrix, and regulate intercellular adhesions. Additionally, cell migration, cell shape and cell adhesion are not only controlled through biochemical signaling but also through biomechanical cues (Lauffenburger and Horwitz 1996; Paluch and Heisenberg 2009; Miller and Davidson 2013).

To understand how cell generated forces work to deform tissues, it is critical to measure tissue mechanical properties. Measurements of mechanical properties have been made in many developmental model organisms. Laser ablation studies in *Drosophila* show that epithelial tissue tension is spatially regulated and plays a role in early processes such as mesoderm invagination, germ band elongation, and dorsal closure, as well as a diverse set of epithelial morphogenetic movements at later stages (Rauzi et al. 2015). Direct measurements of the epithelial blastula wall

in sea urchin revealed that apical ECM can also be a major contributor to tissue modulus (Davidson et al. 1999) that can place physical constraints on the contribution of cellular mechanisms to invagination (Davidson et al. 1995). Studies using zebrafish embryo reaggregates have implicated a role for tissue surface tension, as controlled by cell-cell adhesion interactions, in positioning germ layers within the embryo (Krens et al. 2011; Krieg et al. 2008; Maitre et al. 2012). Perturbing surface mechanics by modulating cadherin expression in aggregates of zebrafish ectoderm cells can also disrupt normal sorting processes that position epidermal cells on the outer surface of the embryo (Schotz et al. 2008; Manning et al. 2010).

Amphibian and avian embryos provide unique opportunities to study the role of mechanics during development due advanced microsurgical maneuvers and rapid wound healing processes. Mechanical properties of embryonic axolotyl epithelia are spatially patterned across the early embryo surface and temporally patterned over late gastrula and neural stages (Wiebe and Brodland 2005). Forces of neurulation have been measured directly in several species of newts (Selman 1955, 1958). Cell contractility and proliferation during avian organogenesis have been suggested to play a direct mechanical role in heart remodeling (Taber et al. 2010), head fold formation (Varner et al. 2010), gut tube coiling (Savin et al. 2011; Nerurkar et al. 2017), and villus formation in the intestine (Shyer et al. 2015).

1.1.2 Developmental biomechanics in *Xenopus laevis*

The mechanics of embryos of the African claw-toed frog *Xenopus laevis* have been the most fully studied species through gastrulation, neurulation, heart forming, and tailbud elongation stages. The embryo before gastrulation consists of a spherical ball of cells with the vegetal hemisphere containing prospective endoderm, the animal hemisphere containing prospective

ectoderm, and an annular strip spanning the equator consisting of prospective endoderm, mesoderm, and ectoderm referred to as the marginal zone. During gastrulation and neurulation, the embryo changes form to achieve very specific architectures (i.e. segmentation cavities and neural folds) with distinct tissue boundaries (Figure 1A-B). The marginal zone is reshaped during gastrulation through the action of multiple modes of cell movement such as radial (Figure 1A') and mediolateral (Figure 1B') intercalation, and bottle cell contraction (Keller et al. 2003; Davidson 2008). The forces generated by these multiple cellular modes are integrated mechanically to drive tissue movements such as ectoderm epiboly, and involution and convergent extension of the marginal zone into dorsal axial tissues comprised of three germ layers: 1) neural plate ectoderm along the outer surface of the embryo, 2) mesoderm consisting of a central notochord flanked by presomitic mesoderm, and 3) endoderm facing the archenteron. The general positions of the germ layers are preserved as neurulation progresses, however each germ layer, particularly the neural plate ectoderm and presomitic mesoderm are reshaped creating new tissue architecture and cell shapes.

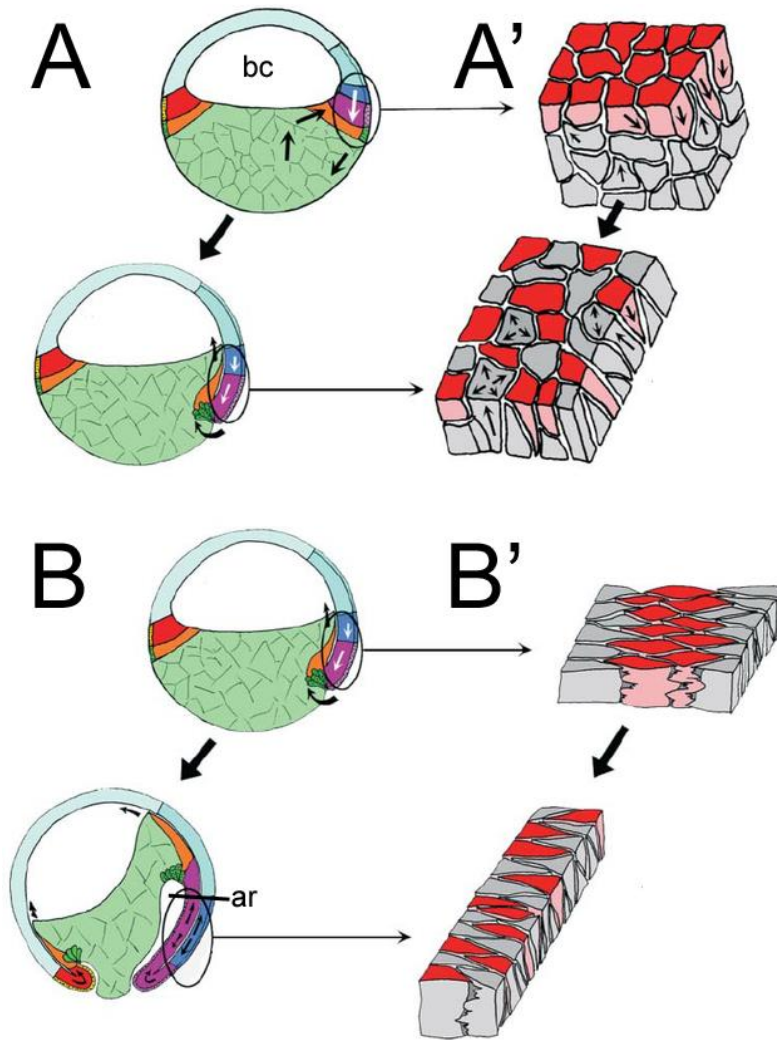


Figure 1. Tissue movements during *Xenopus* gastrulation.

A) At the beginning of gastrulation (stage 10), the marginal zone undergoes involution (black arrows), thinning and extension (white arrows). Prospective fates: epidermis (light blue); forebrain (blue); spinal cord (dark blue), superficial endoderm-bottle cells (green); vegetal endoderm (light green); notochord (magenta); somitic mesoderm (red); leading edge mesendoderm (orange); blastocoel (bc). A') Tissue thinning is driven by radial intercalation of deep cells to the surface of the embryo. B) After mid-gastrulation, the involuted marginal zone along with the entire dorsal axis undergoes convergent extension (black arrows), archenteron (ar). B') Convergent extension is driven by mediolateral cell intercalation (B'). Figure reproduced from (Keller et al. 2003).

Early dorsal tissues within frog embryos are extremely soft but display anisotropic modulus from the earliest stages of gastrulation (Moore et al. 1995) and exhibit a six-fold increase in residual Young's modulus from early gastrula to tailbud stages (Zhou et al. 2009). Ectoderm isolates and aggregates can appear fluid-like but exhibit elastic behaviors needed to guide morphogenesis (Luu et al. 2011). The modulus of ventral tissues also increase after neurulation as the heart and other ventral organs form (Jackson et al. 2017). Large-scale structures such as the notochord also play a role, for instance, as the tailbud embryo straightens and lengthens the vacuoles within the collagen sheathed notochord swell (Adams et al. 1990; Koehl et al. 2000; Murakami et al. 2017). Thus, changes in both material composition, e.g. cytoskeleton, and large-scale multicellular structures such as the notochord can contribute to both the bulk modulus and morphogenesis of the *Xenopus* embryo.

Little is known about the role of cell- or tissue-scale features on modulus or whether these features contribute to changes in modulus. In this study, we test the contribution of tissue-, cell-, and subcellular-scale structures to the changing modulus of the *Xenopus* embryonic dorsal axis during elongation (Figure 2). We adopt a formal theoretical framework known as the Cellular Solids Model (CSM)(Gibson and Ashby 1997) to *Xenopus* embryonic tissues.

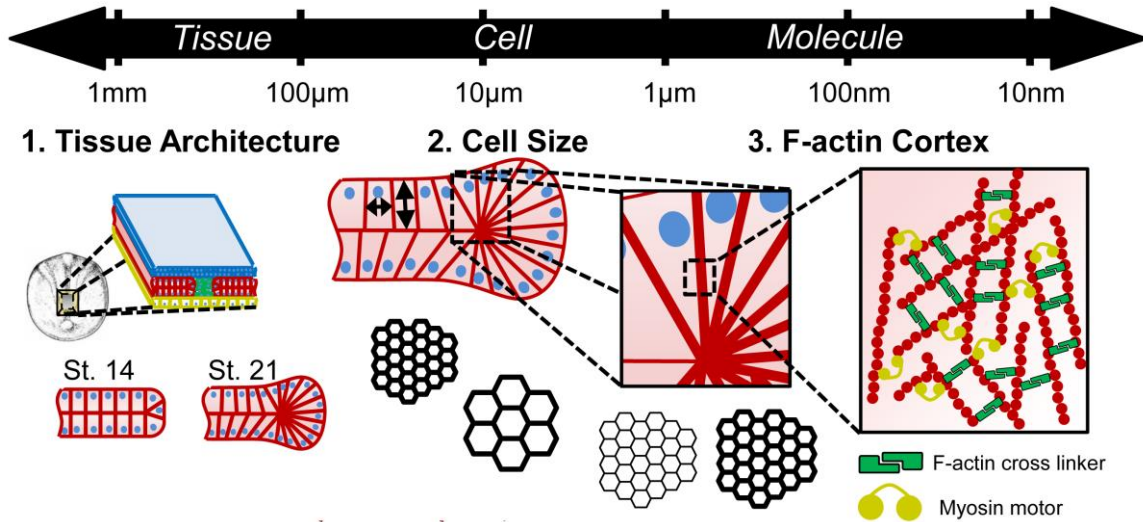


Figure 2: Structural elements at the tissue, cell and molecular scale may be contributing to bulk tissue mechanical properties.

1.2 CELLULAR SOLIDS MODEL

The Cellular Solids Model (CSM) (Gibson and Ashby 1988) was developed to characterize the bulk mechanical properties of open- and closed-cell materials, both synthetic and biological in origin, based on the microstructure of the component cells. Cellular solids can be two dimensional arrays of polygons, known as honeycombs or polyhedral cells packed tightly in three-dimensional space, known as foams. Foams can be open-celled with interconnected cells or closed-celled with membranes enclosing each cell from neighbors. Solid foams differ from liquid foams by their structure and mode of deformation. In solid foams, struts can bear load by bending and stretching however in liquid foams the membranes enclosing cells are thin and only stretch under loads. Liquid foams behave elastically under small deformations, governed by the surface tension of the membrane and cell size and behave plastically under larger deformations

that induce topological changes (Weaire and Hutzler 2001). Liquid foams are often used to describe cell shapes and rearrangement within 2D epithelia (Hayashi and Carthew 2004; Farhadifar et al. 2007). Deformation in solid foams depends on whether cells are open or closed. In open-cell solid foams, bulk compression is transmitted across the material through cell-wall bending. In closed-cell solid foams containing a gas, cell volumes decrease, resulting in increased pressure within cells. Closed-cell solid foams filled with an incompressible fluid within cells are different in that cell volume is conserved by cell-wall stretching which compensates for volume reductions caused by cell wall bending. In both cases, the cell edges bend and extend or contract and the membranes enclosing cells stretch. According to CSM, the basic mechanics of cellular tissues should be like closed-cell foams (Figure 3). The Young's modulus of a closed-cell foam filled with an incompressible liquid is as follows:

$$\frac{E^*}{E_s} = \left(\frac{\rho^*}{\rho_s}\right) \left[1 + \frac{\rho^*}{\rho_s}\right], \quad (1)$$

where E^* = bulk tissue modulus, E_s and ρ_s = material modulus and density, respectively, and ρ^* = density of the foam as calculated by:

$$\rho^* = \frac{[Actin\ cortex\ volume]}{unit\ volume} = \frac{[(SA_c)(\#\ of\ cell)(t)]}{unit\ volume} \quad (2)$$

where SA_c = surface area of a cell and t = cell wall thickness. In our case, we will control ρ^* by modulating the number of cells per volume, which is directly proportional to cell size.

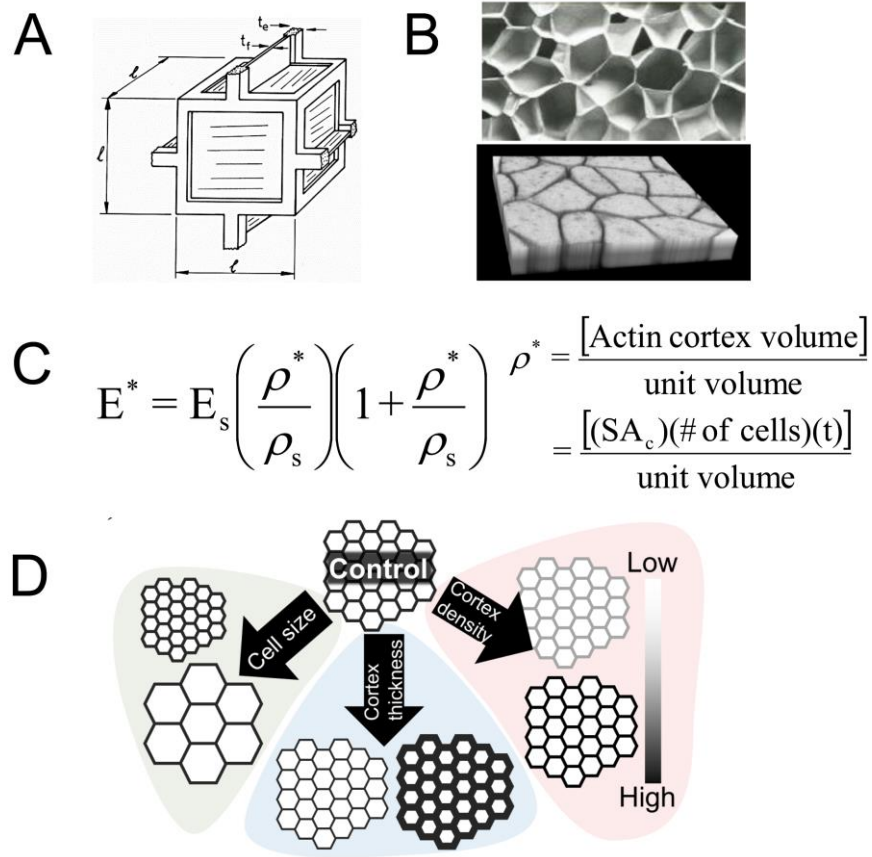


Figure 3. Mechanical properties of embryonic tissues can be modeled as cellular solids.

We utilize the Cellular Solids Model (CSM) to predict how changes in properties at each size scale regulate bulk mechanical properties. A) Schematic of the structure of a closed-cell foam. Reproduced from (Gibson and Ashby 1988). B) Image of a synthetic polyethylene foam (top; reproduced from (Gibson and Ashby 1988)) compared with a 3D projected *Xenopus laevis* embryonic neural plate tissue (bottom). C) Central equation to describe the mechanics of a closed-cell foam with an incompressible fluid. Individual variables are described in the text. D) We utilize CSM to make and test predictions on the contribution of cell size and cortex composition to bulk modulus of embryonic tissues.

1.3 GOALS AND SPECIFIC AIMS OF STUDY

Little is known about the tissue-, cell-, and molecular-scale mechanisms that regulate tissue mechanical properties during gastrulation and neurulation, when the dorsal axis dramatically stiffens. The goal of this research is to identify the structural and molecular factors regulating embryonic tissue stiffness. Regulators of mechanical properties may be categorized by their impact on three different scales: 1) changes in the composition of materials, such as newly assembled extracellular matrix or F-actin cortex that composes the embryo, 2) changes at the level of the cellular architecture, such as the size and shape of cells, and, 3) changes within the tissue microanatomy, such as laminar cell sheets or the ECM wrapped notochord. In *Xenopus*, studies have focused primarily on composition by perturbing ECM, F-actin, microtubules, and myosin contractility and found that F-actin and contractile myosin II account for approximately 60% of the residual Young's modulus at stage 13 (Zhou et al. 2010; Zhou et al. 2009).

During gastrulation and neurulation, the embryo changes form to achieve very specific architectures with distinct tissue boundaries. Structural modulators of tissue stiffness may include changes in cell size, cell shape, overall tissue shape and/or ECM distribution. By perturbing both, cell/tissue architecture and activity levels of potential molecular regulators of F-actin cortex, we aim to pinpoint the factors contributing to tissue stiffening.

We utilize the CSM to make predictions on the contribution of tissue-, cell-, and subcellular-scale structures to the changing modulus of the *Xenopus* embryonic tissues. Features such as cell size and 'cell-wall' composition are major contributors to the bulk modulus of 3D foams; therefore, we set out to determine if these features are also important for embryonic tissue stiffness. A central assumption of the CSM is that bulk properties of tissues are determined by the mechanics of individual constituent cells and not by extracellular features or any large-scale

architectures. In this study, we begin by testing the assumption of the CSM that tissue architecture does not contribute to bulk modulus and proceed to test how cell size and F-actin cortex contribute to bulk mechanics of neurula stage embryonic tissues.

Aim 1: Evaluate the contribution of tissue architecture on tissue stiffness

Hypothesis: Tissue architecture is critical for maintaining tissue modulus.

Architecture can be defined as a unifying or coherent form or structure critical for proper function. In the case of embryonic tissues, we define architecture as the assembly of tissue shapes and surrounding extracellular matrix that make up a 3D tissue. During stages of stiffening, the dorsal axis undergoes dramatic architectural changes, specifically neural plate folding and mesoderm reshaping to form thicker PSM tissues. The contribution of these large multi-cell anatomical features to bulk tissue mechanical properties is unknown. The goal of this aim is to generate and mechanically test tissues devoid of large scale architectural features composed of cells of the same developmental stage.

Aim 2: Relate Cell Size to Tissue Stiffness

Hypothesis: Bulk tissue stiffness is inversely proportional to cell size.

In *Xenopus laevis* development, the early embryo undergoes rapid cleavages without growth to generate progressively smaller cells. The CSM predicts that as cell size decreases tissue stiffness increases. In this aim, we generate tissues with larger and smaller cells by manipulating cell cycle and test how changes in cell size modulate tissue modulus.

Aim 3: Test contribution of the F-actin cortex on bulk tissue stiffness by modulating F-actin cross-linking

Hypothesis: Increased F-actin cross-linking leads to increased bulk tissue stiffness.

F-actin has been shown to be a major contributor to embryonic tissue stiffness in early stages of development. Organization of F-actin networks is controlled by actin binding proteins, including F-actin cross-linkers. *In vitro* studies have shown a positive correlation between stiffness and actin cross-linking in reconstituted gels (Esue et al. 2009; Wachsstock et al. 1994; Gardel et al. 2004; Luan et al. 2008; Xu et al. 1998) and in cell aggregates (Cunningham et al. 1992). Rheological studies have shown that actin filaments form relatively weak gels at physiological concentrations and thus require auxiliary F-actin binding proteins to cross-link and bundle actin filaments into stiffer arrays (Xu et al. 2000). Here, we test the role of F-actin crosslinking by overexpressing full-length and dominant negative forms of α -actinin-1.

1.4 SIGNIFICANCE

Congenital birth defects are present in 1 in every 130 live births and account for the highest rate of child mortality in the first year of life (Nemer 2008). Defects such as neural tube closure and chronic heart defects carry a tremendous social and financial burden to society. One of the goals of modern developmental biology is to elucidate the genetic causes of these congenital defects to be able to provide tools for early genetic counseling. To aid in finding the causes of these birth defects we must have a better understanding of the mechanisms of development and the role of mechanical feedback in regulating development. We are specifically focused on uncovering the

physical mechanisms that govern embryogenesis and the linkage between genetic information and whole tissue mechanical properties throughout development.

The large-scale tissue movements that construct the early embryo are governed by basic physical principles. Morphogenesis is largely viewed as a dynamic system (Beloussov and Grabovsky 2007) where mechanical and chemical feedback serve to guide cell behaviors, unlike a deterministic system, where genetic factors are the sole regulator of morphogenesis with little input from the cell microenvironment. A cell's microenvironment includes extracellular matrix, homotypic or heterotypic cell contacts, cytokines, micro/nanoscale topography, physical properties of substrate and mechanical forces imposed on the cell (Barthes et al. 2014). These factors can directly affect cell behavior through biophysical or biochemical routes. Thus, it is important to understand which features of embryonic tissues contribute to this feedback and how signals are transmitted across size scales. There has been considerable effort in the past decade to experimentally test how mechanical feedback guides tissue shaping and regulates cell and tissue size through mechanical feedback (Lecuit and Le Goff 2007; Pan et al. 2016). An early model of mechanical feedback during morphogenesis described how stretched cells could propagate a contractile response sufficient to drive folding of embryonic epithelia (Odell et al. 1981). By this model, the initial deformation of cells that triggers contraction is governed by the mechanical properties of the epithelium. More recently, cell growth regulation by mechanical stress has been proposed as a mechanism to ensure structural integrity (Aegerter-Wilmsen et al. 2010; Shraiman 2005), normal growth (Shraiman 2005) and homeostasis (Eisenhoffer et al. 2012) of epithelial tissues

Several structures that provide passive mechanical strength to the developing embryo have been described however the mechanisms to modulate these material properties are not well

understood. Studies have investigated the causes of tissue stiffness changes and its dependence on cytoskeleton proteins through F-actin polymerization (Zhou et al. 2009; Janmey and McCulloch 2007), myosin contractility and microtubule formation (Zhou et al. 2010). Factors such as Rho-GTPase play an important role in the control of cell cytoskeleton to allow motility and force generation (Sit and Manser 2011). These cytoskeletal changes, however may not exclusively explain the drastic stiffness changes observed in a developing embryo. This study investigates how different structural and molecular factors may account for these stiffness changes.

Understanding the factors contributing to tissue mechanics with respect to morphogenesis is critical to future progress in tissue engineering. To smartly design and engineer tissues, a fundamental knowledge of how tissues form and the mechanical properties governing them is imperative. The implications of this work may also apply to other cell and tissue models including mesenchymal stem cells as well as cancer cells in tumors.

2.0 ADHESION MECHANICS IN DEVELOPMENT

An important mechanical feature of any composite tissue is strength and type of adhesion between constituent parts. Multicellular tissues remain intact through cell-cell adhesions and cell-extracellular matrix adhesions. To understand bulk mechanics of the tissue it is important to consider the mechanics of these individual adhesions. It has been long proposed that adhesion strength varies between different adhesion proteins and that cells organize based on these mechanics. The following chapter begins with a review (Shawky and Davidson 2015) on the efforts to quantify adhesion mechanics from the subcellular to tissue level, including a table summarizing advantages and disadvantages of different techniques (Table 1). This chapter does not focus on molecular mechanisms which have been well reviewed (Gumbiner 1996; Takeichi 1988; Ruoslahti and Pierschbacher 1987). In the end of the chapter, I present preliminary data on the role of cadherin on tissue modulus.

2.1 TISSUE MECHANICS AND ADHESION DURING EMBRYO DEVELOPMENT

2.1.1 Introduction

Researchers have long been investigating the physical mechanisms of adhesion in cellular tissues. H.V. Wilson dissociated cells from adult and larval sponges and by combining them he

observed their remarkable ability to regenerate the structure and form of adult sponges (Wilson 1907). Wilson and others observed sorting, protrusive behaviors, tissue self-assembly, and regeneration based on the cell type origin, stage, individual, and species. These observations inspired later workers such as Holtfreter, Steinberg, Trinkaus, and others to consider the role of adhesion and cell motility in driving development and tissue-self assembly. Holtfreter conducted groundbreaking experiments using transplanted tissues to identify that the embryo “organizer” did not function based on its structure, but rather by biochemical means (Holtfreter 1934). He also recombined tissue explants from different germ layers to discover that cells can recognize and distinguish themselves from cells of a different germ layer and have “selective affinity” to one another based on identity (Holtfreter 1939; Townes and Holtfreter 1955). Steinberg proposed the differential adhesion hypothesis (DAH) (Steinberg 1963) to describe the patterns of cell sorting that Holtfreter observed using principles of thermodynamics and adhesion energy. According to the DAH, tissues sort based on tissue surface tension and intercellular adhesion strength (Steinberg 1970). Trinkaus identified cell migration within gastrula stage embryos and tissue explants (Trinkaus 1973).

Ultimately, this work led to the discovery of the molecules regulating cell-cell and cell-substrate adhesion, the founding of the field of cell mechanics, and a resurgent interest in the physical principles of early development, morphogenesis, organogenesis, stem cell biology, regeneration, wound healing, and disease. We focus in this review on recent efforts to understand the physical role of adhesion during development and how molecular mechanisms of adhesion generate biological form. In the following sections, we introduce biophysical methods of investigating cell adhesion and its contribution to the mechanical properties and force production within developing embryos. In addition to biophysical studies on embryos we include studies

with cultured cells and cells isolated from adult tissues to demonstrate how cells coordinate biochemical and mechanical signaling through cell-cell and cell-substrate adhesions.

Adhesion couples cell populations that establish mechanical support in tissues, allowing cells to be “fixed” with varying degrees of freedom to certain structures. For instance, epithelial cells can be constrained by their apical adhesive junctions to a two-dimensional plane, similarly, mesenchymal cells may form a monolayer as they bind a distinctive layer of extracellular matrix. Different cell types and diverse cell substrates can restrict cell movements along interfaces where adhesion receptors or ligands are present or direct the force they generate at these interfaces along specific directions. Context- or stage-dependent changes in adhesion may occur as cells contact new neighbors or as cells change their expression or activity of their adhesions and contacts. As tissues assemble into more complex structures adhesion can serve to couple forces produced by cytoskeletal dynamics in one cell to drive deformation and movement of a field of cells (Kasza and Zallen 2011; Gardel et al. 2010; Parsons et al. 2010).

Adhesion is also thought to contribute to cell sorting during tissue assembly. Sorting refers to the rearrangement of scattered mixtures of two or more cell types into homogeneous clusters. Cell sorting has been observed in aggregates of different cell types (Steinberg 1963), in aggregates of cells expressing different levels of adhesion molecules (Foty and Steinberg 2005), and in aggregates of cells from different germ layers of the early embryo (Townes and Holtfreter 1955). This later observation suggested that cell sorting might contribute to the mechanical processes that drive gastrulation. After germ layer determination in embryos, adhesions alone or adhesion-dependent cell behaviors may drive sorting to specific locations based on the type and density of adhesion proteins (Steinberg and Takeichi 1994). For instance, assembly of extracellular matrix (ECM) at an interface between prospective notochord and paraxial

mesoderm cells could attract other notochord and paraxial cells to each face of the boundary. Mixtures of notochord and paraxial cells might then sort at this boundary and then adopt specific behaviors along the interface, maintaining or strengthening that critical structure. The theories that adhesion alone is capable of driving cell rearrangement and tissue morphogenesis have been contentious (Harris 1976) but have inspired alternative theories in which cell adhesions regulate cell behaviors, or that adhesions might be coordinated with apico-basal or planar polarity cues to create asymmetric patterns of actomyosin contractility.

2.1.2 Structural and mechanical function of adhesions during development.

Adhesion plays a vital role in the establishment of tissue structure by shaping and maintaining the polarity of cell associations with their neighbors and surrounding ECM (Gumbiner 1996). Thus, the biological form of embryos and organs is driven in part by expression patterns and activity of adhesion proteins and the matrix elements they assemble. Molecular-level changes in adhesion regulate cell- and tissue-level processes, both biochemically and mechanically. In its strictest definition, cellular *adhesion* refers to cell-substrate interaction or heterotypic cell-cell interactions, whereas cell *cohesion* refers to homotypic cell-cell interaction. Much attention has been given to the cell- and tissue- scale mechanics of cell cohesion and adhesion in the past two decades in an effort to answer long-standing questions in biology on the mechanism of cell sorting and cancer metastasis. Understanding the mechanics governing cell cohesion and cell adhesion during development and in adult tissues is critical not only to further basic science, but also for the development of cellular therapies and tissue engineering applications.

Tissues are dynamic composite materials and thus have complex material properties. These material properties can be represented by mathematical models adapted from mechanical

engineering. Engineering models of embryonic tissues range from elastic solid-like to viscous liquid-like, depending on the time-scale of measurement. Some of these models have likened tissues to granular powders or colloids. These models are derived from mechanical interactions between smaller structural components and can include cell-cell adhesion forces needed to maintain the integrity of the tissue and cell-ECM adhesion forces to maintain contacts between cells and an external substrate.

2.1.3 Biophysical descriptions of adhesion

The dynamics of adhesions must be considered when considering their mechanical function. Biophysical models of cell adhesion can be based on kinetic, thermodynamic and mechanical descriptions of adhesion (Zhu et al. 2000). Kinetic models describe the rates in which adhesion receptors bind and dissociate and on their differential binding affinities. Thermodynamic models describe the differential chemical potentials of the receptors, ligands and bonds. Mechanical models describe adhesion energy density, γ , defined as the mechanical work required to separate a unit area of the adherent surface. Each of these models can be used to predict experimental properties of adhesions. For instance, mechanical engineers can measure γ using a basic method known as the peel-test which measures adhesiveness of two materials (Kim and Aravas 1988). In this test, the force required to pull two materials apart is measured which is a function of the adhesion energy density. Peel tests have limited utility in measuring the adhesion between two tissues when adhesion strength between the tissues is greater than their cohesion strength. Analogous biophysical techniques have been used to measure cohesion using atomic force microscopy between single cells.

Another important aspect of adhesion which makes it difficult to study is that the cytoskeleton and the adhesive machinery in the cell are not only coupled physically but are also coupled through intracellular signaling pathways. Changes in adhesion can alter the cytoskeleton (Kovacs et al. 2011), which in turn can alter cell mechanics (Zhou et al. 2009). Integrins and cadherins have parallel roles in their respective adhesion complexes and involve several common scaffolding and cytoskeletal proteins such as α -actinin and vinculin and engage similar signaling pathways both independently and through cross-talk (Weber et al. 2011). The overlap between integrin and cadherin function and signaling suggest mechanosensing pathways in the embryo could be activated by cell-matrix adhesion and cytoskeletal tension, e.g. activation of ROCK by RhoA (Bhadriraju et al. 2007). Similar signaling pathways mediate both the formation and maturation of integrin based contacts (Huveneers and Danen 2009) and the accumulation of E-cadherin at cell-cell contacts (Shewan et al. 2005). The direct physical contact between these adhesion systems plays a critical role transmitting force across cells (Maruthamuthu et al. 2010). Intracellular feedback through signaling has been proposed to drive the formation of the notochord-somite boundary during gastrulation in the frog *Xenopus laevis* (Fagotto et al. 2013). This study observed that changes in cadherin clustering at the prospective notochord-somite drives the actomyosin cortex to detach from the plasma membrane. Destabilized actomyosin contractions then drive distinctive cell blebbing which captures and traps cells at the newly formed interface.

2.1.4 Formal definitions of the mechanics of adhesion.

Just as we defined adhesion and cohesion for cells and tissues we can extend their definition to the molecular scale. Adhesion can be defined as the bonding of two distinct entities in a manner that resists their subsequent separation. In the context of cell biology, these entities can be held together through either homotypic or heterotypic protein-protein interactions. Cohesion is the specific adhesion formed via homotypic interactions. To understand the role of adhesion in development we must understand how cell and tissue adhesion resists or enables separation of these adhesions. Both heterotypic and homotypic adhesions resist detachment in the direction normal to the surface, e.g. tension, of the adhesive interface and can resist movement parallel to the surface, e.g. shear. In the case of shear, resistance to movement can be linear or can exhibit complex non-linear responses such as stiction when increasing force causes a tissue to "slip" along a boundary after a critical level of applied force is reached. To understand the biophysical response of cell- and tissue-level adhesion to mechanical loads found in embryos we adopt standard terminology from physics and engineering such as stress. Stress is defined in terms of the force applied over a surface (units of force/area; Newton/meter² or Pascal). Stress that is uniform in all three directions is pressure; a surface is under tension when the forces are applied in a direction that would cause separation and an interface is under compression when forces are applied that would bring the objects on either sides of the interface closer together. Once a force, or load, is applied the tissues can change shape or deform. Since the geometry of interfaces can take many forms, the term strain is a more useful description. Strain describes the amount of deformation per the scale of the object being deformed. The degree of strain a material exhibits when a stress is applied is formally defined as the modulus. A material with a high modulus deforms less under a fixed load compared to a material with a lower modulus. The compressive

modulus describes the degree a material resists compressive loads whereas the shear modulus represents how a material will change shape if a shear stress, e.g. a load applied parallel to a surface, is applied. In the practice of mechanical engineering a material may have different modulus in each of the three cardinal directions and along the six shearing surfaces. Mathematically, the modulus is a 3D tensor. When considering a material that slips at a surface we can define a yield stress which is the stress at which a material slips at the interface; such a material is referred to as a plastic and is permanently deformed once the shear stress is removed. The yield stress can be defined from the stiction force needed to overcome static friction when stationary objects are in contact.

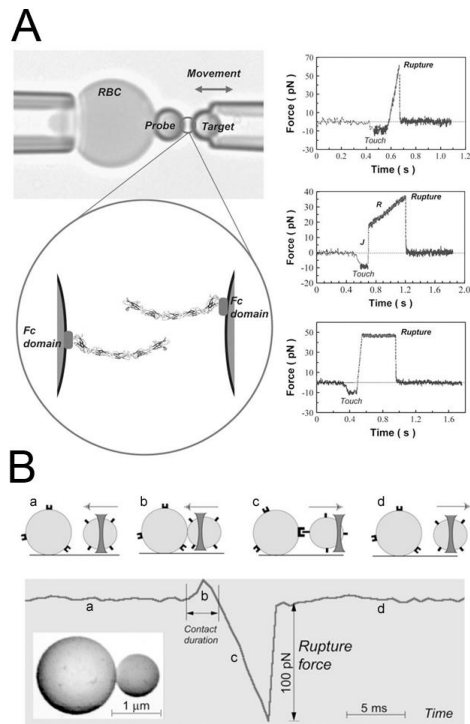


Figure 4. Biophysical analysis of adhesion at the molecular scale.

(A) Biomembrane force probe (BFP) to measure the strengths and lifetimes of homophilic cadherin bonds. Latex beads immobilized with cadherins are brought into contact with one another. After adhesions are established, the forces required to pull the beads apart are measured. The upper panel shows an aspirated RBC with an attached bead

and the probe bead held by the second micropipette. The lower panel is a cartoon of the bound cadherins at the bead-bead junction. On the right, representative force versus time profiles obtained with the steady-ramp (upper), jump/ramp (middle), and constant force (lower) modes of the BFP (Bayas et al., 2006). (B) Laser tweezer system to measure receptor–ligand bond strengths. Integrin molecules are attached to polyacrylamide-coated, spherical silica pedestals and fibrinogen molecules are attached to smaller, laser tweezer controlled, latex beads. The upper panel shows the various steps before and after pedestal-bead contact. The lower panel shows the force profile during the time course of the experiment. Receptor-ligand rupture force is the force required to separate the pedestal and bead after adhesions are made (Litvinov et al., 2002).

Adhesions and biological materials can behave very differently under mechanical loads. A material is elastic if it returns to its original shape after deforming stresses are removed. The degree to which stress produces strain in a material defines the material's elastic modulus. By contrast, a material is viscous if it deforms over time to a new shape that is not restored after stress is removed. The degree to which stress produces a time-dependent strain-rate in a material defines the material's viscosity. In practice, biological materials and adhesive structures fall between the two extremes of elastic and viscous behavior and may simultaneously exhibit both viscous and elastic behavior. These intermediate behaviors can be viscoelastic or viscoplastic. The behavior of these types of materials depend critically on the rate at which a force or stress is applied. A tissue may behave as an elastic material if the force is applied rapidly but may deform more like a liquid if the force is applied over a longer time-scale. Tissues can even exhibit superplasticity - a term borrowed from descriptions of solid crystalline materials (Valiev et al. 1991); superplastic materials can deform well beyond the usual breaking point of an elastic material through rearrangements of grains at specific temperatures or strain rates. Mechanical engineers formulate theory describing such complex material behaviors from the behaviors of submicroscopic components of the materials, however, the elemental components of cells, e.g.

multiple classes of interacting polarized polymers, motors, dynamic cross-linkers and their regulators may exhibit new "physics" (e.g. soft condensed matter physics) that are not well represented by the "orderly" behaviors of simple elastic or viscous materials.

2.1.5 Modulating Adhesions and Mechanics at Different Scales

Adhesion has been studied at many different scales; from single molecule to cellular to whole tissue. Molecular scale experiments isolate adhesion proteins of interest to elucidate the strength of adhesions in an acellular environment, removing variables such as cytoskeletal linkages and intracellular signaling. Adhesion studies at these scales typically use immortalized cell lines or dissociated embryonic primary cells to test adhesion strengths. These experiments cannot reveal the role of tissue mechanical and biochemical cues from neighboring cells that might influence adhesion dynamics *in vivo*. Cell aggregate and cell sheet experiments are more difficult to control during adhesion measurements but attempt to retain some of the native cues cells experience.

Experiments at each scale bring valuable insights but also come with unique caveats. In simple engineered materials, larger scale adhesion can be inferred by the sum of its parts, e.g. the total adhesion strength of a strip of Velcro could be calculated by summing the individual adhesion strength of its constituent 'hooks' and 'loops'. In live cells, it is much more difficult to transition between scales because adhesion systems operate within the dynamic biology of motile cells in tissues. Single molecule experiments are very well controlled but lack the dynamic cellular microenvironment while larger scale aggregate and tissue scale adhesion tests are excellent *in vivo* models of adhesion but retain many uncontrollable variables. Such uncontrollable variables include spatial and temporal information on cell-cell and cell-ECM

adhesion strength within cell sheets during coordinated behaviors. As groups of cells receive and transmit information to and from neighboring cells, changes in adhesion complexes may arise which can either enhance or diminish adhesion and give rise to large-scale morphogenetic movements. Examples of morphogenetic movements that rely on adhesion complex modulation include cadherin contact inhibition at notochord-somite boundaries (Fagotto et al. 2013) and in cell junction remodeling by oscillation and asymmetric polarity of E-cadherin (Levayer and Lecuit 2013). By coordinating experiments across multiple scales, we gain further insight into the mechanics of cellular adhesion.

2.1.5.1 At the single molecule scale

Cohesion and adhesion in animal tissues can be determined by the specificity and general structure of cell surface adhesion proteins (e.g. (Bayas et al. 2006); Figure 4A), and their adhesive strengths (e.g. (Perret et al. 2004)). A range of different experimental approaches have been developed to probe the single molecule level adhesive properties of homophilic cadherin and integrin pairs. Glass beads coated with cell surface receptor proteins such as cadherins and integrins have been used to test interactions when their respective ligands are brought into contact. Using a bio-membrane force probe (BFP), rupture strength between recombinant E-cadherin pairs is tested by loading with precise forces over time from 0.001 to > 1 sec (Perret et al. 2004). The BFP is similar to atomic force microscopy, but the dynamic range of loading and the force sensitivity are greater. There are 3 modes for the BMP; steady-ramp, jump/ramp, and constant force (Figure 4A). Each modality begins by bringing beads into contact with a force of ~10pN and held for 0.1 s. In the steady-ramp mode, beads were separated at a constant loading rate (pN/s) until failure. In the jump/ramp mode, the beads were first pulled apart at a constant loading rate until the force reached a preset value. Surviving bonds were then pulled apart at a

lower rate until failure. Jump/ramp mode was used to distinguish between bound states with different rupture strengths. Finally, in the constant force mode, beads were pulled apart at a constant force until failure. Constant force mode measurements verified the multi-state dynamics of homophilic cadherin adhesion. Using the BFP, the interaction between different recombinant fragments of extracellular fragments were tested along with the contribution of individual fragment domains to adhesion strength. The cadherin extracellular segment is organized in five tandem repeats, numbered from the outermost N-terminal domain (EC1-EC5). These experiments revealed a rupture strength hierarchy for bonds between the full five-domain cadherin fragments, which represented different sub-states of cadherin binding depending on domain engagement (Perret et al. 2004). Similar results were found in studies using recombinant C-cadherin (Bayas et al. 2006; Sivasankar et al. 1999).

Another approach to test single molecule adhesion strength involves laser tweezers. In these experiments, either purified proteins attached to beads or living cells were brought into contact with their ligand and pulled apart. Rupture forces required to separate single ligand-receptor pairs (fibrinogen- α IIb β 3 integrin) exhibited peak yield strengths of 80-100 pN (Litvinov et al. 2002) (Figure 4B). Other studies sought to quantify adhesion by calculating binding probabilities using a dual micropipette system. In this system, live cells with surface-bound receptors and ligands are aspirated into opposite glass micropipettes, and brought into contact for a defined period. In this extension of the classical dual pipette assay, an ultrasensitive red blood cell picoforce transducer is used to detect adhesion strength. CHO cells expressing full length, wild-type C-cadherin were brought into contact with red blood cells modified to bind soluble hexahistidine-tagged C-cadherin ectodomain fragments. Cell pairs were subjected to 50 to 100 contact-retraction cycles which were assigned a 1 or 0 depending on whether adhesion was

observed. Binding probability is the average of all cycles. Cadherin binding curves exhibited a fast, low probability binding state and a second, high probability binding state, which forms more slowly and required the full extracellular segment. In the first two seconds the binding probability rapidly increases to a plateau of 0.2, followed by a two to five second lag phase and transition to a high probability binding state after 20 seconds. Disrupting coordinate binding to a single site drove binding probability curves to adopt a simple monophasic form, as predicted for a single site binding mechanism (Chien et al. 2008). Controlled molecular-scale studies are informative, for instance demonstrating that complex adhesion dynamics can be derived from receptor-scale phenomena, however, single molecule scale experiments cannot capture the role of cell signaling or the role of feedback loops that may occur *in vivo*.

2.1.5.2 Scaling-up: from single-cells to multiple cells and aggregates

Studies of cell aggregates or cohesion between identical cell types highlight the interplay between cell-cell and cell-ECM adhesion and the role of the cytoskeleton on adhesion strength and cortical tension. Cells within embryos are presented with complex mechanical and biochemical cues which may alter their behavior. Just as it is difficult to extrapolate the role of single molecular adhesion to single cells it is further challenging to extrapolate the *in vivo* dynamics of adhesion mechanics in embryos from single cell experiments. To understand adhesion mechanics on this scale requires experiments at the scale of cell sheets and aggregates with physiologically relevant microenvironments. These experiments come with many uncontrollable variables but provide details on the role of adhesion during collective mechanical processes such as tissue spreading and establishment of surface tension.

During development, cell surface adhesion proteins are integrated with the cytoskeleton to hold cells to their environment. Much of the motivation driving these experiments has been

aimed to understand how cells sort from one another during animal development and tissue self-assembly, specifically how germ layers segregate and compartmentalize as development progresses. A leading theory is that cells exhibit differential adhesion for one another and that cells with strongest cohesion end up in the interior and cells with weakest adhesion sort to the exterior (DAH; Differential Adhesion Hypothesis, (Foty and Steinberg 2005)). Recent efforts to test these hypotheses have used atomic force microscopy (Krieg et al. 2008; Puech et al. 2005) (Figure 5A-B) and micropipette aspiration assays (Maitre et al. 2012) (Figure 5C-D). In these approaches, cells from different germ layers are attached to AFM cantilevers or aspirated into micropipettes and brought into contact with another cell or substrate. The force required to break the adhesion from the cell-cell or cell-substrate interaction is a function of contact time and can be measured using either technique. AFM force traces reveal that bonds break sequentially as the micropipettes are pulled apart, suggesting differential bond strength across the adhesion site (Figure 5A-B). In homotypic cell-cell experiments, ectoderm cell pairs exhibited significantly less cohesion compared with mesoderm and endoderm counterparts. Additionally, heterotypic adhesion forces were similar to homotypic ectoderm cohesion.

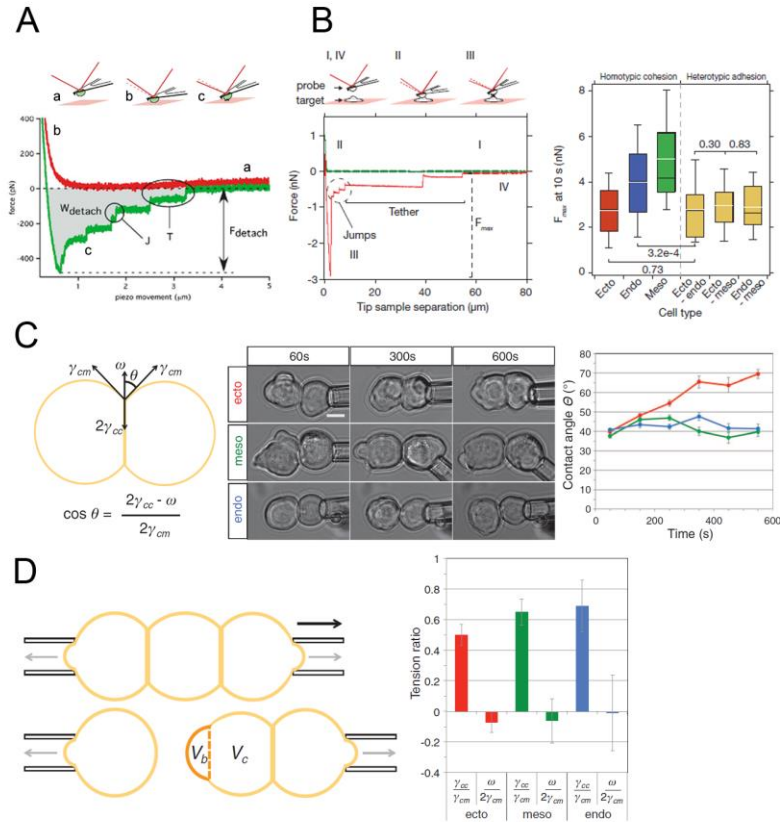


Figure 5. Strategies for measuring adhesion at the cell scale.

(A) Atomic force microscopy (AFM) to measure cell-ECM adhesion forces. Mesendodermal progenitor cells from zebrafish embryos are attached to AFM cantilevers and brought into contact with a fibronectin coated substrate. After adhesions are established, the cantilever/cell is withdrawn from the substrate and the bonds that have been formed sequentially break. The force of detachment is the force required to pull the cell off the substrate after adhesions are established. Numerous distinct ‘detachment events’ are measured during the time-course of cell retraction (Puech et al. 2005). (B) Atomic force microscopy (AFM) to measure cell-cell adhesion forces. This system is identical to (A) except instead of bring cells into contact with an ECM-coated substrate; cells are brought into contact with other cells. Homotypic cohesion and heterotypic adhesion is measured using endo-, meso- and ectoderm primary zebrafish cells (Krieg et al. 2008). (C) Cell doublet shape analysis to measure cell cortical tension. The left panel illustrates how contact angle, θ results from the balance between adhesion tension, ω and the cortex tensions at the cell medium, γ_{CM} and cell-cell interfaces, γ_{CC} The middle panel shows aspirated homotypic cell doublets during the time course of experimentation. The right panel shows contact angles of cell doublets plotted

over time (Maitre et al. 2012). (D) Cell triplet shape analysis to measure cell cortical tension. The left panel illustrates how cell triplets are manipulated with dual microaspirators. Bulge volume V_b is measured at the former cell-cell contact after separation and normalized to the cell body volume V_c . V_b/V_c is a measure of cortex tension at the cell-cell interface. The right panel shows tension ratios computed from homotypic triplet and doublet shapes for each germ layer (Maitre et al. 2012).

The theory of differential cell contractility (DCC) has also been suggested to account for the mechanics of cell sorting (Harris 1976; Brodland 2002). According to this theory, cells develop different levels of contractility at different locations such as the apical versus the basolateral cortex. Differential contractility of cells within a cohesive tissue may drive sorting independent of differences in adhesion strength. High levels of contraction generated parallel to the surface of the apical cell would appear as a surface tension. Both DAH and DCC have been formally tested with aggregates and single cells isolated from Zebrafish embryos to estimate surface tension. In these studies ectoderm cells had the highest actomyosin-dependent cell-cortex tension followed by mesoderm and then endoderm progenitors (Krieg et al. 2008).

Other approaches have focused on quantifying adhesion by analyzing traction forces between cell pairs. If cells in pairs are considered in mechanical equilibrium, the unbalanced traction force on an ECM substrate reflects the force exerted via cell-cell adhesion (Maruthamuthu et al. 2011). Endogenous cell-cell forces were estimated at approximately 100 nN and interestingly, were independent of cell-cell junction length. In a similar study using microneedles as force sensors rather than traction force gels, VE-cadherin mutants resulted in reduced intercellular forces, while traction forces remained similar (Liu et al. 2010). Additionally, junction size was directly correlated with intercellular force, unlike findings from Maruthamuthu et al. These studies describe a direct relationship between total cellular traction

force and cell-cell force generation which suggests functional cross-talk between cell-ECM adhesion proteins and cell-cell adhesion proteins.

2.1.5.3 Sheets, aggregates, and assembly of large multi-tissue structures

Molecular specificity of adhesion serves to integrate a group of like cells into single mechanical units (e.g. sheets, aggregates, tubes, keels, masses, etc). Such units can then respond to applied forces by distributing strain over the structure and avoid "tears" or "rips". Units can remain together, moving over other tissues through active traction or by passively sliding. Examples of "mechanical units" include epithelial sheets that remain cohesive during epiboly and neurulation. Mesenchymal tissues can also form well defined structures such as the neural keel in teleosts (Papan and Camposortega 1994) or the notochord in vertebrates (Stemple 2005). Mechanically integrated tissues may shear or slide over one another. Such shearing movements could occur when clusters of cells actively migrate along interfaces, for example the movement of streaming neural crest (Loring and Erickson 1987) may be driven passively in response to forces generated elsewhere. Many mesenchymal tissues shear with respect to adjacent layers, such as head mesoderm or mesendoderm tissues move during gastrulation (Winklbauer 1990; Davidson et al. 2002).

Experimental approaches to study tissue cohesiveness on this scale, like efforts to understand single cell adhesion, draw physical analogies to surface tension. Considered as an analog to surface tension between immiscible fluids, adhesion forces are thought to act parallel to the cell membrane and seek to minimize the exposed area of the aggregate (Kalantarian et al. 2009) (Figure 6A). Surface-tension forces driven by differential adhesion can be offset by cortical tension (Manning et al. 2010). Approaches to measure surface tension are similar to those used to estimate elastic and viscoelastic properties and include parallel plate compression

and drop-shape analysis. Parallel plate compression of spheroidal aggregates between two parallel plates requires measurement of the force of compression and the shape of the deformed aggregate. By analogy to simple theoretical models of surface tension between two immiscible fluids, the applied force, and geometry of the deformed aggregate allow calculation of an equivalent surface tension for the multi-cellular aggregate. Compression-, sessile- or drop-shape analysis of the aggregate can provides an estimate of the surface tension within the aggregate after forces have been applied. Using these approaches, the contribution of cadherin levels to surface tension have been estimated. Steinberg and co-workers generated several cell lines expressing varying degrees of various cadherin proteins (Foty and Steinberg 2005) and estimated the surface tension of multi-cellular aggregates using parallel plate compression. Similar experiments have been carried out using cells isolated from different regions of the chick embryo where differences in cohesion parallel the capacity of the tissue to sort out (Foty et al. 1994; Foty et al. 1996) (Figure 6B). Using drop shape analysis, EP/C-cadherin knockdown, by cytoplasmically truncated EP/C-cadherin expression (Kalantarian et al. 2009) and EP/C-cadherin morpholinos (Ninomiya et al. 2012), has been shown to decrease surface tension by at least two fold.

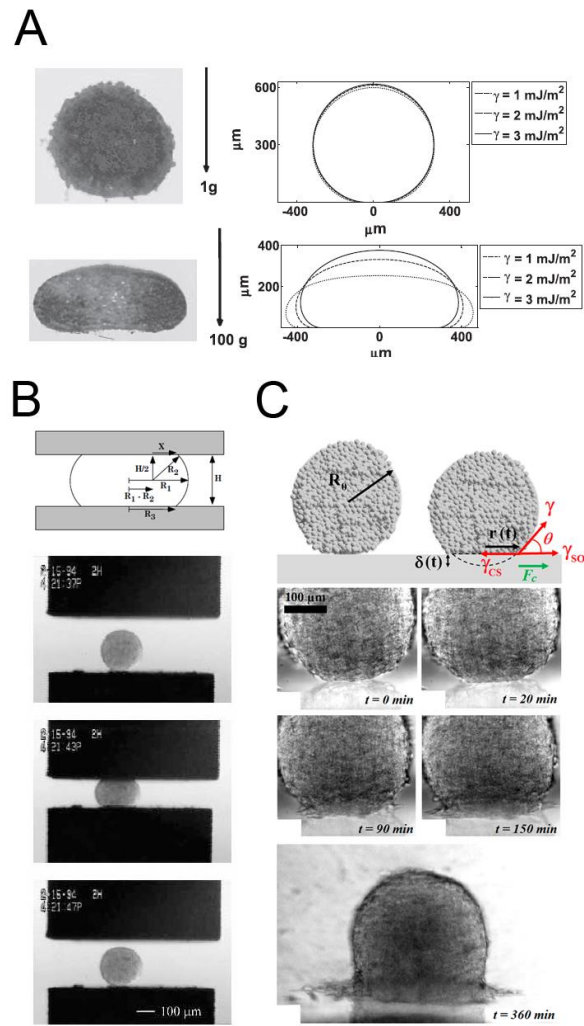


Figure 6. Investigating the biophysics of adhesion at the tissue scale.

(A) Drop shape analysis for estimating surface tension of cell aggregates. Tissue aggregates under variable loading conditions (left) with complementary drop shape analyses and surface tension prediction (right) (Kalantarian et al. 2009). (B) Upper panel is a schematic of a liquid droplet compressed between parallel plates. In brief, radii, degree of compression, and force of compression measurements are combined to calculate surface tension. Bottom panel shows a spherical heart aggregate before, during, and after compression (Foty et al. 1996). (C) Aggregate spreading analysis for characterizing liquid-gas transition behavior. Upper panel is a schematic of an aggregate spreading and parameters used in analyses. All subsequent panels show the progression of aggregate spreading. Spreading dynamics were altered when changing levels of cohesion via cadherins (Douezan et al. 2011).

The process of tissue spreading depends on many of the same adhesion-dependent mechanical processes as sorting and engulfment. Spreading of an aggregate can be used to challenge the forces of cohesion that keep the aggregate together with forces of adhesion which drive spreading onto an ECM substrate. For instance, spheroidal aggregates spreading uniformly on ECM can be modeled by the spreading of liquid on a surface with spreading rates being proportional to cohesiveness of the cell aggregate (Beaune et al. 2014). In highly cohesive aggregates, tissues flow like a liquid, however when cohesiveness is reduced, by perturbing E-cadherin expression, the cells in the tissue act independently. Like molecules in a two dimensional gas, cells detach from the monolayer and move independently (Douezan et al. 2011) (Figure 6C).

Efforts to integrate the physics of tissue adhesion at the single cell scale with the properties of embryonic tissues or aggregates often have multiple plausible explanations and these can be further confounded by complex cell signaling and motility within dense tissues. Cells in tissues are always in contact with neighbors or extracellular substrates which can provide cues for asymmetric contractility, cytoskeletal dynamics, as well as adhesion. For instance, perturbing contacts between cells may alter conventional signaling pathways. However, new biophysical approaches combining fluorescence reporters of molecular strain with systems biology tools such as computational models discussed in the next section can resolve some of these issues.

2.1.6 New efforts to extend mechanics of molecular adhesion to tissue scales: molecular strain and tension sensors.

Combined advances in light microscopy and protein-encoded fluorescent probes have made possible the construction of fluorescent reporters of molecular strain at adhesive junctions (Grashoff et al. 2010; Borghi et al. 2012). Molecular strain sensors, also referred to as intramolecular tension sensors use Förster resonant energy transfer (FRET) to report the magnitude of tension at cell-cell or cell-ECM junctions (Figure 7). These sensors are based on a variety of protein modules that unfold or stretch with increasing force. Strain sensors are constructed with a FRET pair of donor and acceptor fluorescent proteins positioned at either end of the unfolding protein module. Under conditions of low or no tension the donor and acceptor are in close proximity and a virtual photon can be transferred directly from the donor to the acceptor. The missing emission by the donor and extra emission by the acceptor can be observed due to the difference in emission wavelengths of the FRET pair of fluorescent proteins. As force is applied to the adhesion complex, the FRET pair is separated and photon transfer ceases. Early applications of these molecular strain sensors have been promising. One question as these probes are applied is whether the molecular strain reported within the adhesion complex is relevant to the cell and tissue-scale tensions that drive morphogenesis. Another question concerns the dynamic range of these tension sensors, e.g. is the force sensing protein module stiff enough to report intermediate strains? Furthermore, if the protein module is too stiff the fluorescent proteins themselves can be denatured yielding a false indication of reduced FRET (Saeger et al. 2012). One significant limitation of these sensors is that they do not detect the direction of strain only its absolute magnitude. For instance, the reported FRET signal may indicate strain along the apical-basal axis of the cell and not the strain directed within the plane of the epithelium.

However, even with these caveats, these probes are already raising new questions regarding our current views of strain within molecular complexes that mediate adhesion (Conway et al. 2013) and may reveal novel feedback between adhesion and cell signaling pathways.

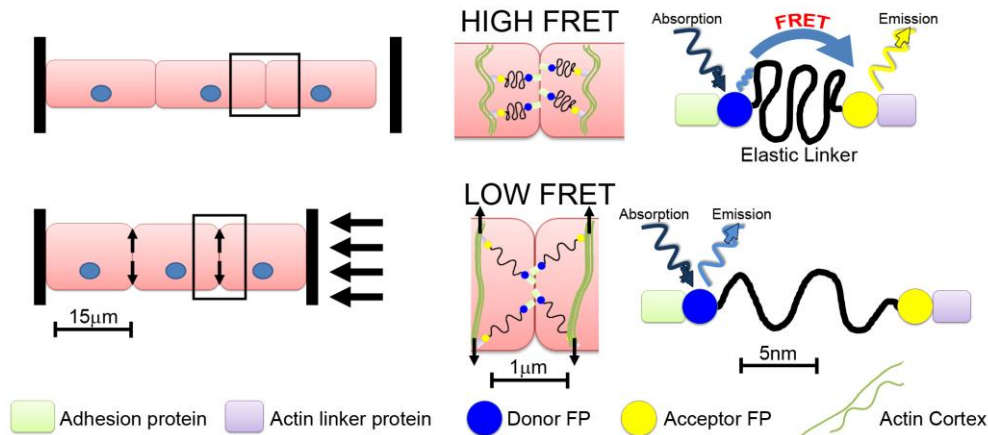


Figure 7. How molecular FRET tension sensors might probe the mechanics of adhesion at cell junctions in tissues under compression.

Several tension sensors have been developed to interrogate the mechanical status of sub-cellular structures. This theoretical example shows such a tension sensor that includes an actin-binding protein on one end and an adhesion protein on the other end. Under no compressive load (top row), cortical tensions will be at a baseline level and therefore the FRET sensor will be in the ‘off’ position, indicating high FRET signal. After compression of the tissue (bottom row) the load will be transferred perpendicular to the applied force to stretch the cell cortices and cortical F-actin networks. As the F-actin networks are stretched, the tension sensor will turn on, causing low FRET signal. In this example, a compressive load at the tissue level is converted to tensile loads at the cell level.

2.1.7 Mechanics and adhesion in the embryo

To better understand the role of adhesion mechanics in the embryo, animal models with controllable adhesion levels have been developed. An elegant study investigating the role of adhesion mechanics *in vivo* focused on patterning within stereotyped cell clusters in the *Drosophila* retina (Hayashi and Carthew 2004). During pattern formation, cell types within the

retina become determined, and adopt identity-specific cell shapes. DN- and DE- cadherins mediate apical adhesion between retina epithelial cells and establish the shape of cone cells. Interestingly, wild type cone cell configurations are nearly identical to soap bubbles confined within similar clusters. In soap bubble clusters these configurations are governed by surface energy minimization. Even mutants, with variable numbers of cone cells, exhibit soap bubble-like configurations (Hilgenfeldt et al. 2008; Kafer et al. 2007) (Figure 8A). With mosaic analysis of adhesion mutant clones, these studies showed that differential DN-cadherin between cone cells and primary pigment cells altered cell shapes into soap bubble idealized configurations. When DN-cadherin is misexpressed in both primary pigment cells and in cone cells, the cone cells did not assume soap bubble, surface area minimized, configurations. While the physical processes control cell shape in the *Drosophila* retina may be more complex than surface-tension mechanics, this study demonstrates the interplay between genetic control of adhesion and physical mechanical processes; regulated levels of cadherin expression adopt shapes analogous to predicted configurations. The success of physical analog models in predicting cell shapes in the retina demonstrates the plausibility of these mechanisms for coordinating local cell shape and geometric order within cell clusters; the question of whether these mechanisms are universal or can produce sufficient stress to shape larger tissues remains unanswered.

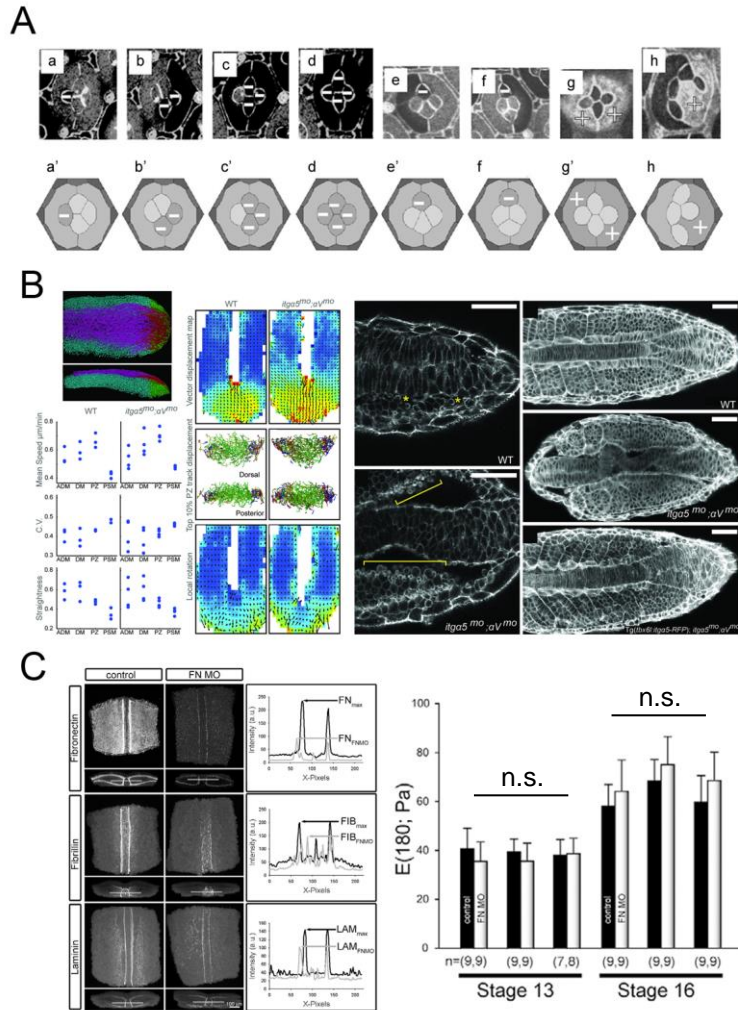


Figure 8. Roles of adhesion at the embryo scale.

(A) *Drosophila* retina ommatidium shapes are governed by cell adhesion and cortex contractility. This panel illustrates various N-cadherin mutants resulting in abnormal cell shapes. Using computer simulations and knock down experiments, Kafer et al. show that a simple surface minimization model is insufficient to model the experimentally observed shapes and packing patterns of ommatidium. The authors develop a model in which adhesion leads to surface increase, balanced by cell contraction, which successfully predicts experimental observations (Kafer et al. 2007). (B) Cell-fibronectin interactions determine tissue fluidity in zebrafish tail bud. Left panel shows the quantitative analysis of cell motion in wildtype and integrin mutant embryos. Right panel is a series of confocal images of phalloidin stained wildtype, integrin mutant, and rescued embryos showing shortened body elongation and increased blebbing (yellow brackets) in integrin mutants (Dray et al. 2013). (C) Fibrillar fibronectin does not contribute to dorsal tissue stiffness in *Xenopus laevis* embryos. The left panel shows representative

confocal images of dorsal tissues stained for fibronectin, fibrillin, and laminin in control and ECM knock-down explants. The right panel shows that the stiffness of explants injected with fibronectin morpholinos (FNMO) does not differ from uninjected explants at either stage 13 or at stage 16 (Zhou et al. 2009).

Another whole embryo model focused on the role of ECM adhesion mechanics during zebrafish tailbud trunk elongation. Paraxial cell movements in these stages appear fluid-like and suggest that cells reduce their elastic coupling. Tissue fluidity during trunk elongation is estimated non-invasively by combining whole embryo imaging and cell tracking analysis. The discovery of highly ordered collective migration and its dependence on cell-substrate interactions (Lawton et al. 2013) has been interpreted to support the role of ECM in maintaining tissue fluidity in the tailbud. To test the role of cell-fibronectin (FN) interactions in vertebrate body elongation, embryos whose integrin receptors for ECM have been reduced generate a body truncation (Dray et al. 2013) (Figure 8B). Surprisingly, characteristic features of migrating cells were unaltered after abrogation of cell-FN interactions. Knock-down embryos exhibited abnormally anisotropic FN along the mesoderm-notochord boundary with high rates of cell blebbing and detachment from the notochord in paraxial mesoderm surface cells. The low rates of blebbing in WT cells suggested that FN matrix constrains blebbing and accompanying changes in cytosolic pressure. Expression of integrin $\alpha 5$ specifically expressed in the paraxial mesoderm rescued paraxial mesoderm FN assembly, paraxial mesoderm-notochord adhesion, and normal blebbing. This study revealed that FN is not only a substrate for cell migration but is also integrated mechanically with cells during tissue morphogenesis.

Cell-cell and cell-matrix adhesions may play direct roles in establishing tissue stiffness during morphogenesis. Dorsal tissues within *Xenopus laevis* embryos increase in stiffness six-fold as from gastrula through neurula stages (Zhou et al. 2009). Over these same stages the

embryo assembles a complex fibrillar ECM at all major tissue interfaces (Davidson et al. 2008). Such a correlation between histology and physical mechanics suggested that ECM could be a major contributor to increasing levels of stiffness. Testing the hypothesis that FN matrix mediated the observed increase in tissue stiffness measurements were collected from embryos injected with FN morpholinos. Interestingly, even though FN, laminin, and fibrillin fibrils were reduced in FN-knockdown embryos, dorsal tissues showed no difference in stiffness from controls (Zhou et al. 2009) (Figure 8C). FN does not contribute to bulk tissue stiffness, however, FN and other matrix components may still contribute to other mechanical aspects of tissue development, for instance, serving as a lubricant for shear at tissue interfaces, as a medium for force transmission through tissue types, or as a permissive signal for cell motility (Rozario et al. 2009).

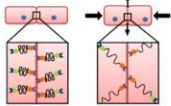
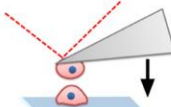
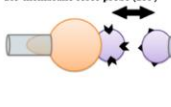
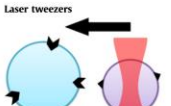
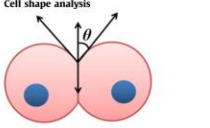
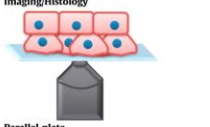
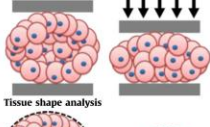
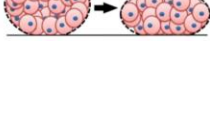
2.1.8 Review Summary

Throughout this review we have described biophysical approaches to measuring adhesion and mechanical properties of embryonic tissues. The fundamental role of adhesion is to connect cells to their microenvironment allowing force-transmission across a tissue. While this is a mechanical process, the forces and stresses originate from the cytoskeleton of individual cells pulling on neighboring cells and matrix. Thus, when considering potential cases of mechanical feedback, it is critical to distinguish between the force-transmission and mechano-transduction roles of these multifunctional systems. Biomechanical tests using controlled strains and strain-rates within physiological levels are critical to distinguishing the mechanical roles played by adhesion. Mechano-transduction occurs when a cell converts a mechanical stimulus into a chemical cue that can be relayed across the cell or to other cells via more conventional biochemical signaling

pathways. To understand the mechanochemical circuits that use adhesion to drive and control development we will need to consider how adhesion operates at the molecular level and how forces and signals are transmitted throughout the tissue. New molecular strain sensors will be powerful tools to probe how forces are transmitted through space and time and across length scales (Figure 7). Using these tools, we will need to answer several questions: How does the action at the level of molecular adhesions alter tissues 10,000-fold larger? How are the direction and magnitude of stresses and strains transmitted over the intervening length scales?

Molecular level mechanics and kinetics provide the most fundamental descriptions of adhesion. The work of many molecules on the surface of cells governs the potential mechanical roles of adhesion and cohesion. Cell dynamics and cues from the environment must be integrated with developmental processes that guide cells in their fate and differentiation. How integrin or cadherin activation drives and organizes the cytoskeleton within the embryo and how their expression and activity are regulated spatially and temporally remain open questions.

Table 1. Techniques to measure molecular, cell and tissue level adhesion mechanics.

Technique	Scale	Advantages	Limitations	References
 <p>FRET tension sensor</p>	Molecular	<ul style="list-style-type: none"> Ability to measure forces at molecular level in intact tissues 	<ul style="list-style-type: none"> Difficult validation process. Unable to obtain directional information. Molecular scale may not reflect cell- or tissue-scale tensions. 	<p>Comway et al. (2013) and Saeger et al. (2012)</p>
 <p>AFM</p>	Molecular	<ul style="list-style-type: none"> Ability to tether proteins and cells at nanometer resolution and under physiological conditions. 	<ul style="list-style-type: none"> Receptor-ligand bond strengths may differ from in vivo due to complex biological interactions. Difficult to run experiments at high velocities due to viscous drag from cantilevers. 	<p>Puech et al. (2005)</p>
 <p>Bio-membrane force probe (BFP)</p>	Molecular	<ul style="list-style-type: none"> Detection of bond rupture forces with piconewton sensitivity. Micron sized trapped beads allow for more 	<ul style="list-style-type: none"> Receptor-ligand bond strengths may differ from in vivo due to complex biological interactions. Limited range of detectable forces (large forces yield non-linear force-deformation relationships). 	<p>Perret et al. (2004) and Bayas et al. (2006)</p>
 <p>Laser tweezers</p>	Molecular-cell	<ul style="list-style-type: none"> Isolation of single molecules Precise control of force application. 	<ul style="list-style-type: none"> Receptor-ligand bond strengths may differ from in vivo due to complex biological interactions. Requires optically homogeneous and highly purified samples. Local heating of sample, potentially perturbing mechanics. 	<p>Litvinov et al. (2002)</p>
 <p>Dual micropipette aspiration</p>	Cell	<ul style="list-style-type: none"> Ability to grasp and move cells into contact with other cells or substrate 	<ul style="list-style-type: none"> Requires substantial deformation of cells. Cells removed from native environment. 	<p>Maitre et al. (2012)</p>
 <p>Cell shape analysis</p>	Cell	<ul style="list-style-type: none"> Obtain cell surface tensions 	<ul style="list-style-type: none"> Dependent on contact time between cell pairs. Cells removed from native environment. 	<p>Maitre et al. (2012) and Manning et al. (2010)</p>
 <p>Imaging/Histology</p>	Cell-tissue	<ul style="list-style-type: none"> Can be done in vivo Genotype to phenotype relationship 	<ul style="list-style-type: none"> Not mechanically quantitative. May change cell identity over time course of experiment. 	<p>Kafer et al. (2007) and Dray et al. (2013)</p>
 <p>Parallel plate</p>	Tissue	<ul style="list-style-type: none"> Directly measure tissue relaxation after application of known loads 	<ul style="list-style-type: none"> Requires spherical aggregates. Risk of changing cell identities over time course of experiment. 	<p>Foty et al. (1994)</p>
 <p>Tissue shape analysis</p>	Tissue	<ul style="list-style-type: none"> Simple prep Obtain cell surface tensions 	<ul style="list-style-type: none"> Requires spherical aggregates. Risk of changing cell identities over time course of experiment. 	<p>Kalantarian et al. (2009)</p>

2.2 RESULTS

2.2.1 Cdh3-ΔE expression reduces cortical actin and reduces tissue stiffness

In this preliminary experiment, we sought to test the role of cadherin function on tissue modulus. In *Xenopus*, C-cadherin is expressed in the egg (Choi et al. 1990; Ginsberg et al. 1991), is required for cell adhesion in the blastula (Heasman et al. 1994) and is expressed in dorsal tissues throughout gastrulation and neurulation (Nandadasa et al. 2009). E-cadherin and N-cadherin begin expression at the start of gastrulation and neurulation, respectively (Nandadasa et al. 2009). We chose to diminish C-cadherin since it is ubiquitously expressed.

To inhibit function of C-cadherin, we expressed a dominant negative extracellular domain deleted cadherin construct, Cdh3-ΔE. mRNA encoding Cdh3-ΔE was injected into the

two dorsal blastomeres at the 4-cell stage at levels that permitted gastrulation. Preliminary results show that cells expressing moderate amounts of Cdh3-ΔE in the notochord exhibit reduced F-actin cortex (Figure 9A). The density of cortical actin has been shown to depend on levels of C-cadherin through depletion and overexpression experiments (Tao et al. 2007).

Overexpression of Cdh3-ΔE in dorsal isolates causes reduced stiffness (Figure 9B). However, C-cadherin inhibition also reduces cortical actin. Thus, since tissue modulus is known to depend on F-actin, it is difficult to isolate the specific role of adhesion to mechanical properties.

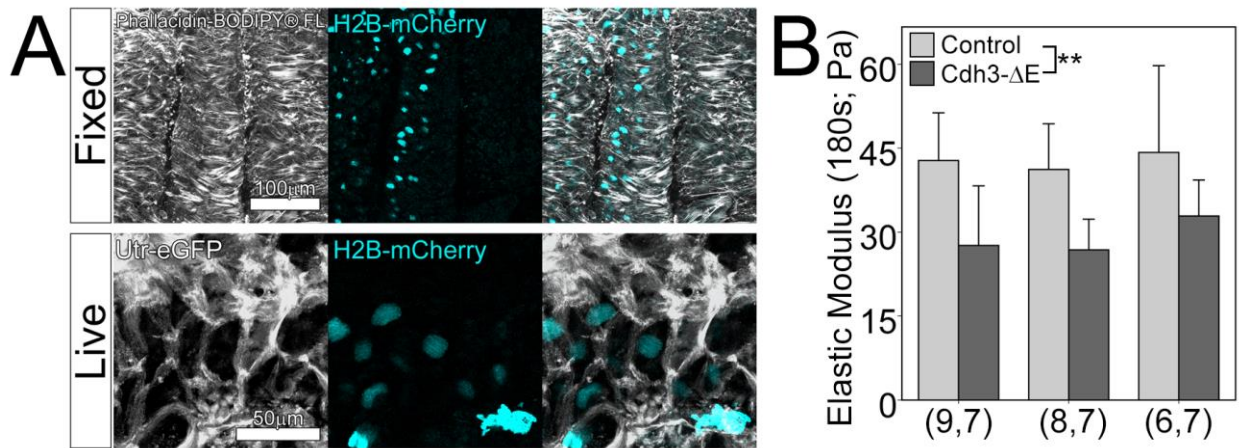


Figure 9. Dominant negative cadherin reduces cortical actin and tissue stiffness.

A) Cdh3-ΔE mRNA was co-injected with H2B-mCherry into the embryo. Embryos were fixed and stained for F-actin (phalloidin) and peeled to visualize the mesoderm-notochord boundary. In live experiments, we also expressed Utrophin-eGFP, isolated dorsal isolates, peeled away endoderm tissue and imaged regions within mesoderm at stage 16. B) Modulus of tissues expression Cdh3-ΔE was reduced by 32% (p-val 0.006; 2-way ANOVA).

3.0 TISSUE ARCHITECTURE & MECHANICAL PROPERTIES

3.1 INTRODUCTION

Tissue movements during gastrulation and neurulation construct specific architectural structures (i.e. segmentation cavities and neural folds) with distinct tissue boundaries through individual and collective cell migration (Aman and Piotrowski 2010), cell shape change (Paluch and Heisenberg 2009), and extracellular matrix deposition. Here, we define architecture as the assembly of tissue shapes and surrounding extracellular matrix that compose the tissue microanatomy. For example, the dorsal axis of a *Xenopus* neurula stage embryo can be viewed as a rectangular prism containing two blocks of presomitic mesoderm on either side of the cylindrical notochord with an overlying block of neural ectoderm and an underlying block of large celled endoderm. Establishment of these structures may facilitate tissue morphogenesis in several ways including creating and guiding morphogen gradients, and constraining specific cell behaviors such as bottle cell contraction or channeling tissue movements such as involution. However, the role of newly formed architectures on bulk tissue modulus has been neglected. To elucidate the source of bulk stiffening in these tissues, it is key to understand how the changing structures within the embryo contribute to bulk mechanical properties.

In this study, we decouple tissue microarchitecture from its material composition by disrupting tissue architecture in embryonic tissues (Figure 10) and measured the mechanical

properties of reaggregated, hereinafter referred to as “scrambled” tissues (scram). We find that, surprisingly, tissue architecture makes little contribution to the bulk mechanical properties but is critical to the continued morphogenesis and continued stiffening of the dorsal axis.

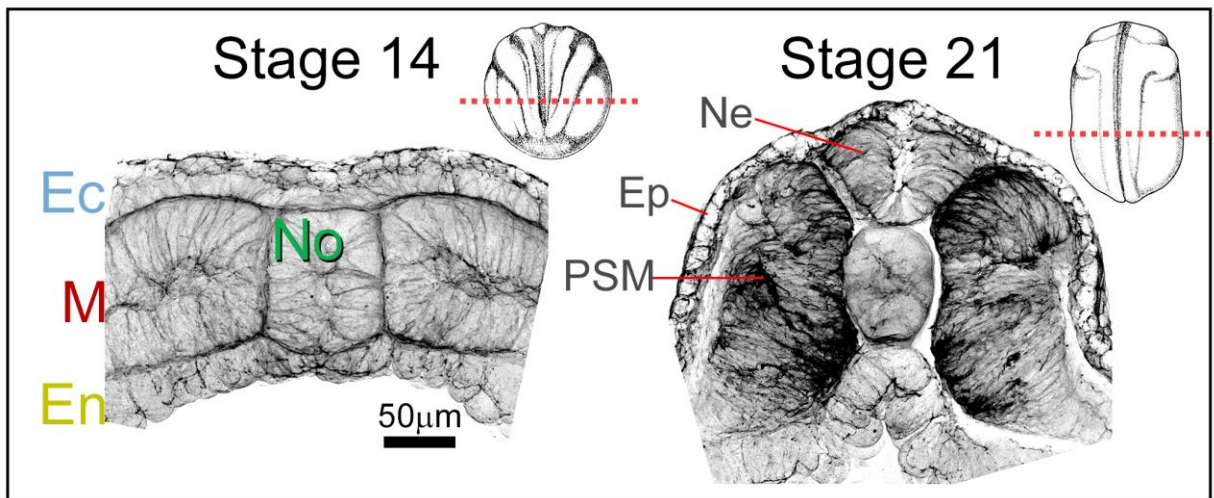


Figure 10. Tissue architecture changes during neurulation.

Transverse sections of Stage 14 and Stage 21 dorsal axial tissues stained for F-actin (phalloidin). Note large scale tissue reshaping in paraxial mesoderm and ectoderm tissues. Ectoderm (Ec); Mesoderm (M); Endoderm (En); Notochord (No); Neural ectoderm (Ne); Prospective epidermis (Ep); Presomitic mesoderm (PSM). The flat Ec tissue at stage 14 bends, folds and internalizes to form the neural tube (Ne).

3.2 RESULTS

3.2.1 Embryonic dorsal tissues stiffen 150% during neurulation

The *Xenopus* dorsal axis is composed of all three germ layers after gastrulation. Tissues from this axis can be microsurgically isolated and cultured for more than 24 hours. This isolated

tissue, known as the dorsal isolate undergoes convergent extension, which is defined by lengthening in the anterior-posterior axis and shortening in the lateral direction. The dorsal isolate retains a consistent cross-sectional composition along its anterior to posterior length. The regular shape and consistent composition of the dorsal isolate allows the use of unconfined compression testing to measure its time-varying mechanical properties. Applying a ~20% strain along the anterior-posterior axis yields a time dependent Young's Modulus from the plateau compressive force, strain during testing, and cross-sectional area (Figure 11A). Dorsal isolates stiffen 150% in 5 hours from Stage 14 to Stage 21 (Figure 11B), confirming with previous measurements (Zhou et al. 2009).

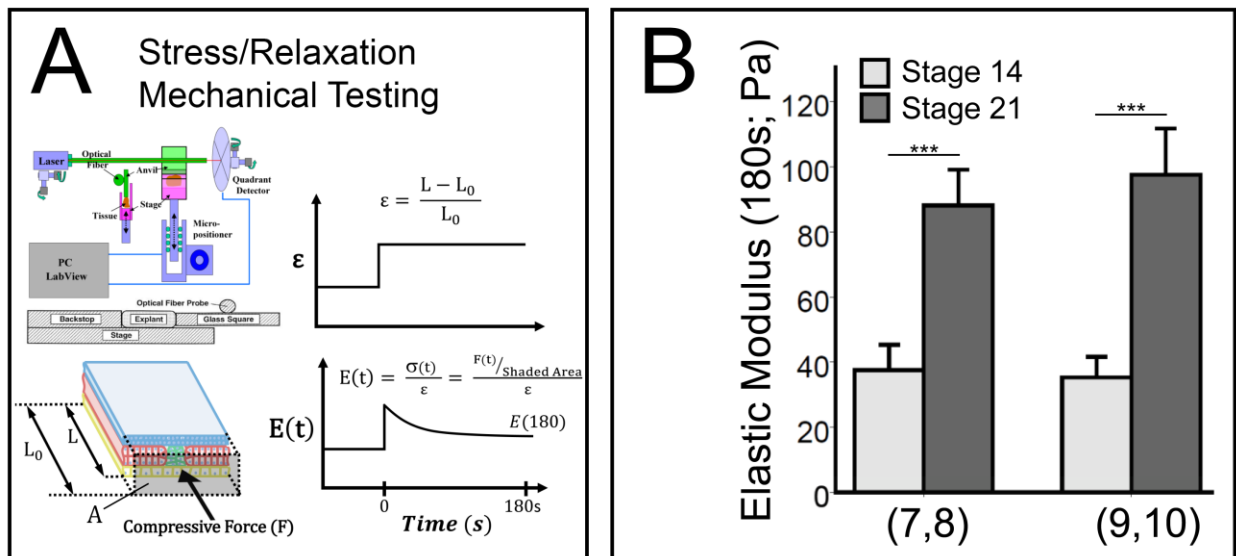


Figure 11. Dorsal tissues stiffen 150% during neurulation.

Dorsal tissues from *Xenopus laevis* embryos are microsurgically isolated and loaded into the A) nanoNewton Force Measurement device (nNFMD) to obtain time-dependent Young's Moduli by uniaxial stress relaxation testing. Tissues are compressed from L to L_0 while the resistive force (F) is measured using a calibrated force transducer and the cross sectional-area (A) is measured after fixation. Schematic of nNFMD reproduced from (Davidson and Keller 2007). B) Tissues stiffen ~150% between stages 14 and 21. Two clutches of embryos were tested with number of explants in each set indicated in parentheses below the plot (***) indicates $p < 0.001$; Mann-Whitney U test).

3.2.2 Architecture changes in dorsal isolate are concurrent with tissue stiffening

Like all vertebrates, the process of neurulation involves both formation of the neural tube and convergence of presomitic mesoderm (Keller 2000; Vijayraghavan and Davidson 2016). These morphological changes involve coordinated large scale movements of laminar cell sheets and results in a thicker (dorso-ventrally), longer (anterio-posteriorly) and narrower (laterally) tissue (Figure 10). At stage 14, the dorsal axis is $128 \pm 13 \mu\text{m}$ in thickness and contains a flat neural plate and brick-shaped presomitic mesoderm. By stage 21, the dorsal axis is $228 \pm 14 \mu\text{m}$ in thickness and has undergone major architectural changes, specifically neural plate folding and mesoderm reshaping to form thicker PSM tissues. The two-cell layered neural plate thickens significantly between stage 14 and 21 from 29 ± 4 to $75 \pm 8 \mu\text{m}$ and forms the neural tube. Cell shapes within the PSM change significantly between stage 14 and stage 21. Transverse aspect ratio of PSM cells increase 2-fold between stages 14 and 21 (p-val<0.001; Mann-Whitney U test; 2.6 ± 0.8 at stage 14, 5.2 ± 1.2 at stage 21; Figure 12). Mosaic labeling also revealed numerous filopodia-like protrusions, often extending more than $10 \mu\text{m}$ between cells of the paraxial mesoderm at stage 14 and 21 (red arrowheads in Figure 12). Thus, we considered whether the stiffening of dorsal tissues reflected the emergence of large coherent structures.

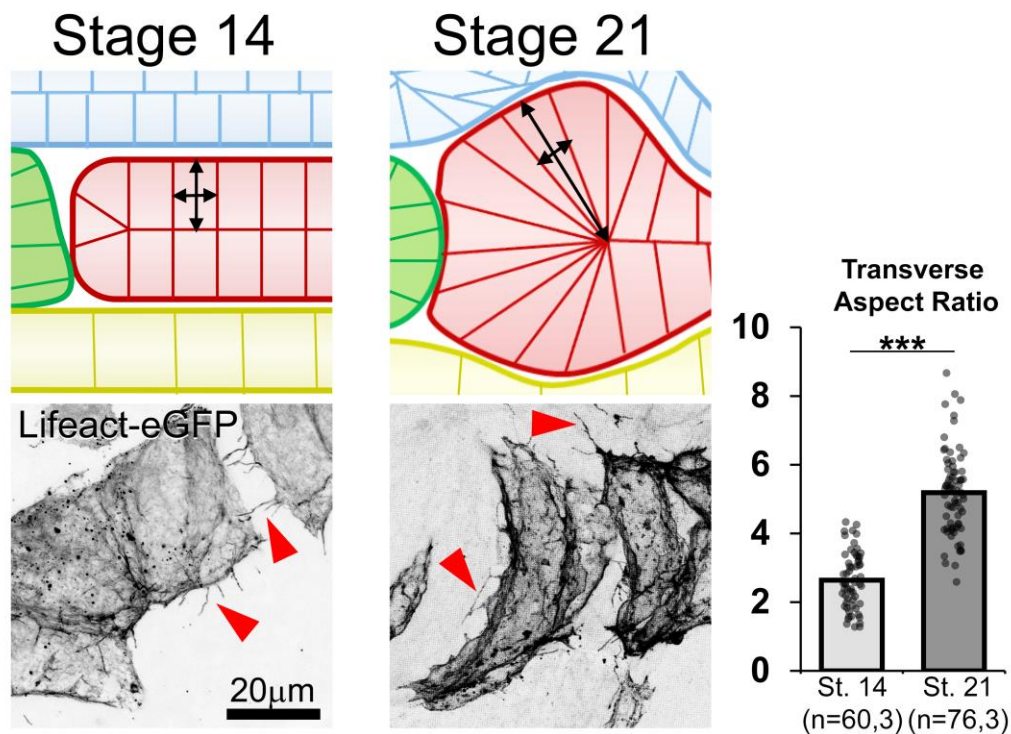


Figure 12. Changes in mesoderm cell shape during neurulation.

Dorsal isolates mosaically injected with F-actin reporter, Lifeact-eGFP reveal cell shapes in presomitic mesoderm tissues (n= cells, explants). By stage 21, mesoderm cells become longer dorso-ventrally, reflecting tissue-level mesoderm thickening (**p-val <0.001; Mann-Whitney U test). Arrowheads reveal filopodia-like protrusions from the lateral surface of the cells.

3.2.3 Architecture of the dorsal isolate is disrupted after 'scrambling.'

To construct a tissue that is devoid of large coherent 3D structures we microsurgically isolated dorsal tissues, scrambled the tissues by gentle cell dissociation, and regenerated dorsal isolate-shaped tissue blocks. Brief incubation in Ca^{++} - Mg^{++} -free media disrupted laminar tissue structure of dorsal isolates (Figure 13A). Dissociated cells were quickly returned to $\text{Ca}^{++}\text{Mg}^{++}$ containing media and reconstituted into large flat elliptical-shaped tissue "cakes" by

centrifugation (8 minutes at 2000g) in a custom flat-bottomed centrifuge tube. Up to 10 dorsal isolates were dissociated and combined to generate ~0.8mm by 1mm elliptical sheets of tissue. Regular dorsal isolate-shaped blocks of scrambled tissues were subsequently dissected from the sheets and cultured for further testing. Scrambled tissues remained viable throughout the centrifugation and reaggregation process.

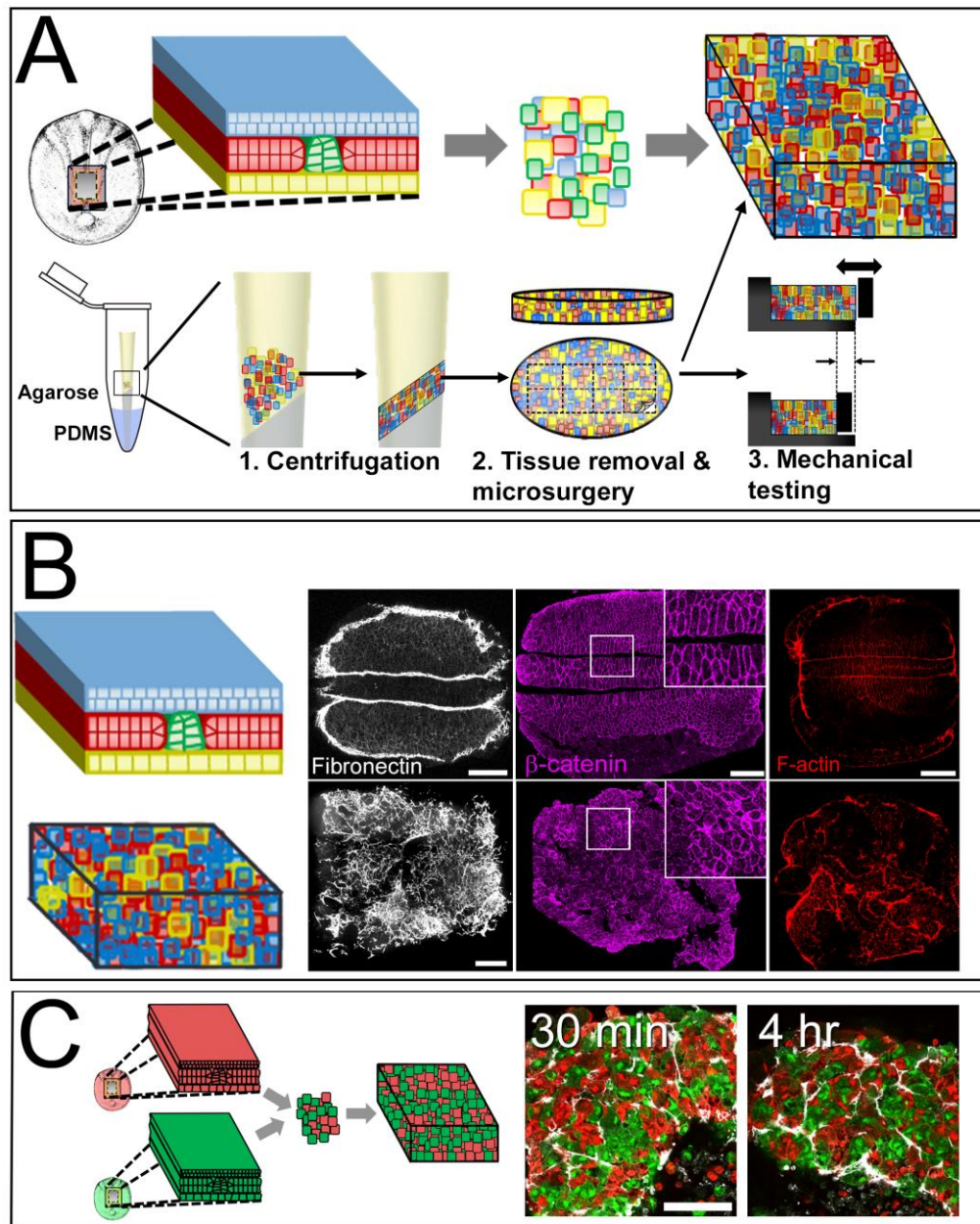


Figure 13. Native architecture is disrupted in “scrambled” tissues.

A) Tissue Architecture disruption schematic. Tissues are isolated at neurula stage, dissociated, and reaggreated into “scrambled” tissues. B) Fibronectin and β -catenin staining reveal loss of bulk architecture, stereotypic fibronectin organization and cell shape in scrambled tissues. C) Cross-explant mixing occurs within ECM encapsulated clusters as seen in scrambled tissues made from half Rhodamine Dextran injected embryos and half FITC Dextran injected embryos. Scale bars 100 μ m.

To assess the degree of bulk tissue architecture disruption after scrambling, we fixed and stained scrambled tissues for fibronectin, the dominant extracellular matrix protein at this stage in development that is found at all germ layer interfaces (Davidson et al. 2004). As suspected fibronectin distribution indicated the loss of bulk structure in scrambled tissues (Figure 13B), however, local tissue microdomains consisting of small clusters of 2 to 20 cells can be found surrounded by fibronectin fibrils. Scrambled tissues retain their shape for at least several hours but do not undergo convergent extension movements or neural fold formation observed in control tissues (Figure 14).

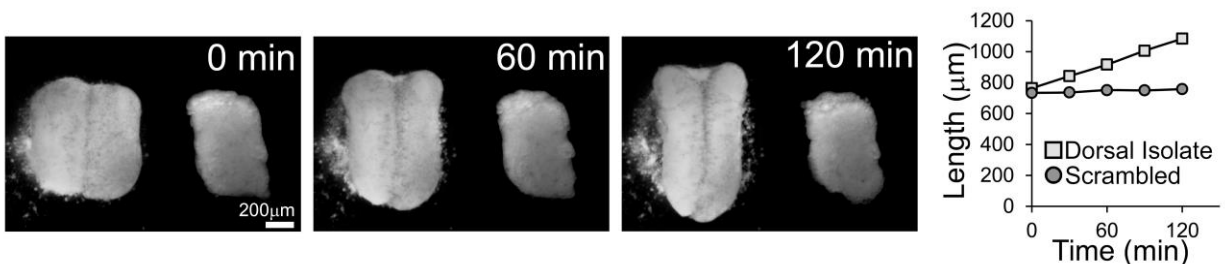


Figure 14. Scrambled tissues do not undergo bulk morphogenetic movements.

Time-lapse sequence of stage 14 dorsal isolate (left) and scrambled tissue (right) cultured in DFA. Dorsal isolate undergoes convergence and extension however scrambled tissue does not undergo macroscopic shape change over two hours. Anterior-posterior length is plotted over time.

To test whether microdomains form from residual connections between cells from a single dorsal isolate or if mixing occurs, we prepared dorsal isolates from embryos injected with lineage tracers FITC-dextran and TRITC-dextran. If cells from single isolates retained their neighbors we would expect only single colors within fibronectin-bounded microdomains. However, dissociated cells from different embryos mixed within microdomains by 30 minutes and persisted at least four hours after aggregation (Figure 13C). Thus, cells from different embryos could join into single microdomains during the aggregation process. Surprisingly, we

did not observe large scale re-establishment of germ layers over four hours. This was surprising since dissociated cells from early amphibian embryos have been shown to sort out by germ layer and reconstruct tissue structures (Townes and Holtfreter 1955). We also note that cell shapes within scrambled tissues are irregular (Figure 13C) compared with stereotypical cell shapes within germ layers in intact dorsal isolates.

3.2.4 Scrambled tissues parallel development of native tissue, differentiating and assembling laminin and fibrillin fibrils

To determine whether scrambled tissues continued to mature at the same rate as intact dorsal tissues we checked whether scrambled tissues expressed stage-appropriate markers. Laminin and fibrillin are two extracellular matrix proteins that appear at low levels during early neurulation (stage 14) and form dense arrays by late neurulation (stage 18) (Fey and Hausen 1990; Skoglund et al. 2006). By the deep neural groove stage fibrillin and laminin are localized around the notochord and at mesoderm-ectoderm and mesoderm-endoderm interfaces proximal to the notochord (Figure 15). Fibrillin is also observed between cells within the notochord (Figure 15, arrowheads). Fibrillin and laminin organization is disrupted in both early neurula and deep groove equivalent-staged scrambled tissues (Figure 15). Just like intact tissues, scrambled tissues aged to late neural groove stages undergo stereotypical assembly of fibrillin and laminin arrays forming fibrillin fibers between notochord cells (Figure 15). Thus, cells within scrambled tissues maintain normal stage-dependent developmental programs of extracellular matrix assembly.

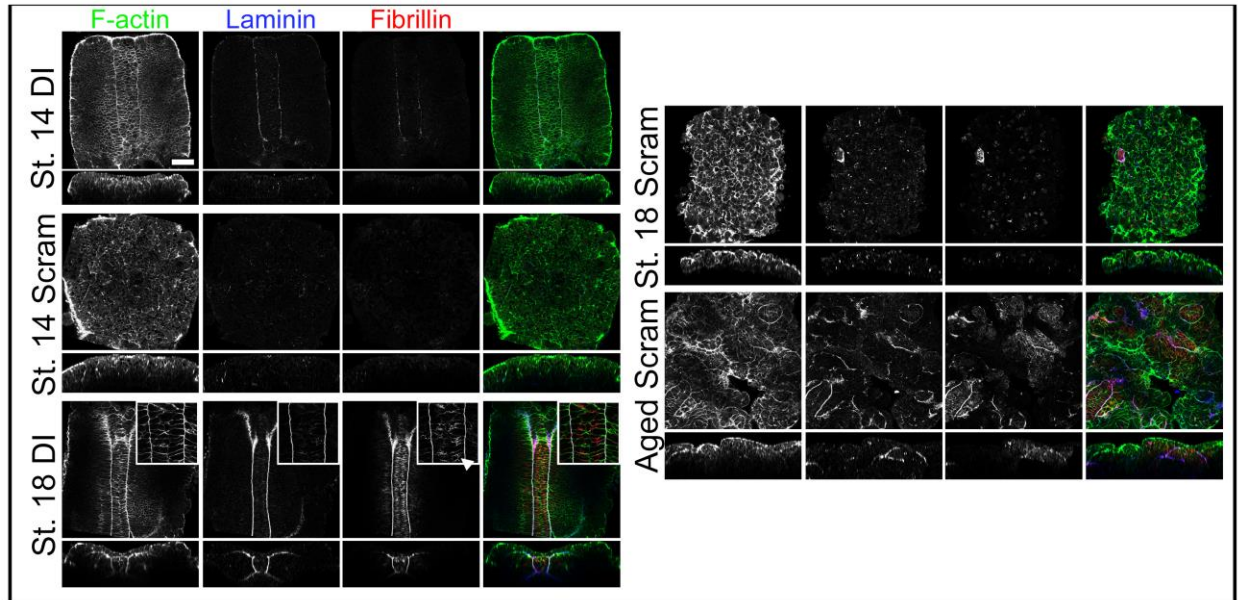


Figure 15. Scrambled tissues synthesize fibrillin and laminin.

En-face z-slices of dorsal isolate and scrambled tissues stained for F-actin, Laminin and Fibrillin. Inset reveals high levels of fibrillin between notochord cells. Aged scrambled tissues (to equivalent stage 18) reveal de novo synthesis of laminin and fibrillin. Scale bars 100 μ m.

To assess maturation of presomitic mesoderm, the tissue previously identified with the highest Young's modulus (Zhou et al. 2009), we tested whether scrambling inhibited somitic cell differentiation. The immunomarker 12/101 stains myofibers (Kintner and Brockes 1984) and appears during neurula stages and appears in scrambled tissues over the same stages (Figure 16). We note that 12/101 in z-projections of confocal stacks appear enhanced compared to dorsal isolates but suspect this apparent enrichment reflects dispersion of 12/101 expressing cells rather than enhanced expression within individual cells (Figure 16, single confocal sections). Thus, mesoderm tissues within scrambled explants maintain the capacity to differentiate into somitic cells.

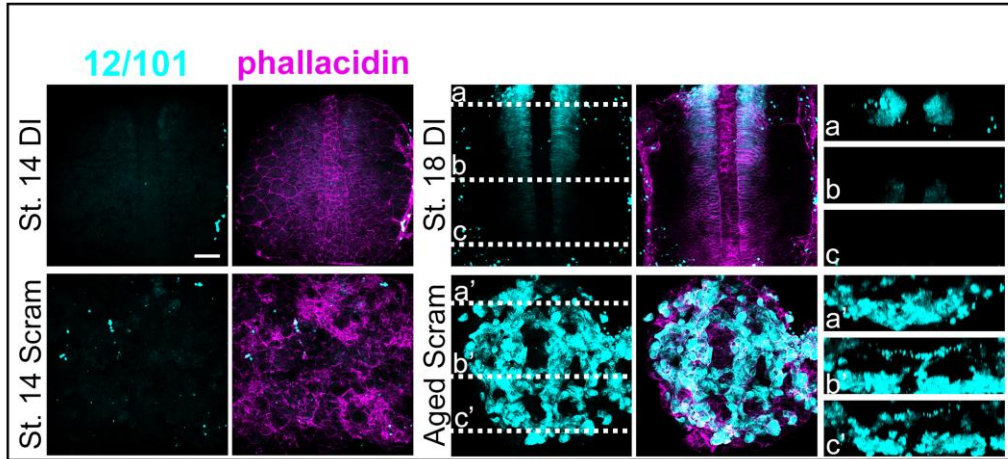


Figure 16. Scrambled tissues differentiate somites.

En face z-slices of dorsal isolate and scrambled tissues stained for somite marker, 12/101 and F-actin (phalloidin). Dashed white lines indicate optical sections at 3 points along the dorsal axis from anterior (a) to posterior (c). Cells within aged scrambled tissues (to equivalent stage 18) express 12/101 indicating differentiation to somitic tissue. Scale bars 100 μm .

To assess F-actin cytoskeletal dynamics in cells within scrambled tissues, we imaged mesoderm cells expressing Lifeact-GFP (Riedl et al. 2008). Mesoderm tissue isolated from Lifeact-GFP expressing stage 14 embryos and unlabeled tissues were mixed as tissues were dissociated and re-aggregated. The resulting scrambled tissues with scattered F-actin labeled mesoderm cells were cultured on a fibronectin coated substrate. During mid gastrulation, when mediolateral cell intercalation begins, mesoderm cells exhibit bipolar protrusive activity oriented orthogonal to the anterior-posterior axis (Shih and Keller 1992b, 1992a). Time-lapse imaging revealed that F-actin protrusive activity was maintained within scrambled tissues compared with dorsal mesoderm within the embryo, indicating that mesodermal protrusive activity persists even after cells have been removed from their native microenvironment (Figure 17), however protrusions were no longer oriented.

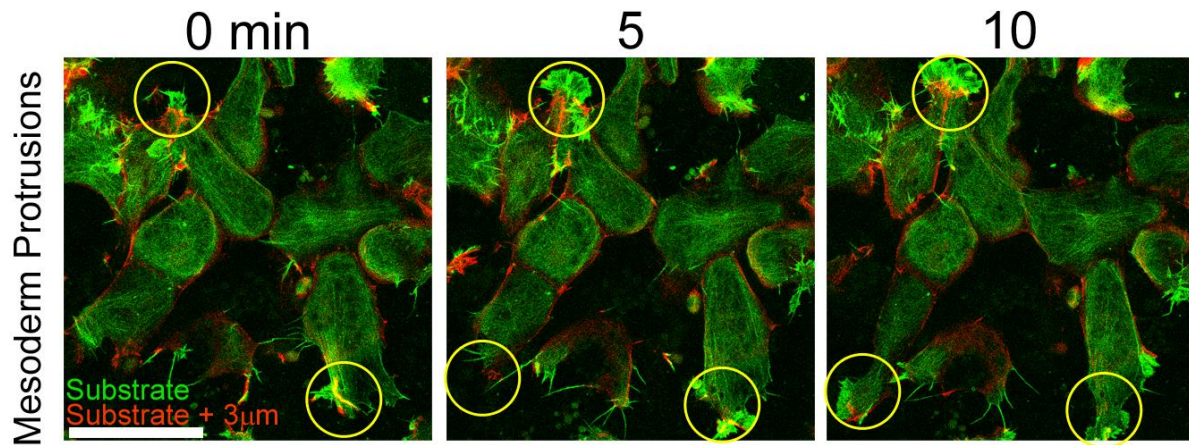


Figure 17. Mesoderm cells in scrambled tissues undergo stereotypic protrusive activity.

Lifeact-GFP expressing mesoderm cells mixed with unlabeled scrambled tissues cultured on fibronectin coated glass substrate. Yellow circles indicate lamellipodial protrusions at the substrate level (green), typical of the converging and extended mesoderm in native dorsal isolates (Shih and Keller 1992b, 1992a). Scale bar 50µm.

3.2.5 Elastic Modulus depends on stage, not architecture

Having confirmed that major structural elements were disrupted and that programs of development continued within scrambled dorsal isolates we compared the mechanical properties of scrambled tissues to intact dorsal isolates. Surprisingly, we found that tissue architecture makes little contribution to bulk mechanical properties. The Young's modulus of early neural plate stage (stage 14) scrambled tissues subjected to an unconfined compression test were not significantly different from stage matched dorsal isolates (Figure 18). Similarly, post-neurulation (stage 21) scrambled tissues showed no difference from stage matched dorsal isolates. Thus, the bulk modulus of scrambled tissues was indistinguishable from those with native architecture.

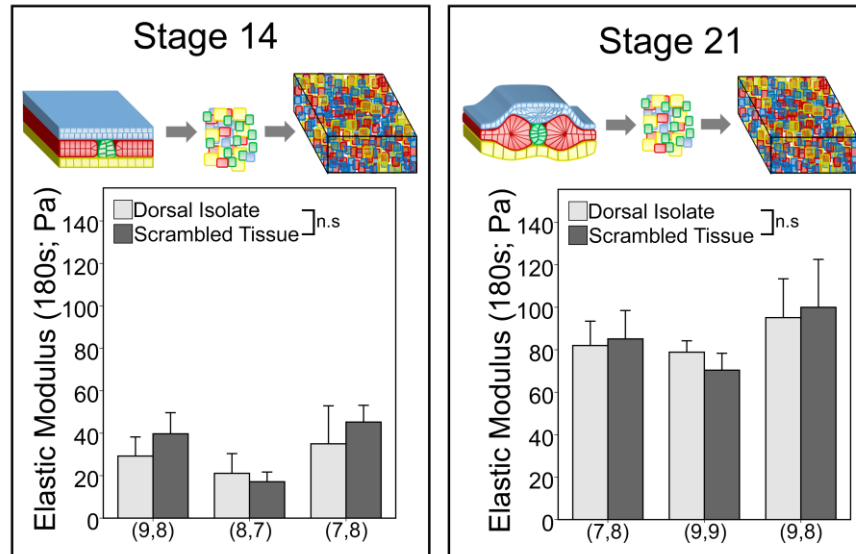


Figure 18. Elastic Modulus of scrambled tissues unchanged from stage-matched dorsal isolates.

Scrambled tissues (dark gray bars) have the same modulus as native control tissues (light gray bars) in early and late neurula tissues (Stage 14: 27.9Pa v. 33.8Pa; two-way ANOVA p-val: 0.371; Stage 21: 85.5Pa v. 85.1Pa; two-way ANOVA p-val: 0.971). Each cluster represents one experiment and n value represents number of explants tested per group. Error bars represent 1 S.D.

3.2.6 Native architecture is required for mechanical maturation

Since native tissues continue to stiffen during neurulation, we then asked whether stage 14 scrambled tissues would mimic native tissue stiffening when cultured to stage 21. We created scrambled tissues at stage 14 and aged them to equivalent stage 14 and stage 21. Aged scrambled tissues stiffened in comparison to early stage scrambled tissues (p-val=0.001; 2-way ANOVA; Figure 19), albeit not to the full stiffness of scrambled tissues created at stage 21. Taken together, these experiments suggested to us that tissue architecture is not important for maintaining tissue modulus in early and late stage dorsal isolate tissues, however scrambling inhibits the tissue's ability to stiffen to native levels.

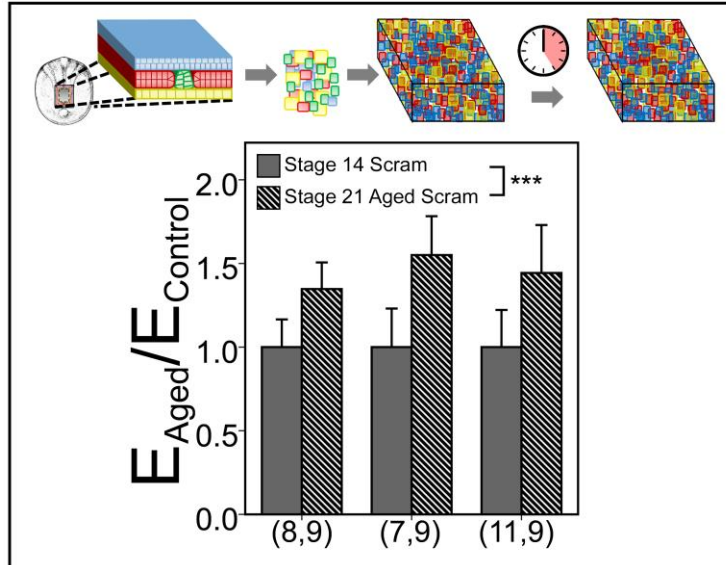


Figure 19. Aged scrambled tissues stiffen, however not to the extent of native tissues.

Aged scrambled tissues stiffened by 45% over 5 hours (p-val=0.001; 2-way ANOVA). Tissues were cultured in DFA and mechanically tested when stage-matched whole embryos reached stage 21. In each experiment, elastic modulus of aged scrambled tissue is normalized to stage 14 scrambled tissue. Each cluster represents one experiment and the value along x-axis for each cluster represents n tissues tested per group.

3.3 DISCUSSION

We investigated the contribution of tissue microarchitecture in embryonic tissues to bulk tissue mechanical properties. A formal test the role of tissue microarchitecture to bulk mechanical properties would require fine-scale control over tissue architecture; however, precisely controlling tissue architecture in the dorsal axis is beyond current tissue engineering technologies. We instead turn to our dissociation protocol to strip tissues of their native architecture. Researchers have long been dissociating and reaggregating cells to investigate how different cell types within tissues sort out from one another to eventually place specific cells in

their correct location. We find that scrambling tissues into random architectures does not alter the bulk mechanical properties of these tissues. This suggests that the source of stiffness in these embryonic tissues resides within the intrinsic stiffness of individual cells rather than the architecture in which the cells are arranged.

We also considered de-differentiation of cells in aged scrambled tissue since cells within scrams could be exposed to different biochemical or biophysical inducible cues in their new microenvironment. During gastrulation, the embryo is patterned by complex signaling pathways which determine germ layer identity and establish the notochord. It has been suggested that cells in the early embryo change competence in a background of persistent inducing signals which make cells less able to differentiate even though inducing signals are present. The process of decreased competence is unclear. Stage 13 presomitic mesoderm has been shown to autonomously differentiate into somite tissue when dissociated in Ca^{2+} - and Mg^{2+} - free media and transplanted into the blastocoel of gastrula stage embryos (Kato and Gurdon 1993). This gave us confidence that mesoderm cells were not changing fate within scrambled tissues. It is possible that cells were induced to mesoderm since mesoderm induction factors remain through stage 23 and have been shown to instruct grafted neural ectoderm cells to dedifferentiate into mesoderm (Dali et al. 2002). The impact of fate change on mechanical properties is unclear however there is a known difference in modulus between germ layers in the frog dorsal axis (Zhou et al. 2009) and differences in surface tension between induced germ cells in zebrafish (Schotz et al. 2008; Maitre et al. 2012; Krieg et al. 2008).

Our results in *X. laevis* suggest that the mechanical properties of cellular tissues with relatively low levels of ECM rely on cell level properties. This finding may be extended to other tissues, either in embryos during regeneration, or within 3D organoid models. Even though the

modulus was unchanged in scrambled tissues, these tissues were not able to restore laminar germ layers or drive convergent extension movements. Most notably, scrambled tissues are also unable to match developmental changes in modulus observed in native tissues. Since architecture is not a regulator of embryonic bulk tissue mechanical properties at these stages, we then focused on testing parameters that are independent of architecture and architecture-dependent mechanisms including cell size and F-actin cortex composition. Exposing and ultimately controlling the programs that coordinate embryonic tissue mechanics will guide efforts to control tissue remodeling and mechanobiology for tissue engineering applications.

3.4 EXPERIMENTAL PROCEDURES

3.4.1 Tissue Dissociation and Reaggregation

To generate scrambled tissues, dorsal tissues isolates were dissociated in Ca^{++} and Mg^{++} free DFA for 5 to 7 minutes and superficial epithelium discarded. Dissociated cells were transferred to custom wells. Wells were fabricated using yellow tips embedded in PDMS in 1.5ml Eppendorf tubes. The ends of the yellow tips were cut off according to the diameter desired for creating scrambled tissues. 50 μl agarose was pipetted into each yellow tip well and allowed to harden to enable tissue reaggregation without attachment. Once, the agarose hardened (<1 minute) cells from the dissociated dorsal isolates were pipetted in and centrifuged for 10 minutes at 5,000G to create disc shaped tissues of uniform thickness. Prior to centrifugation, cells were washed with DFA containing normal levels of Ca^{++} and Mg^{++} . Scrambled tissues were cultured in DFA for 30 minutes before microsurgery and cut into regular shapes approximately 200 by

400 by 600 μm for mechanical testing. Scrambled tissues were cultured in DFA for 30-300 minutes depending on the experiment prior to mechanical testing.

3.4.2 Immunohistochemistry

To assess the structure of dorsal isolates and scrambled tissues were fixed with 4% paraformaldehyde for 3 hours at room temperature or overnight or Dent's fixative overnight. Immediately after fixation, explants were bisected and blocked in 10% goat serum prior to antibody staining. Immunofluorescence staining was carried out with primary antibodies JB3 (Fibrillin-2, Developmental Studies Hybridoma Bank), 4H2 (Fibronectin, courtesy of Douglas DeSimone), β -catenin (Sigma Aldrich), 12/101. Appropriate secondary antibodies (Jackson Immuno Research) were then used (1:200) for 3 hours at room temperature or overnight.

3.4.3 Live cell and tissue imaging

To assess F-actin dynamics within mesoderm cells of scrambled tissues, embryos were injected at the 1-cell stage with Lifeact-GFP and cultured to stage 13. Dorsal isolates were micro surgically excised from Lifeact-GFP expressing embryos and incubated in 20 $\mu\text{g}/\text{ul}$ Dispase (Worthington Biochemical Corp) for 10 minutes to allow separation of germ layers. Mesoderm cells were isolated, dissociated and mixed with unlabeled scrambled tissues and cultured on fibronectin coated glass substrate. Scrambled tissues with scattered Lifeact-GFP expressing mesoderm cells were imaged using confocal microscopy. Single sections and time-lapse sequences were collected using a confocal laser scanner (SP5, Leica Microsystems, Inc., Wetzlar, Germany) mounted on inverted compound microscope (DMI6000, Leica Microsystems,

Inc.) using automated acquisition software (LASAF, Leica Microsystems, Inc.). Laser power, scanline frequency, pinhole size, and PMT gains were adjusted to optimize image quality and minimize photo toxicity. Macroscopic tissue movements of scrambled tissues were observed by collecting time-lapse sequences using a CCD camera (Scion Co, Frederick, MD) on a stereoscope microscope (Zeiss Stemi 2000-C).

3.4.4 Mechanical testing of tissue explants

For mechanical measurements, scrambled tissues and dorsal isolates were loaded into the nNFMD device (described in detail in Section 6.2)(Moore et al. 1995). This device allows us to conduct unconfined uniaxial compressive stress-relaxation tests to measure the time-dependent viscoelastic properties of *Xenopus* embryonic tissues. Tissues were kept at 14 degrees C until testing to ensure testing was conducted at similar developmental stage.

4.0 CELL SIZE ON TISSUE MECHANICAL PROPERTIES

4.1 INTRODUCTION

Cell size is a tightly regulated parameter during animal morphogenesis (Lecuit and Le Goff 2007). Since cells in the *Xenopus* embryo undergo many cycles of reductive cleavages during stages of rapid stiffening (Saka and Smith 2001), we sought to understand the contribution of decreasing cell size on the 150% stiffening during neurulation. We first use the Cellular Solids Model (Gibson and Ashby 1988), described in Section 1.2 to predict the role of cell size change on bulk modulus. We then experimentally generate tissues with larger than native cells by inhibiting the cell cycle starting stage 10. We next generate smaller cells by inhibiting a developmentally regulated cell cycle inhibitor to allow an extra round of division within mesoderm tissues.

4.2 RESULTS

4.2.1 Lower cell density reduces the modulus of dorsal isolates.

Since the mesoderm is the stiffest of the germ layers in the developing neurula (Stage 16)(Zhou et al. 2009) we focused on cell size in the mesoderm. To increase cell size we inhibited cell cycle

progression through S-phase with a combination of 20 mM hydroxyurea and 150 μ M aphidicolin (HUA), which have been shown to demonstrate growth arrest in various cell types in the *Xenopus* neurula without obvious toxicity (Harris and Hartenstein 1991). Dorsal structures, such as the neural tube, still develop normally without cell division (Harris and Hartenstein 1991). Cell cycle inhibitors are introduced at the start of gastrulation, when most division is found to occur (Saka and Smith 2001).

By inhibiting reductively cleaving cell division at stage 10, we produced embryos with larger cells by stage 14 (Figure 20A). We confirmed the effect of HUA on cell size by culturing whole embryos in HUA from early gastrula to early neurula and observing both epithelial cell size and nuclear density within presomitic mesoderm (Figure 21). To ensure that HUA did not perturb large scale tissue organization or F-actin cortex, whole embryos treated with HUA were stained for fibronectin and nuclei (Figure 20B-B') or F-actin (Figure 20C-C') revealing qualitatively unchanged tissue and F-actin organization throughout all three germ layers compared with control embryos.

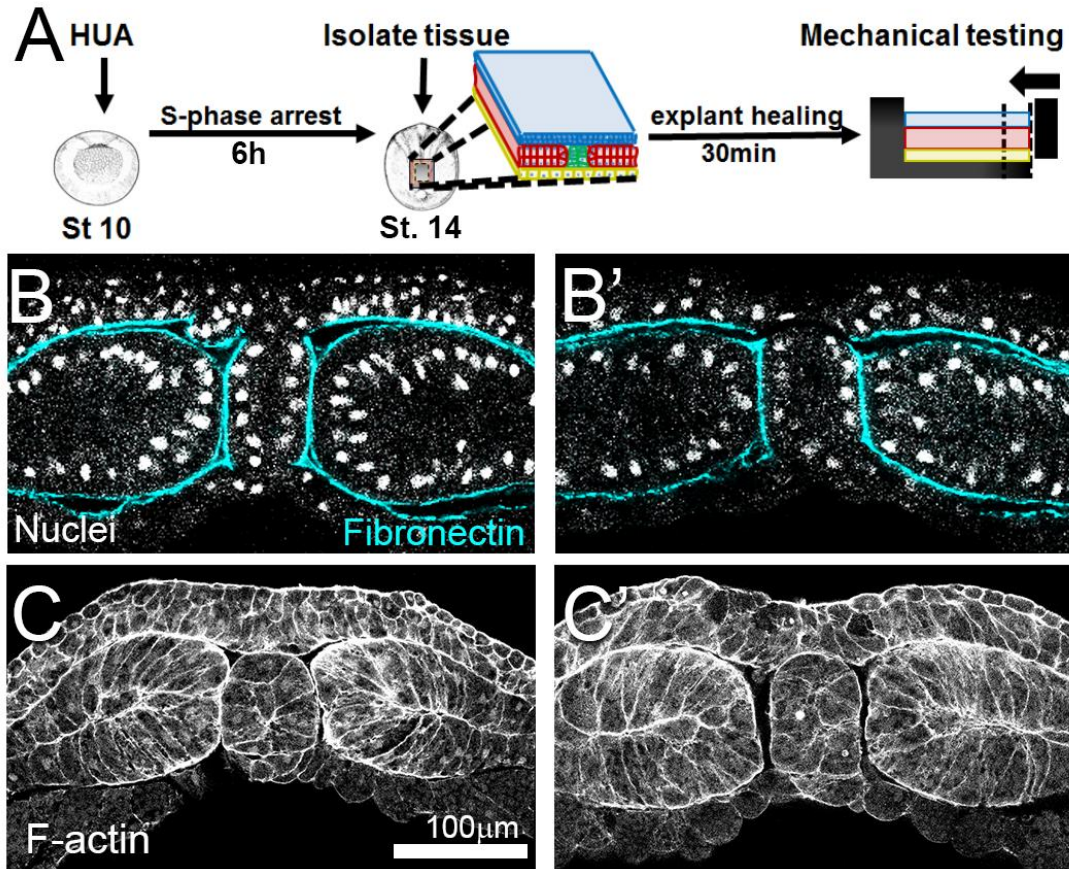


Figure 20. Cell cycle inhibition using HUA doesn't alter bulk architecture or F-actin abundance.

A) To generate large cells in tissue explants, we arrested the cell cycle using a combination of cell cycle inhibitors, hydroxyurea and aphidicolin (HUA). Tissues were microsurgically isolated at stage 14 and mechanically tested. Representative images of control (B,C) and HUA treated (B',C') tissues stained for nuclei (Yo-Pro-1), Fibronectin (4H2) and F-actin (phalloidin).

En face confocal sections of dorsal isolate explants (Figure 21A,A') reveal that HUA resulted in an increase in cell size (not quantified directly from data) and a 34% decrease in nuclear density (Figure 21C). This decrease in nuclear density results in an approximately 52% increase in cell volume calculated by dividing the unit volume from which cells were counted by the number of cells in the volume. Surface epithelial cells also exhibited an increase in apical area (Figure 21C). Cell cycle inhibition with HUA treatment increased cell size by ~ 50% in

embryos at a time point several hours from the initiation of treatment. The CSM predicts a 23% decrease in tissue stiffness for a 50% increase in cell size. We found that tissue explants with larger cells exhibited a 25% decrease in elastic modulus compared with control tissues.

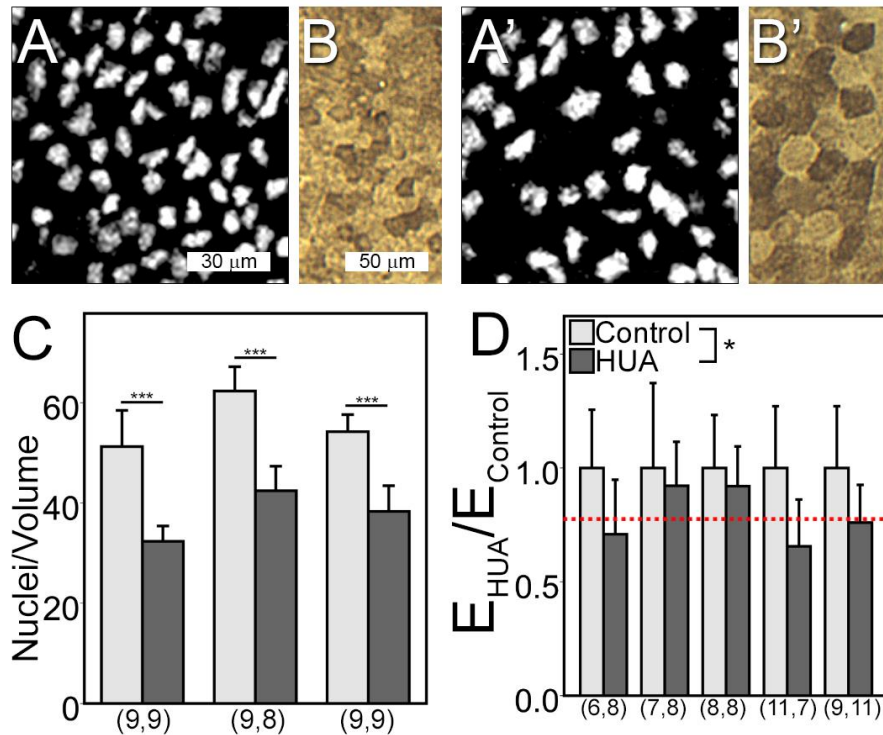


Figure 21. HUA treatment reduces cell density in mesoderm tissues and decreases bulk modulus.

Single z-slices in control (A) and HUA treated (A') mesoderm tissue stained for Yo-Pro-1. Epithelial cells on the ventral surface of the embryo also exhibited an increase in apical area (B,B'). Tissues treated with HUA show reduced nuclei/volume compared with control (***) p=0.01; Mann-Whitney U test; C) and a 25% decrease in modulus (* p-val= 0.04; 2-way ANOVA; D). Each cluster represents one experiment and n value represents number of explants tested per group. Error bars represent 1 S.D. Dashed red line indicates CSM prediction for the decreased density produced by HUA.

4.2.2 Increased cell density increases the modulus of dorsal isolates.

Since the modulus of less cell dense tissues confirms CSM predictions we tested whether the CSM could accurately predict the modulus of denser dorsal isolates. To reduce cell size we inhibited the developmentally regulated cell cycle inhibitor Wee2 (Figure 22A). Wee2 is a tyrosine kinase that prevents cell cycle progression by phosphorylating, thus inhibiting activity of CDK1 and is expressed in the paraxial mesoderm during gastrulation (Leise and Mueller 2002).

Morpholino-mediated depletion of Wee2 increases the mitotic index in paraxial mesoderm tissues (Leise 2004). We confirmed the whole embryo phenotype after injection of 40ng Wee2 morpholino (W2MO) characterized by a reduced somitic ridge during neurulation and a shorter tailbud (Figure 22B). To ensure that Wee2 depletion did not grossly alter the actin cytoskeleton we compared the W2MO injected with the contra-lateral uninjected side and found no difference in F-actin intensity (Figure 22C,D). To test the effects of Wee2 on cell density we coinjected 20 ng W2MO with rhodamine dextran amine (RDA) into one blastomere at the 2-cell stage. By stage 16 we confirmed a 26% increase in cell density in the mesoderm by counting the number of nuclei within 200 μm from the notochord-mesoderm fibronectin interface in transverse sections (Figure 23A,B), which results in a 19% decrease in cell volume, assuming constant tissue volume.

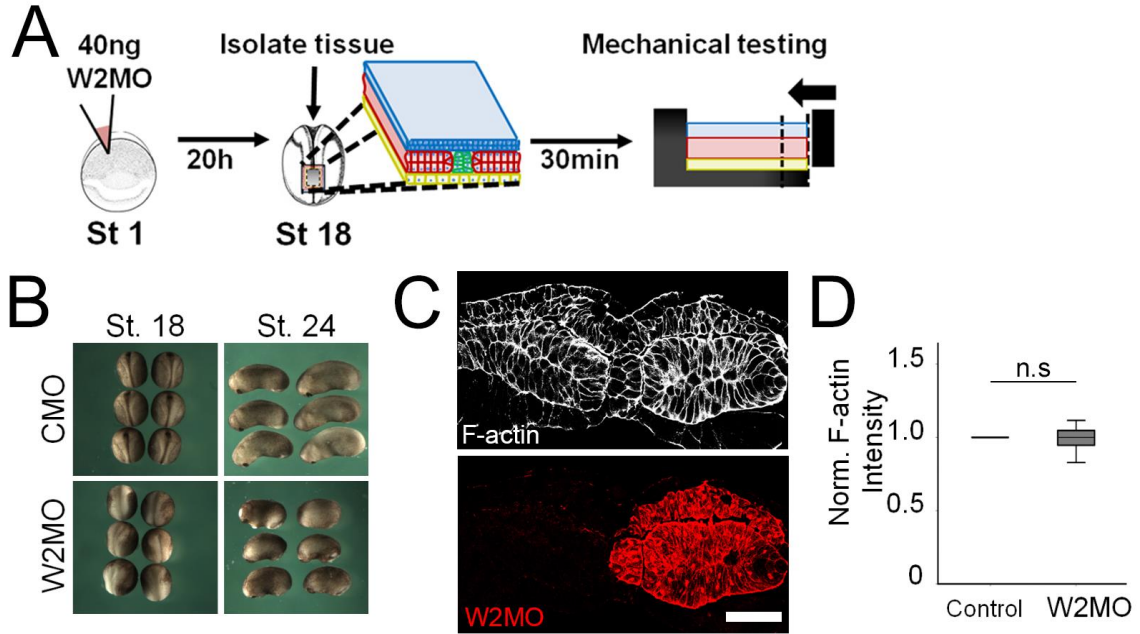


Figure 22. Wee2 depletion doesn't alter F-actin abundance.

A) To generate small cells in tissue explants, we induced a cell division in the presomitic mesoderm by inhibiting a developmentally regulated cell cycle inhibitor, Wee2 using anti-sense morpholino knockdown (W2MO). Tissues were microsurgically isolated at stage 18 and mechanically tested. B) Depletion of Wee2 in whole embryos compared with control morpholino. Note reduced convergence of neural folds at stage 18 and shortened axis at stage 24. C) Transverse sections of stage 18 unilaterally depleted Wee2 (morpholino co-injected with rhodamine dextran amine (RDA)) tissues stained for F-actin (phalloidin). Scale bar 100µm. D) Normalized F-actin unperturbed in Wee2 depleted tissues compared with control.

Having confirmed increased cell density in Wee2 morphant embryos we tested the role of increased cellular density on bulk mechanical properties. We measured the elastic modulus of Wee2 depleted dorsal isolates and compared with control morpholino (CMO) injected dorsal isolates. The CSM predicts a 14% increase in tissue stiffness given a 19% decrease in cell volume. Wee2-MO depleted tissues exhibited a small, yet significant increase in modulus of 12% (Figure 23C).

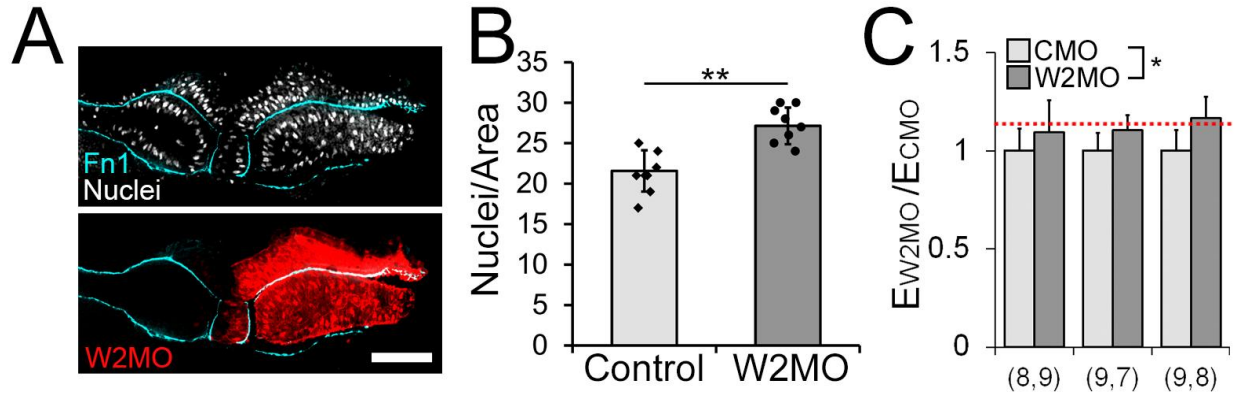


Figure 23. Wee2 depletion increases nuclear density and tissue modulus.

A) Transverse sections of stage 18 unilaterally depleted Wee2 (morpholino co-injected with rhodamine dextran amine (RDA)) tissues stained for nuclei (DAPI) and Fn1. Note increased nuclei within Wee2 depleted tissues. B) Increased nuclear density within Wee2 depleted mesoderm tissue (n=8; ** p<0.002 Student's T-test). C) Tissues depleted of Wee2 show 12% increase in modulus (* p-val= 0.038; 2-way ANOVA). Modulus is normalized to control morpholino (CMO) injected tissues. Dashed red line indicates CSM prediction. Each cluster represents one experiment and n value represents number of explants tested per group. Error bars represent 1 S.D.

4.3 DISCUSSION

In this study, we investigated the role of cell size on bulk mechanical properties of embryonic tissues using the CSM to make predictions. Mechanical testing of dorsal isolates with lower and higher cell density confirm the predictions of the CSM, however, cell density can only account for an approximate 20% increase in modulus from early to late neurulation. Thus, continuing rounds of cell division and increasing cell density are not responsible for the 150% increase in modulus observed over the course of neurulation. It may not be surprising that cell division is not a major contributor to stiffening since axial mesodermal cells, including prospective notochord, stop dividing after dorsal involution, beginning at stage 11 (Saka and Smith 2001). In our

experiments, we targeted cells throughout the entire axis including neural ectoderm and endoderm, however since the mesoderm makes up ~50% of the cross-sectional area of the dorsal isolate, it would require the remaining 50% of tissue to divide many times to achieve 2-3-fold increases in bulk stiffness.

An inherent limitation of our study is that we inhibit cells from entering mitosis. During mitosis, Moesin and Myosin II are activated via Slik and Rho kinase which has been shown to induce cortex stiffening (Kunda et al. 2008). Reducing the number of cells in mitosis could have confounding effects on bulk stiffness. While cell size reduction may not account for tissue stiffening during neurulation, this study gave us confidence that embryonic tissues behave like cellular solids since experimental and theoretical modulus changes after cell size manipulation were in good agreement. In the following chapter, we turned to manipulating the “cell wall,” another important regulator of modulus in foams.

4.4 EXPERIMENTAL PROCEDURES

4.4.1 Cell Cycle Inhibition to Generate Larger Cells

A combination of cycle inhibitors, 20 mM hydroxyurea and 150 μ M aphidicolin (HUA) was used at the start of gastrulation (st.10) and embryos were cultured to stage 14 for mechanical testing. Aphidicolin is an inhibitor of eukaryotic DNA polymerase α and γ , which are responsible for DNA repair and replication. In *Xenopus* egg extracts, Aphidicolin have been shown to inhibit the progressive elongation of nascent DNA strands resulting in cells being stalled in S phase (Marheineke and Hyrien 2001). Hydroxyurea is a blocker of ribonucleoside diphosphate

reductase, an enzyme required for the reductive conversion of ribonucleotides to deoxyribonucleotides. Similarly, treatment with hydroxyurea has been shown to inhibit crucial steps in the synthesis of DNA, thus stalling cells in S phase. Many researchers have used hydroxyurea and aphidicolin in combination (HUA) for a more efficient inhibition of cell cycle. Hydroxyurea has been reported to act fast (1-2 hours) but did not inhibit synthesis completely, while aphidicolin worked slower (4 hours) and inhibited DNA synthesis more completely. (Harris and Hartenstein 1991). All of the drugs used in our cell cycle manipulation experiments are introduced at their respective doses in sealed acrylic chambers mounted on glass. The drugs are reconstituted in media formulated to match the interstitial fluid within the embryo (Danilchik's for Amy; DFA). Cell size (volume) is interpolated based on examination of the nuclear density within a given volume of tissue.

4.4.2 Nuclear density measurements

Since it is difficult to accurately measure cell volumes, we instead looked at nuclear density within a confined volume of tissue and correlated that with cell size. As the nuclear density decreases within a confined volume, cell size is increased. After cell cycle inhibition, tissues were fixed and stained with Yo-Pro-1 and fibronectin (4H2) to visualize nuclei and fibronectin, respectively. Fibronectin staining allowed us to differentiate between the 3 germ layers and consistently isolate the same region in each sample. Nuclear densities were measured by manually counting nuclei within the given volume of mesoderm in each tissue sample. Cell shape was assumed to be cuboidal for simplicity. Cell volume was extrapolated by dividing the volume of mesoderm ROI by the number of nuclei in the ROI.

4.4.3 Microinjection of morpholino

In Wee2 depletion experiments, 20ng Wee2 morpholino (W2MO; Gene Tools, LLC) was injected into 2 dorsal blastomeres (for stiffness testing) or 1 dorsal blastomere (for F-actin and nuclei characterization) at the 4-cell stage (Leise 2004). For microinjection of W2MO, embryos were placed in 1X MBS containing 3% Ficoll (Sigma Aldrich). For contralateral injections, W2MO was coinjected with rhodamine dextran amine (RDA) to identify the injected side. Morpholino injected embryos were cultured to stage 18 and selected based on whole embryo mutant phenotype characterized by a reduced somitic ridge and reduced convergence of dorsal tissues.

4.4.4 Mechanical testing of tissue explants

For mechanical measurements, dorsal isolates treated with HUA or depleted of Wee2 were loaded into the nNFMD device (described in detail in Section 6.2)(Moore et al. 1995). This device allows us to conduct unconfined uniaxial compressive stress-relaxation tests to measure the time-dependent viscoelastic properties of *Xenopus* embryonic tissues. Tissues were kept at 14 degrees C until testing to ensure testing was conducted at similar developmental stage.

5.0 F-ACTIN REGULATION DURING DEVELOPMENT

5.1 INTRODUCTION

An important factor contributing to bulk stiffness in foams includes the thickness and material properties of the "cell-wall" (Gibson and Ashby 1988). In the dorsal isolate, we define "cell wall" as the F-actin cortex directly beneath the cell membrane. Actin is the most abundant intracellular protein within eukaryotic cells and accounts for approximately 1-5% of the mass of non-muscle cells (Gardel et al. 2008). Actin monomers polymerize to form filamentous actin (F-actin) which is an important structural feature that, in combination with molecular motors, enables cells to exert or resist forces. F-actin can be modified by actin binding proteins that inhibit or accelerate polymerization or depolymerization (Lee and Dominguez 2010).

The CSM proposes that "cell walls" are the major load bearing elements within foam. In predicting the role of the cell wall on modulus, CSM includes effects of cell-wall thickness (t), material density (ρ_s) and material modulus (E_s). The distinction between ρ_s and ρ^* , from the description in Section 1.2, is that ρ_s is the density of the solid the foam is made from (i.e. mass of the solid over the volume of the solid) while ρ^* is the density of the cellular material (i.e. mass of the solid over the total volume of the foam) and is equal to 1 minus the porosity. In the CSM, thickness is independent of material properties; however, ρ_s and E_s are coupled. For instance, the modulus of reconstituted F-actin gels depends not only on the concentration of F-actin but also

on filament length, association of F-actin with actin-binding proteins including F-actin motor proteins such as myosin and F-actin crosslinkers such as α -actinin (Xu et al. 1998; Claessens et al. 2006; Grooman et al. 2012). To understand how the physical properties of the actin cortex might regulate bulk physical properties predicted by the CSM we first measure F-actin intensity and cortical thickness between stage 14 and 21. To understand the relationship between ρ_s and E_s we refer to computational models of actomyosin arrays (Kim et al. 2009) (Gong et al. 2013) and experimental studies of reconstituted F-actin gels (Tseng et al. 2002; Gardel et al. 2004; Shin et al. 2004; Wagner et al. 2006) which allow mechanical testing with precise control of F-actin and associated binding protein concentration.

We next perturb the F-actin cortex by enhancing or diminishing crosslinking. Actin filaments can be cross-linked by a variety of different actin crosslinking proteins (Figure 24). Actin crosslinkers modify the connectivity and microarchitecture of F-actin networks into branched networks through ARP 2/3 nucleation (Mullins et al. 1998), or parallel bundles (Bartles 2000) which is important for force transmission through the cell. The size of actin crosslinking protein determines the organization of filaments. For example, short crosslinkers organize filaments into tight parallel bundles while long, flexible cross-linkers allow for orthogonal tethering of filaments and branched networks (Lodish et al. 2000). There has been extensive investigation into how crosslinkers affect the organization and mechanics of F-actin networks *in vitro*. Crosslinkers are dynamic proteins with different affinity to F-actin that allow for temporal control of network mechanics relevant to cell behavior and remodeling. Crosslinker dynamics, particularly dissociation rates, have been shown to regulate mechanical properties of reconstituted actin gels (Xu et al. 1998). Many F-actin cross-linkers are expressed during gastrulation and neurulation in *Xenopus laevis* as revealed by recent deep sequencing data

(Figure 25)(Session et al. 2016). Notably, Fascin-1 (*fscn1*) is expressed at high levels during gastrulation but decreases as neurulation progresses and α -actinin-4.L (*actn4.L*) ramps up expression over 2-fold after gastrulation and persists through neurulation (Figure 25). In this chapter, we chose to investigate the role of α -actinin expression on mechanical properties of the dorsal isolate.

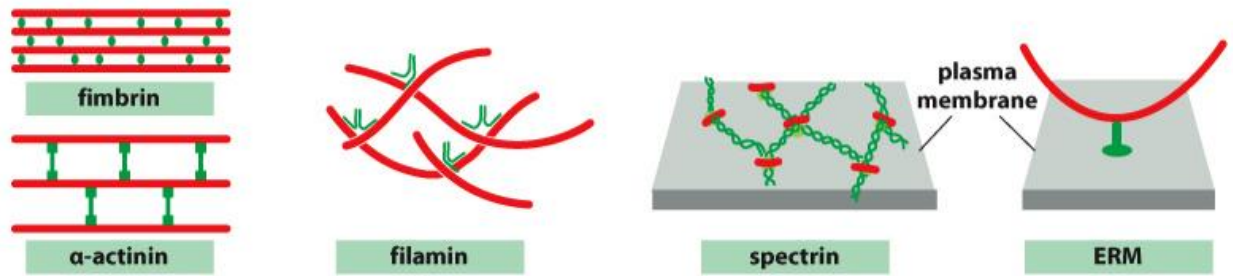


Figure 24. Examples of common F-actin cross-linkers.

F-actin filaments (red) can be organized into different arrays by F-actin crosslinking proteins (green). Fimbrin and α -actinin bundle F-actin into parallel networks, filamin crosslinks F-actin into orthogonal arrays and spectrins and ERM family proteins attach F-actin to transmembrane proteins. Reproduced from (Alberts 2015).

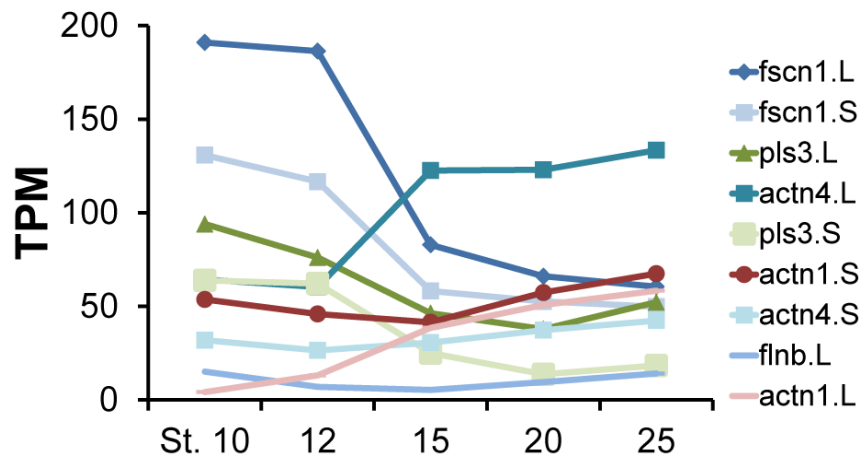


Figure 25. F-actin cross-linkers expressed during gastrulation and neurulation in *X. laevis*.

Deep sequencing data compiled from (Session et al. 2016) revealing temporal pattern of whole embryo expression of abundant F-actin crosslinking proteins in transcripts per million (TPM).

5.2 RESULTS

5.2.1 Endogenous F-actin cortex intensity and stability increase during neurulation

The cell cortex in mesoderm shows both a gross increase in F-actin abundance and stability from early to late neurula stages. Dorsal tissue explants at stage 14 and 21 were fixed in 4% PFA overnight, stained for F-actin (phalloidin), dehydrated and cleared within the same vial. To quantify F-actin intensity, we took two approaches. The first approach was to measure mean intensity within the entire cross sectional area of mesoderm tissue (dashed white ROI in Figure 26A,A') which did not discriminate between F-actin cortex and other pools of F-actin within the cytoplasm. The second approach was to collect high magnification (63X, 3X optical zoom) confocal z-slices and measure intensity across a line profile perpendicular to cortical regions. Max intensity across line scans was compared between stages. Mesoderm F-actin intensity was enhanced 70% according to bulk measurement and 85% in high magnification measurement between stage 14 and stage 21 (Figure 26A-B). Additionally, F-actin networks become polarized and oriented towards the midline by stage 21 (Figure 26E,E').

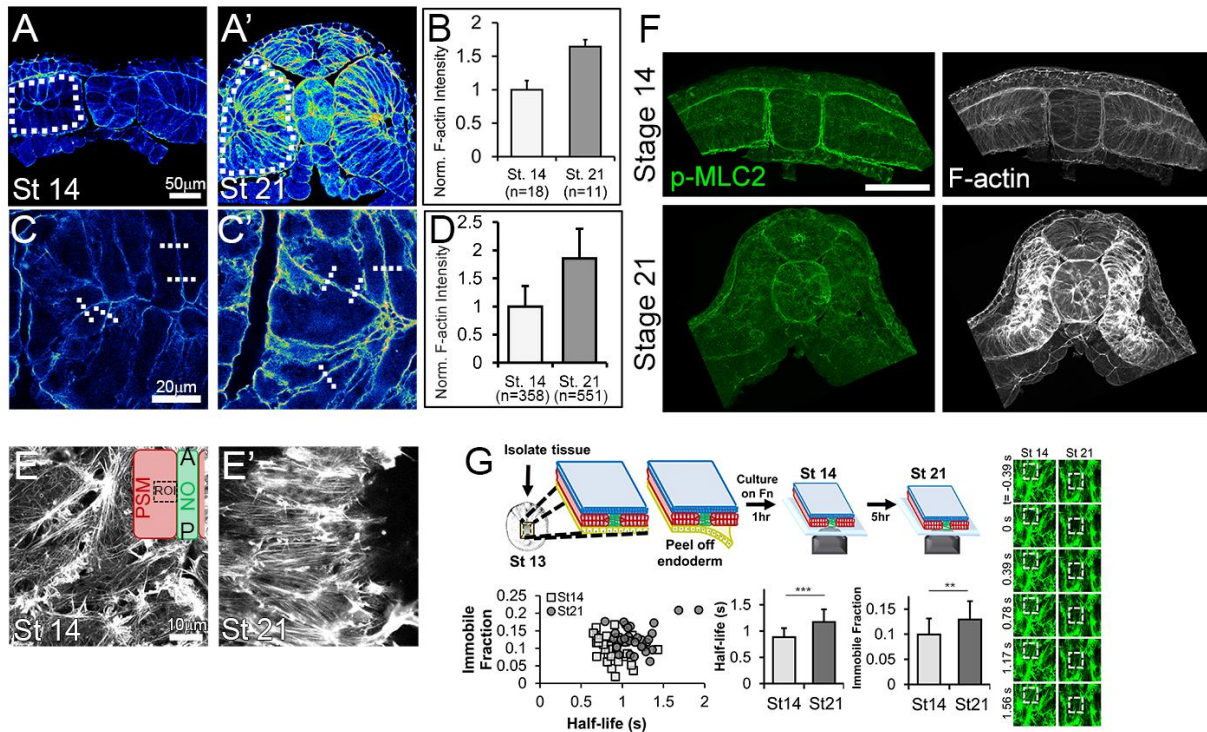


Figure 26. F-actin enhanced and stabilized in mesoderm during neurulation.

Transverse sections of Stage 14 (A,C) and Stage 21 (A',C') dorsal tissues stained for F-actin reveal an increase in mesodermal F-actin abundance. Bulk measurements of mean phalloidin intensity within mesoderm cells (dashed white ROIs) reveals a 70% increase in intensity (A-B'; Mann-Whitney U test p-val p-val <0.01). Phalloidin intensity was also measured by comparing max intensities across lines drawn perpendicular to cortex (dashed white lines), revealing an 85% increase (C-D; Mann-Whitney U test p-val <0.001). High resolution confocal images of the endoderm-side mesodermal F-actin network at Stage 14 (E) and Stage 21 (E') reveal alignment and polarization of F-actin network by Stage 21. F) Transverse sections of stage 14 and 21 dorsal isolates stained for p-MLC2 and F-actin. Scale bar 100 μ m. G) Schematic of F-actin FRAP experiment. Dorsal isolate tissues were isolated from Stage 13 embryos injected with an F-actin live reporter (LifeAct-GFP), endoderm peeled off and cultured on fibronectin to Stage 14. FRAP experiments were done on Stage 14 (n=32 cells) and Stage 21 (n=30 cells) tissues. Representative FRAP experiment showing ~50% bleach at 0s with full recovery by 1.5 s. Stage 21 mesoderm tissues had higher immobile fraction and half-life (** p<0.002, *** p<0.0001; Student's t-test) compared with Stage 14 tissues.

Although F-actin is enriched in mesoderm between stages 14 and 21, no gross increase in myosin activation (p-MLC2) was observed (Figure 22F). Myosin II contractility contributes significantly to modulus in stage 16 explants (Zhou et al. 2009) however, it is unclear what contribution myosin II contractility provides for Stage 21 explants. We treated stage 14 and stage 21 dorsal explants with Rho kinase (ROCK) inhibitor, Y-27632 (50 μ M) for at least one hour. Rock inhibition reduced stiffness by 52% in stage 14 explants (36.3 \pm 6.8 Pa v. 17.6 \pm 7.8 Pa; 2-way ANOVA p-val: 0.017), consistent with stage 16 explants. However, ROCK inhibition reduced stiffness by 39% in stage 21 explants (93.3 \pm 13.4 Pa v. 56.5 \pm 10.3 Pa; 2-way ANOVA p-val: 0.019), indicating that ROCK-mediated myosin contractility contributes less to the modulus at stage 21 compared to stage 14 (Figure 27). To evaluate the stability of mesodermal F-actin we prepared Wilson explants (Wilson and Keller 1991), microsurgically removing the endoderm from dorsal isolates at stage 13, cultured explants to early or late neurula stage and conducted fluorescence recovery after photobleaching experiments (FRAP) to assess F-actin turnover. FRAP analysis of exposed mesoderm revealed F-actin in the cortex is significantly more stable at stage 21 (half-life and immobile fraction, p-val < 0.05; Figure 26G).

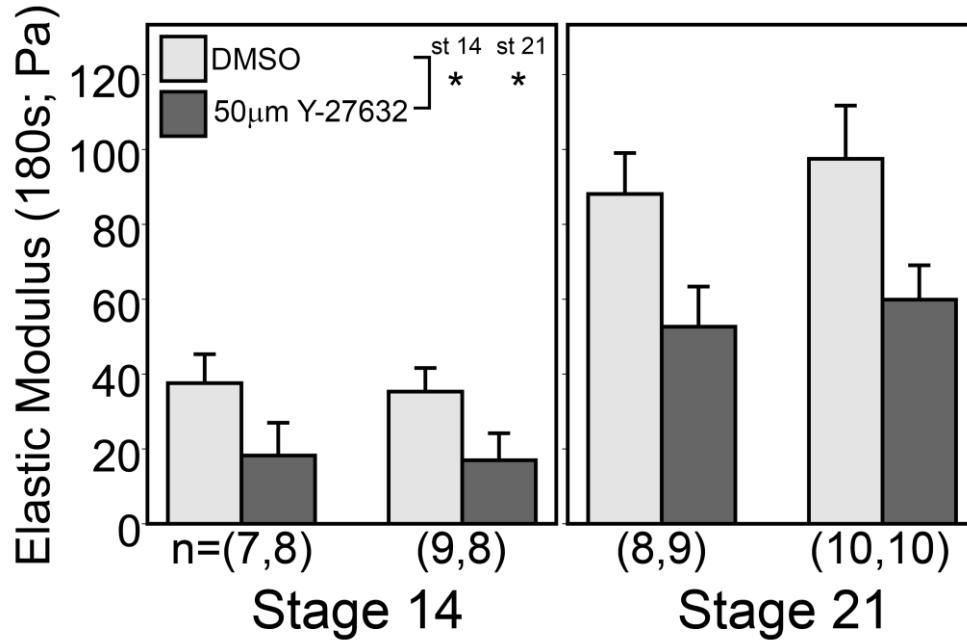


Figure 27. Rock inhibition reduces modulus of stage 14 and 21 dorsal isolates.

Stage 14 and 21 dorsal isolates treated with Y-27632 (50 µM) for at least one hour were tested in the nNFMD and compared with untreated DMSO controls. Y-27632 treatment significantly reduced modulus at stage 14 (* p-val: 0.017; 2-way ANOVA) and stage 21 (* p-val: 0.019; 2-way ANOVA). Each cluster represents one experiment and n value represents number of explants tested per group. Error bars represent 1 S.D.

5.2.2 F-actin Cortex thickness unchanged during neurulation

The enhancement of F-actin cortex intensity can be due to increased cortex thickness, t , and/or cortex density, ρ_s . The CSM predicts that cortex thickness can be a strong contributor to bulk modulus, for instance, to account for the 150% increase in modulus observed during neurulation would require a 79% increase in thickness. To quantify “cell-wall” thickness, we adapted a method used in single cells to measure F-actin cortex thickness (Clark et al. 2013), inspired by single-molecule high resolution colocalization (Thompson et al. 2002). Since F-actin cortex thickness is below the light resolution limit, it is impossible to directly measure via conventional

confocal microscopy. Instead, the position of a diffraction limited point, line or sheet can be determined with nanometer precision using a Gaussian fit around the point spread function (PSF) it produces (Churchman and Spudich 2012), assuming known geometry of the object and a high signal/noise ratio. Thus, using a theoretical description of the cortex geometry, cortex thickness can be calculated, independent of intensity, by relating the distance between the plasma membrane and actin cortex, Δ . The F-actin cortex is assumed to be uniformly dense, decay abruptly at the cytoplasm interface and in direct contact with the negligibly thin plasma membrane. Thus, the distance between the center of the actin cortex and center of the plasma membrane is $1/2$ cortex thickness.

Cortex thickness measurement within a tissue requires isolated cells whose membrane and F-actin cortex and simultaneously labeled. mRNAs encoding actin and membrane reporters are injected into one dorsal blastomere at the 16-cell stage to achieve mosaic scatter throughout the axis (Figure 28). Once fixed, tissues were also labeled with phalloidin, to assess F-actin intensity independent of Lifeact expression levels to compare F-actin intensity and cortex thickness for each line scan. Cortex thickness is calculated using the intensity profile across a junction between a cell expressing fluorescent proteins for both membrane and Lifeact and a non-expressing cell followed by Gaussian fitting around peaks in each channel (Figure 29). Interestingly, we measured no change in F-actin thickness in mesoderm cells between Stage 14 and 21 (Figure 30). We also did not observe a relationship between cortex intensity and thickness. Since cortex thickness was not enhanced, this suggested that observed F-actin enhancement is likely due to increased cortex density.

5.2.2.1 Limitations of Cortex Thickness Measurement

The cortex within cells of the presomitic mesoderm is assumed to be orthogonal to the X-Y axis of imaging. Cell shapes in the mesoderm vary drastically, seen from 3D reconstructed cells at stage 14 or 21 (Figure 12). The degree of cortex curvature in the out-of-plane direction may confound our cortex thickness estimates (Figure 31). To estimate curvature, we can measure the position of the cortex in several z-slices above and below the slice of interest and relate the X-Y offset to the skew of the junction. An angle skew in the X-Z or Y-Z plane would likely result in an underestimation of the distance between cortex and membrane positions, and thus an underestimation in thickness. Additionally, small vesicular structures present during endocytosis or exocytosis may introduce additional variance in our estimates. Another limitation of measuring cortex thickness in mosaically labelled cells is that it is assumed adjacent cells do not receive any injected mRNA. Low levels of Lifeact mRNA in ‘unlabeled’ cells sharing a junction with ‘labeled’ cells can result in a skewing of the relative position of the cortex towards the membrane and again an underestimation of cortex thickness.

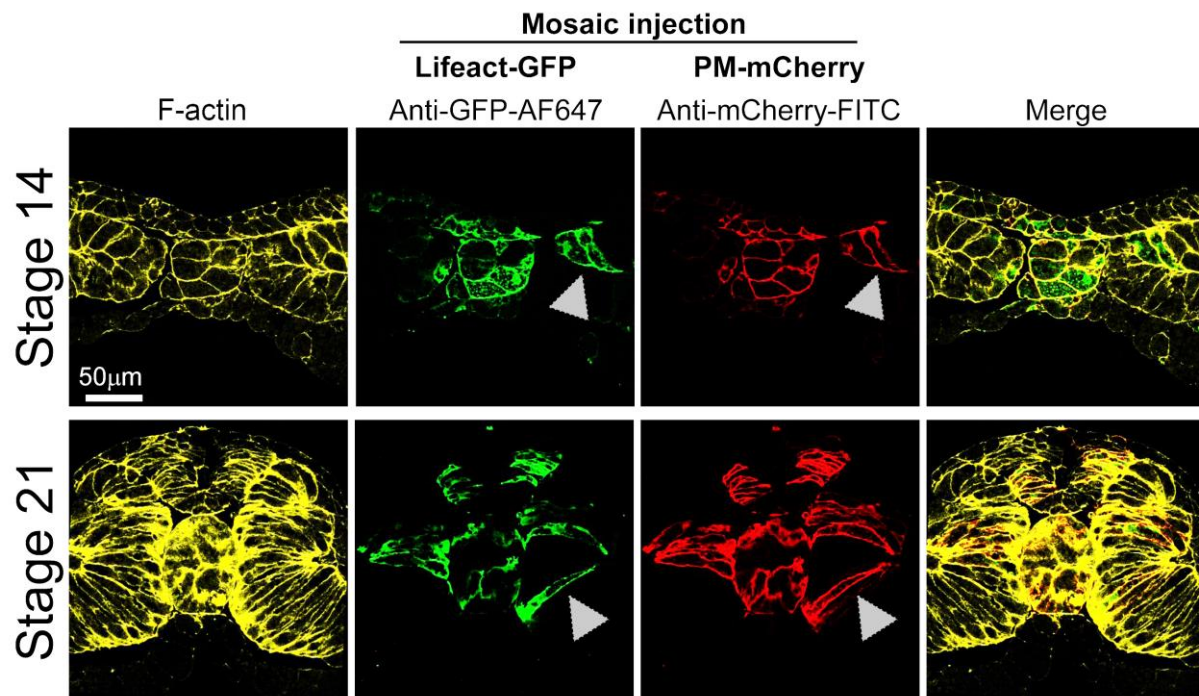


Figure 28. Scatter labeling of plasma membrane and F-actin reporters within dorsal isolates.

Embryos were injected at 16-cell stage with Lifect-eGFP and PM-mCherry and cultured to Stage 14 or 21. After PFA fixation, conjugated antibodies against eGFP and mCherry were used to visualize F-actin and plasma membrane reporters since fluorescence of FPs is quenched during isopropanol dehydration and clearing. Tissues were also stained for total F-actin (phalloidin; yellow channel). Single cells within the PSM are identified (white arrowheads) and imaged under high magnification (63X; 3X optical zoom) for cortex thickness measurements.

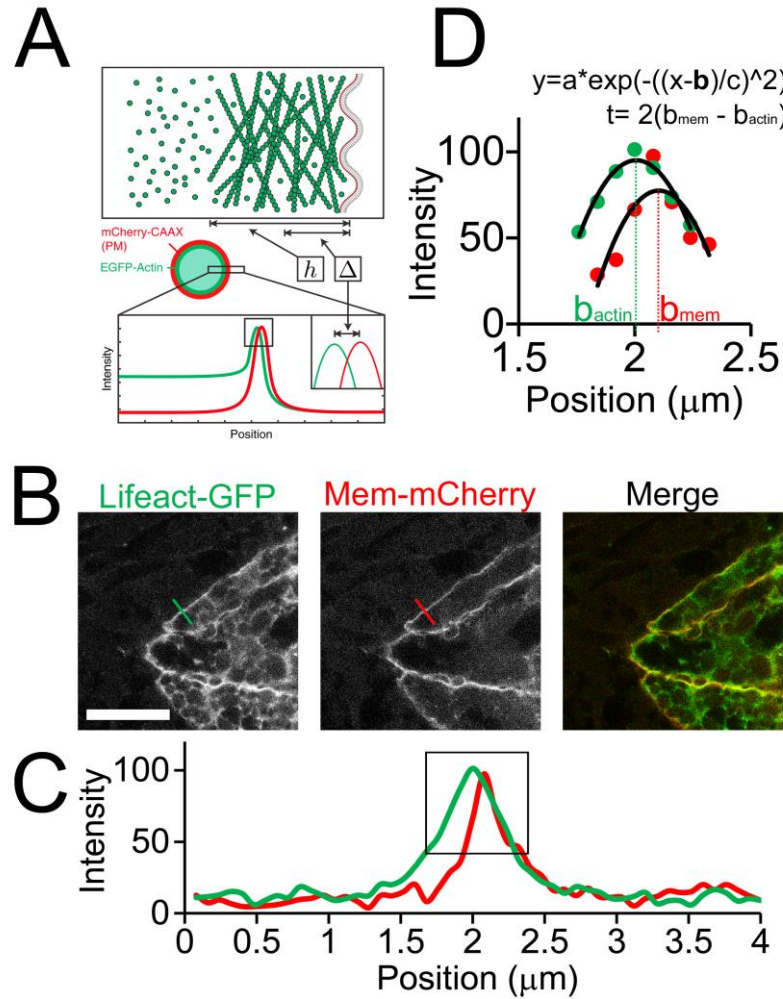


Figure 29. Measuring cortex thickness within mosaically labeled tissues.

A) Schematic from (Clark et al. 2013) showing method of measuring cortex thickness in single isolated HeLa cells. B) Similar approach applied in *Xenopus* mesoderm cells expressing both a membrane label (mem-mCherry) and an f-actin label (Lifeact-GFP). Scale bar 20 μ m. C) The intensity profile across a junction between a cell expressing membrane/actin markers and a non-expressing cell is obtained followed by D) Gaussian fitting around peaks in each channel. Using the Gaussian fit parameters; the separation between the positions of the actin and membrane linescan peaks (b_{actin} and b_{mem}) is obtained and related to cortex thickness (t). X-axis in C and D is arbitrary distance along line profile.

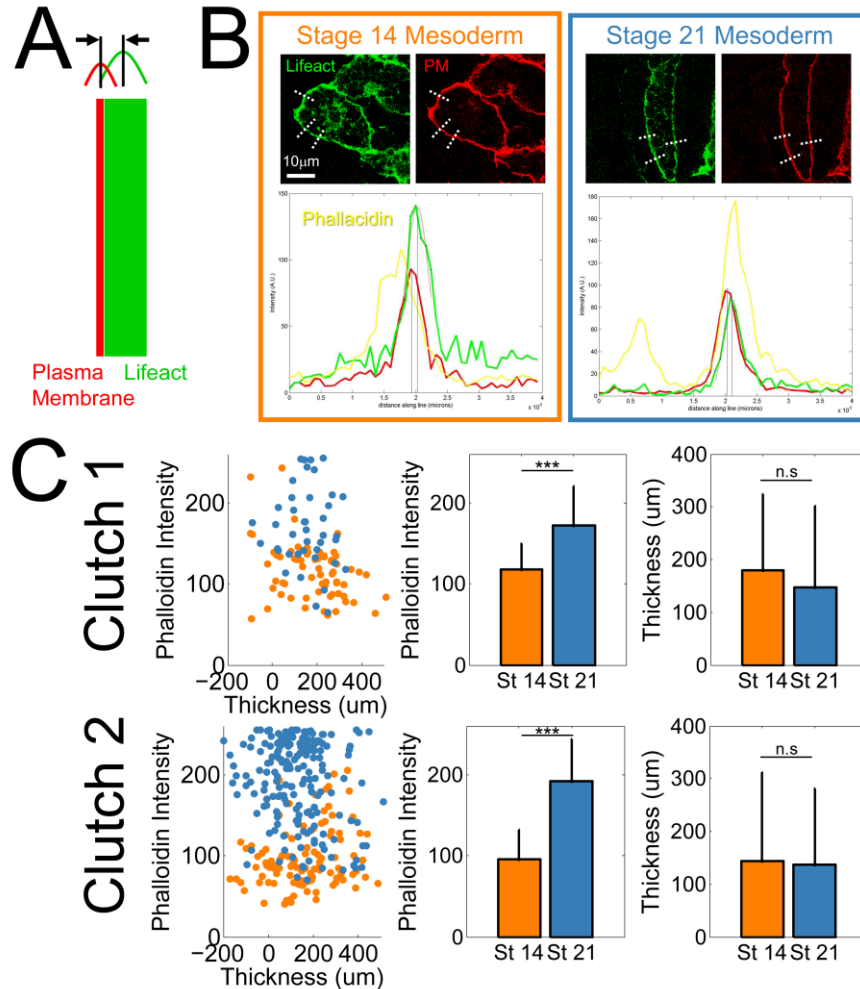


Figure 30. Cortex thickness unchanged within mesoderm.

A) Cortex thickness is calculated using the intensity profile across a junction between a cell expressing fluorescent proteins for both membrane and Lifect and a non-expressing cell. The center of the plasma membrane and F-actin cortex positions is calculated by Gaussian fitting around peak intensities in each channel. B) Representative z-slices of mosaically labeled cells with example line profiles (dashed white lines) drawn across junctions. Plots represent intensity values vs. position on line profile (red: mem-mCherry; green: Lifect-GFP; yellow: BODIPY FL Phalloidin). C) No relationship between cortex intensity (Phalloidin intensity) and cortex thickness. Cortex intensity increases significantly between stage 14 and 21 (***) p-val < 0.001; Mann-Whitney U test) however cortex thickness does not (Clutch 1: p-val = 0.29; Clutch 2: p-val = 0.27; Mann-Whitney U test). Error bars represent 1 SD.

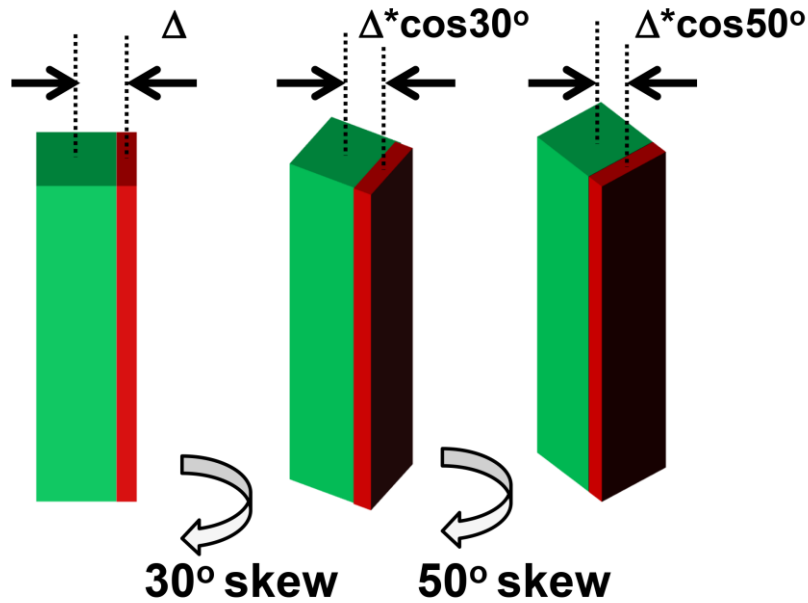


Figure 31. Theoretical effect of cortex angle skew on relative positions of actin and membrane signal.

For cortex thickness measurements, the distance (Δ) between the center of the actin cortex (green) and membrane (red) signal must be measured. If the cortex is not orthogonal to the X-Y imaging plane, as shown in the 30 and 50 degree skew cases, the observed Δ decreases with increased angle skew, compromising cortex thickness measurement. To identify angle skew, cortex position at various z-slices must be obtained.

5.2.3 ACTN1 crosslinking regulates dorsal axis stiffness

Since F-actin intensity in the cortex in the mesoderm increases during neurulation and is known to contribute to the bulk mechanics of dorsal tissues (Zhou et al. 2009), we asked whether the degree of cross linking can control mechanics of the dorsal axis. F-actin crosslinking and bundling can contribute to mechanical properties of reconstituted actin gels, single cells, and tissues. The organization of F-actin networks is coordinated by actin binding proteins that facilitate bundling and cross linking of filaments. *In vitro* studies using rheology to measure viscoelasticity of reconstituted actin gels have shown that increased cross-linking of F-actin

results in stiffer gels (Esue et al., 2009; Gardel et al., 2004; Luan et al., 2008; Wachsstock et al., 1994; Xu et al., 1998) and in cell aggregates (Cunningham et al., 1992). Rheological studies have shown that actin filaments form relatively weak gels at physiological concentrations and thus likely involve F-actin binding proteins to cross-link and bundle actin filaments into stiffer arrays (Xu et al., 2000).

To test the role of F-actin crosslinking, we modulated α -actinin-1 (ACTN1) function using overexpression of wildtype protein and expression of a dominant negative, actin-binding domain deleted form (Figure 34A). We chose α -actinin-1 since its expression increases sharply during neurulation (Session et al. 2016) and is expressed at relatively high levels in the dorsal marginal zone (Popov et al. 2017). Moderate levels of α -actinin-1 overexpression resulted in a 10% increase in mesodermal F-actin intensity (Figure 34B,C; p-val <0.001; One-Sample t-test), and a 39% increase in stiffness (Figure 34D; p-val 0.001) in stage 16 dorsal isolates. Overexpression of α -actinin-1 has been shown to increase density and reduce turnover of actin filaments during cytokinesis in cell culture (Mukhina et al. 2007), suggesting that overexpression inhibits F-actin depolymerization. To test whether overexpression of α -actinin-1 alters turnover at these stages we carried out FRAP analysis in animal cap epithelial cells and found increased half-life and immobile fraction in the apical cortical domain of overexpressing cells (Figure 33), consistent with a role for α -actinin-1 in stabilizing as well as cross-linking the F-actin network. To diminish F-actin cross-linking, we expressed a dominant negative, actin-binding domain deleted α -actinin (Δ ABD-actinin). Δ ABD-actinin has been shown to form heterodimers with endogenous α -actinin, thus inhibiting cross-linking activity (Low et al. 2010). To confirm the function of Δ ABD-actinin we sought to rescue a blastopore closure defect characterized by moderate overexpression of α -actinin-1. We reasoned that Δ ABD-actinin would dimerize and

effectively quench the overexpressed wildtype protein, resulting in a rescued phenotype. We overexpressed both wildtype and dominant negative constructs simultaneously and compared blastopore diameter with embryos overexpressing only wildtype protein and uninjected controls. Overexpression of Δ ABD-actinin rescued the blastopore closure defect, which suggested that Δ ABD-actinin was interacting with and inhibiting wildtype protein function (Figure 32).

Interestingly, overexpression of Δ ABD-actinin resulted in no detectable change in F-actin intensity (Figure 34B,C; p-val <0.15; One-Sample t-test), yet still generated a 27% reduction in stiffness (Figure 34D; p-val 0.005) in stage 21 dorsal isolates, indicating that F-actin cross-linking can control mechanical properties independent of total F-actin density.

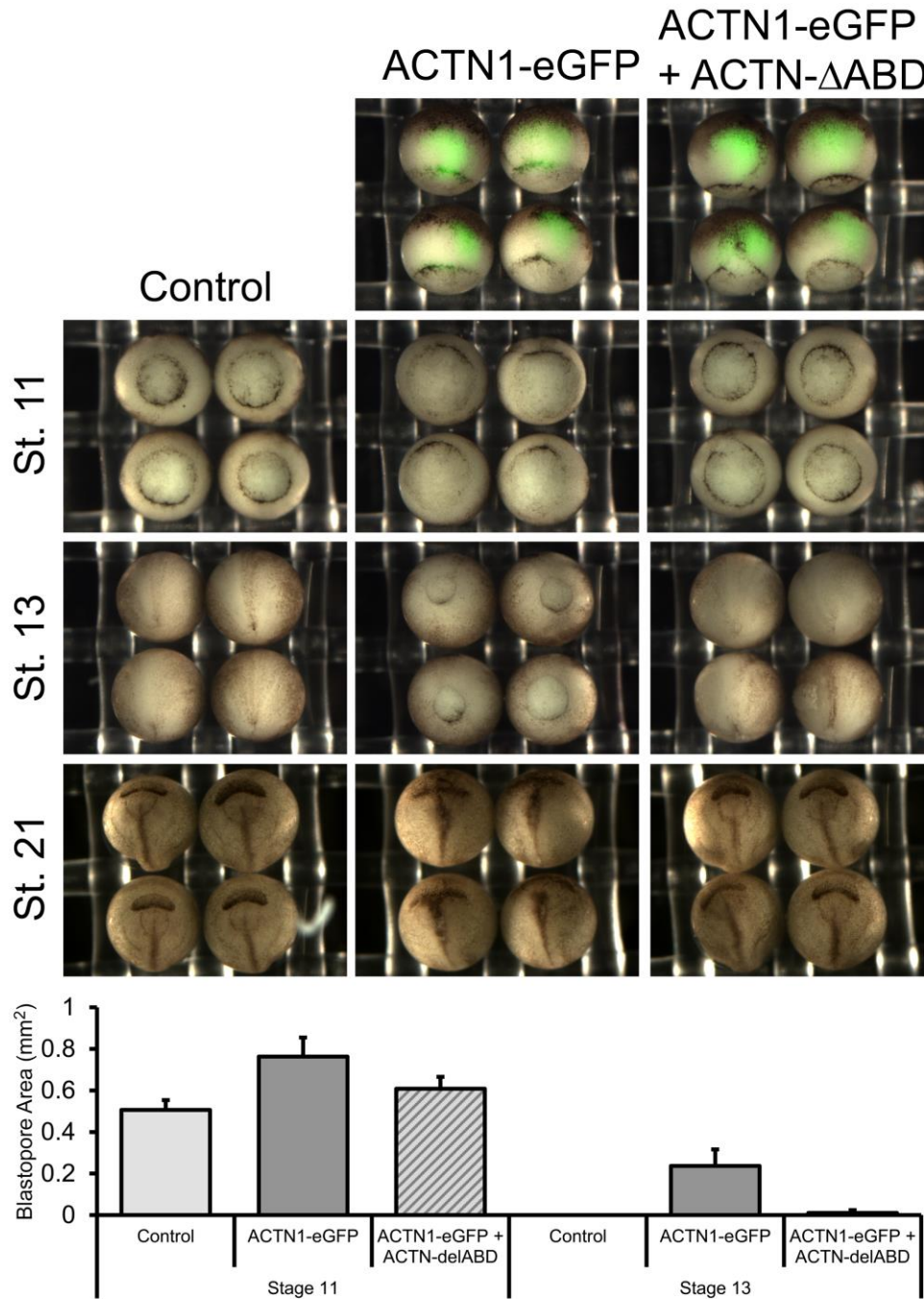


Figure 32. Δ ABD-actinin rescues blastopore closure delay caused by overexpression of α -actinin-1.

Embryos were injected with ACTN1-eGFP or ACTN1-eGFP + ACTN- Δ ABD at the 4-cell stage in the equatorial region of both dorsal blastomeres. Green signal in top row represents tissues overexpressing actinin constructs. Blastopore diameter was compared between embryos to assess degree of rescue (n=4 embryos in each bar).

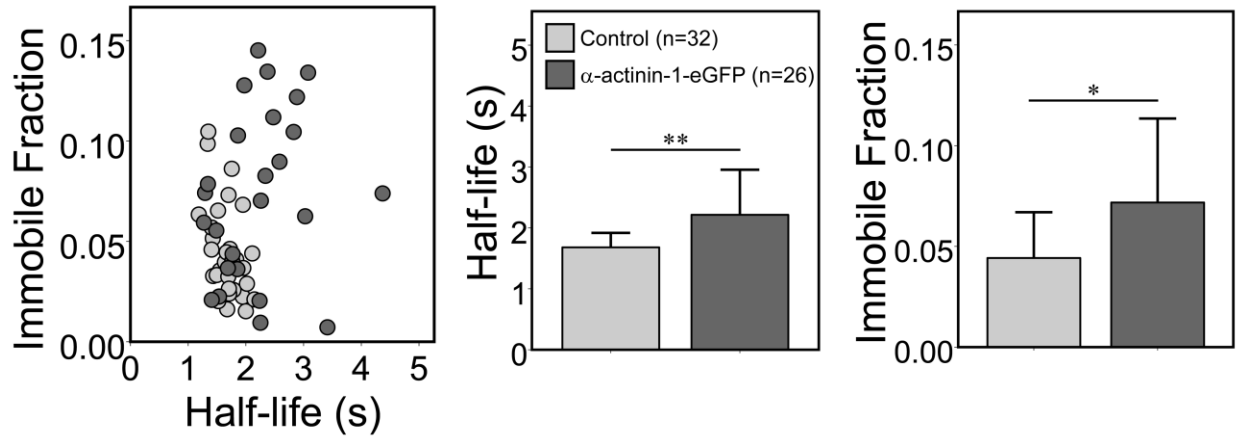


Figure 33. α -actinin-1 overexpression increases cortex stability in animal cap epithelium.

Fluorescent recovery after photobleaching (FRAP) experiments were conducted on apical animal cap epithelial cells overexpressing α -actinin-1 and compared with wildtype controls. To compare groups, Mann-Whitney U test was performed between groups (Half life ** p-val: 0.002; Immobile fraction * p-val: 0.012).

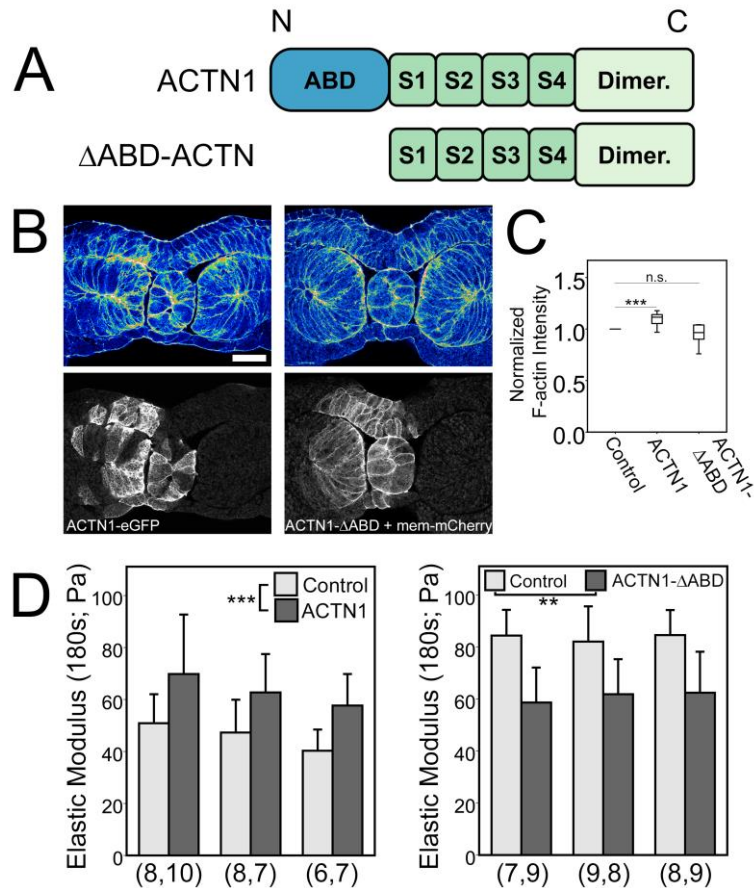


Figure 34. α -actinin-1 cross-linking affects F-actin intensity and tissue modulus.

A) Diagrams of α -actinin constructs used, showing the N-terminal actin binding domain (ABD), C-terminal calmodulin-like dimerization domain (Dimer) and 4 spectrin repeats. For ACTN1 construct, eGFP was at the N terminus. B) Transverse sections of Stage 16 dorsal tissues contralaterally injected with ACTN1 or ACTN1- Δ ABD and stained for F-actin (phalloidin). ACTN1- Δ ABD was coinjected with mem-mCherry. Scale bar 100 μ m. C) F-actin intensity levels of injected cells were compared with contralateral, uninjected cells within mesoderm tissues. F-actin was significantly enhanced in cells injected with ACTN1 (p-val < 0.001; One Sample t-test), but not ACTN1- Δ ABD (p-val = 0.15; One Sample t-test). D) Stage 16 dorsal isolates overexpressing ACTN1 were 39% stiffer than controls (*** p-val < 0.001; 2-way ANOVA). Stage 21 dorsal isolates overexpressing ACTN1- Δ ABD had a 27% reduction in stiffness (** p-val = 0.005; 2-way ANOVA). Each cluster represents one experiment and n value represents number of explants tested per group. Error bars represent 1 S.D.

5.3 DISCUSSION

In this aim, we tested how the F-actin cortex contributes to mechanical properties since the “cell-wall” is predicted by the CSM to be a major contributor to bulk modulus. We measured a substantial increase in the abundance and stability of mesodermal F-actin between Stage 14 and 21, however no difference in F-actin cortex thickness. The mechanism of F-actin enhancement in the dorsal axis remains a mystery however factors such as g-actin expression levels, polymerization/depolymerization rate effectors and F-actin bundling proteins could be at play, none of which are mutually exclusive. To test the contribution of the cell-wall, we modulated F-actin cortex composition by enhancing or diminishing crosslinking by a-actinin-1 and measured a significant increase or reduction in stiffness with levels of crosslinking.

While the predictions of the CSM have been useful in predicting how structural features might influence bulk mechanical properties, the basic equations of the CSM do not capture finer scale organization of materials within a foam. For instance, cortex thickness may be a useful parameter however without having information on F-actin cortex organization, density and degree cross-linking it is challenging to determine bulk mechanical properties of the cell-wall. Interestingly, depletion of four different F-actin crosslinkers known to mediate F-actin gel mechanics did not affect cortex thickness in HeLa cells (Chugh et al. 2017). Additionally, the F-actin cortex of mouse oocytes gets thicker during meiosis I however becomes softer due to the exclusion of myosin-II, indicating that contractility is another important regulator of cortex mechanical properties (Chaigne et al. 2013). F-actin networks can be organized in different types of networks, each with different mechanical properties (Xu et al. 1998; Claessens et al. 2006; Grooman et al. 2012). To better understand the “material” properties of our embryonic tissues,

we turn to studies in reconstituted gels which provide a simpler system to tune parameters such as crosslinking and filament density (Shin et al. 2004).

In this study, we chose to investigate α -actinin-1 however many other crosslinkers and actin-binding proteins ramp up expression during neurulation (Session et al. 2016). The enhancement of F-actin is likely to be regulated by several, potentially redundant mechanisms and could depend on cell identity. Further studies will need to be conducted to understand the extent to which F-actin crosslinking controls bulk modulus in embryonic tissues.

5.4 EXPERIMENTAL PROCEDURES

5.4.1 F-actin staining and intensity measurement

Dorsal isolates were isolated from neurula stage embryos, allowed to heal for 30 minutes and fixed in 4% PFA for 3-4 hours at room temperature. After fixation, explants were washed 3x for at least 15 minutes each with PBST (0.1% Triton-X) and bisected transversely using a razor. Transverse sections were stained with phalloidin (2.5:1000) for at least 1hr at room temperature or overnight at 4 degrees C. After staining, explants were washed 3x for at least 15 minutes each with PBST (0.1% Triton-X) and then dehydrated in 100% isopropanol. Tissue samples were transferred into chambers (made of nylon washers adhered to coverslips using clear nail polish) containing Murray's Clear (2:1 Benzyl Benzoate: Benzyl Alcohol) for imaging.

F-actin intensity was measured in transverse dorsal isolate tissue sections within the presomitic mesoderm (PSM). The mesoderm was chosen since it makes up a large portion of the cross sectional area of the dorsal isolate (~50%) and also because it is the stiffest tissue within

the dorsal axis during neurulation (Zhou et al. 2009). For bulk intensity measurements, transverse sections were imaged using the 25X water objective with 2X optical zoom. FIJI was used to manually draw ROIs around the PSM and measure average pixel intensity.

Finer scale F-actin intensity measurements were collected at higher magnification (63x oil objective with 3X optical zoom) to visualize individual bundles of F-actin cortex. Manual ROIs were drawn along bundles of F-actin cortex and custom algorithms were written to draw perpendicular lines across bundles. Max intensity values across line profiles were averaged across bundles within an entire image

5.4.2 Fluorescence Recovery After Photobleaching

Fluorescence recovery after photobleaching (FRAP) experiments were performed on a laser scanning confocal microscope (SP5; Leica Microsystems) with a 63X oil objective and 3X optical zoom using the FRAP wizard with LASAF software package. A square ROI (5 μ m by 5 μ m) was manually selected within the F-actin cortex of either animal cap epithelium or mesoderm for bleaching (Figure 35). To maximize frame rate, 256 x 256-pixel images were acquired at 700Hz (~0.37 seconds/frame). Bleaching was achieved by zooming in to the square ROI ('zoom-in' feature on software) and exposing the 488nm Argon laser for two time steps (~0.74s). The laser power was set to 25% and the ND filter setting to 100% for bleaching. Five frames were collected before bleaching and 30 frames after at the same frame rate. After acquisition, intensity profiles were analyzed using custom Matlab software to calculate half-life and immobile fraction.

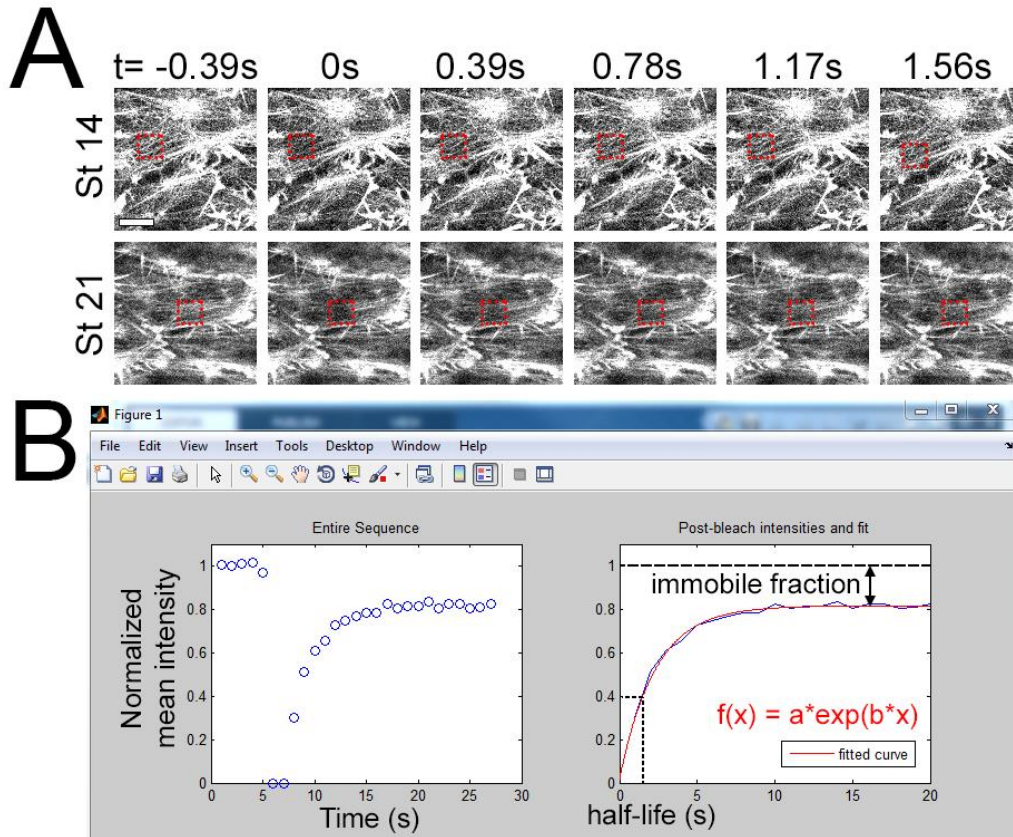


Figure 35. Fluorescence Recovery After Photo-bleaching (FRAP) Experiment.

A) Representative time course of FRAP experiments done in mesoderm at stage 14 and 21. Regions of cortex were bleached (red dashed ROI) and mean intensity within ROI was collected for 30 seconds. FRAP experiment shows ~50% bleach at 0s with full recovery by 1.5 s. Scale bar 10 μ m. B) ROI mean intensity over time was normalized to pre-bleach levels, plotted over time and fit to an exponential function. Immobile fraction and half-life were used for statistical analysis.

5.4.3 Actinin mRNA constructs

α -actinin-1-eGFP (hsACTN1 splice variant 2) was generously provided by Carol Otey (Edlund et al. 2001). The dominant negative mutant lacking the actin binding domain (ACTN1- Δ ABD; amino acids 251-892) was amplified using PCR using α -actinin-1 as a template. ACTN1- Δ ABD

has been shown to form heterodimers with endogenous α -actinin and act as a dominant negative in NRK cells (Low et al. 2010). For overexpression studies, 2ng of α -actinin-1 mRNA or 4ng of α -actinin-1- Δ ABD mRNA was injected into the equator of the 2 dorsal blastomeres at the 4-cell stage. Total volumes of injected mRNA were 4-10nl per blastomere at 4-cell stage.

5.4.4 F-actin Cortex Thickness Measurement

To quantify “cell-wall” thickness, we adapted a method used in single cells to measure F-actin cortex thickness (Clark et al. 2013). Cell cortex thickness measurements within a tissue require mosaic labeling of membrane and actin reporters. Membrane/actin mRNA reporters are injected in one dorsal blastomere at the 16-cell stage to achieve scatter throughout the axis. Regions of cortex within mesoderm tissue are manually selected through confocal stacks of transverse tissue sections. A custom program is used to create perpendicular lines (across the junction) using 5 μ m thickness and 5 μ m spacing and collect intensity along each line scan. Peak positions and intensities are determined by fitting a Gaussian function to the seven points surrounding and including the pixel with highest intensity. Line scans are filtered to ensure a peak is detected in each channel (peak intensity > 4x baseline, where baseline is identified as all points excluding the 7 points surrounding and including the pixel with highest intensity) and goodness of Gaussian fit ($r^2 > 80\%$). Using parameters from the Gaussian fit, we determined the separation between the positions of the actin cortex and membrane, Δ . We assumed that the membrane is negligibly thin; therefore cortex thickness is calculated as $2*\Delta$.

5.4.5 Mechanical testing of tissue explants

For mechanical measurements, dorsal isolates isolated from embryos overexpressing wildtype or mutant α -actinin-1 were loaded into the nNFMD device (described in detail in Section 6.2)(Moore et al. 1995). This device allows us to conduct unconfined uniaxial compressive stress-relaxation tests to measure the time-dependent viscoelastic properties of *Xenopus* embryonic tissues. Tissues were kept at 14 degrees C until testing to ensure testing was conducted at similar developmental stage.

6.0 GENERAL METHODS

6.1 EMBRYOS AND MICROSURGERY

Xenopus laevis embryos were obtained by standard methods (Kay 1991), fertilized in vitro and cultured in 1/3X Modified Barth's Solution (MBS). Embryos are cultured to stage 14 or 21 (Nieuwkoop 1967), at which time dorsal axial and paraxial tissues (dorsal isolate) are microsurgically removed from the embryo using hair loops and knives. Before microsurgery, small (~1x5mm) pieces of glasses are cut from a #1.5 glass slide using a diamond pen. Microsurgically removed dorsal isolate explants contain a consistent tissue organization of ectoderm, mesoderm and endoderm. After isolation, tissue explants are transferred to a clean dish filled with DFA and gently and minimally compressed under a precut small piece of glass using vacuum grease at the ends for half an hour prior to experimentation to allow healing without tissue folding/bending. For microinjection of mRNAs, embryos are placed in 1X MBS containing Ficoll.

6.2 BIOMECHANICAL TESTING- NNFMD

Tissue explants are loaded into the nNFMD device (Figure 36) to test bulk stiffness after our cell size regulation experiments (Moore et al. 1995). This device allows us to conduct unconfined uniaxial compressive stress-relaxation tests to measure the time-dependent viscoelastic properties of *Xenopus* embryonic tissues. This standard stress-relaxation test allows us to obtain data on tissue residual stiffness of these tissues, independent of shape, that are comparable to other data in the literature. During stress relaxation testing, the tissue sample is rapidly compressed to length for the duration of the test while the force required to maintain the compressed length is measured (Findley et al. 1976). For viscoelastic materials, the force required to maintain the compressed length decreases with time due to stress dissipation, resulting in time-dependent resistive force values.

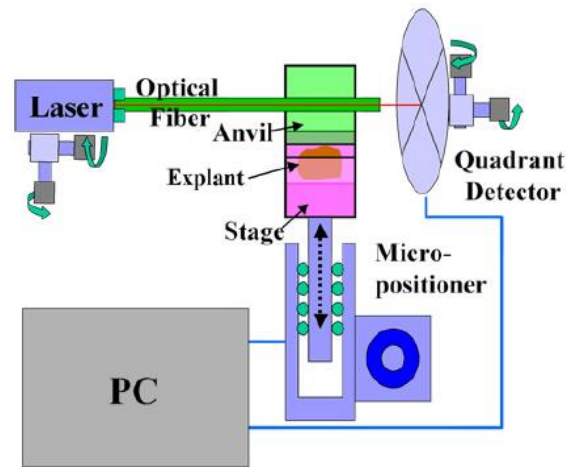


Figure 36. nano-Newton Force Measurement Device (nNFMD).

The nNFMD is used to perform uniaxial unconfined compression stress-relaxation testing on dorsal explants to measure time-dependent Young's modulus. Schematic reproduced from (Davidson and Keller 2007).

The nNFMD has been described in detail previously (Davidson and Keller 2007). In brief, this device consists of an optical fiber that acts as a force transducer. The spring constant of the fiber is measured using Hooke's law by adding successive strips of wire of known mass at the end of the fiber and measuring the deflection. During testing, the deflection of the optical fiber is measured in the x- and y- direction with a laser-quadrant detector. A Labview VI is used to communicate between the hardware and software in this system. A closed-loop servo micro positioner with encoder is used to move the tissue sample against the force transducer to initiate compression. To measure viscoelastic properties of the tissue explants we compress tissue samples ~15-20% along its anterior-posterior axis and calculate the resistive force using the measured deflection of the force transducer. The tissue samples are visualized with a camera during the compression test to obtain measurements before and after compression. Immediately after testing, explants are fixed in 4% paraformaldehyde (PFA), transversely bisected and imaged under stereomicroscopy to obtain cross-sectional area of the explants. A time dependent Young's modulus is then calculated using measured resistive force, cross-sectional area and strain measurements (Figure 11).

Based on prior characterization of *Xenopus* embryonic tissues (Moore et al. 1995; Zhou et al. 2009) and confirming here, we find that resistive force after compression spikes instantly and exponentially decays until approximately 180 seconds when the resistive force plateaus. We assume that embryonic tissues exhibit linear viscoelastic behavior and thus, the time-dependent relaxation modulus can be fitted to a standard linear solid (SLS) model (Findley et al. 1976), consisting of a spring in parallel with a Maxwell element (spring and dashpot in series). While the SLS model generally fits the relaxation modulus of embryonic tissues, there many examples of unpredictable tissue-level contractions during testing which confound model fit. Contractions

can arise due to extracellular ATP (Joshi et al. 2010) caused after microsurgery and can result in an elevated transient resistive force, compromising SLS model fit parameters. For this reason, we compare the measured Young's modulus at 180 seconds, E(180) rather than using SLS fit parameters.

Statistical tests of significance are conducted using two-way ANOVA with drug treatment as a fixed factor and clutch as a random factor. Generally, at least three clutches are used to compare stiffness between groups (plotted as clusters along the X-axis. We confirmed normality of the dependent variable (E(180)) across ten clutches of Stage 14 control dorsal isolates (n= 82; Shapiro-Wilk test for normality sig. 0.057). Sources of error may arise from natural variation in the mechanical properties between individual embryos and/or experimental error due to slight mistiming of tissue explant isolation.

7.0 SUMMARY AND CONCLUSIONS

7.1 SUMMARY OF FINDINGS

In this study, we took a multiscale approach to understand how the embryo stiffens dramatically during neurulation through three specific aims (Section 1.3). We confirmed a 150% stiffening during neurulation and compared the mechanics of dorsal embryonic tissues to foams governed by the Cellular Solids Model (CSM) to make predictions on how structural features at different size scales contribute to the bulk mechanical properties. The CSM predicts that changing architecture of the dorsal axis would not contribute to modulus since bulk mechanical properties depend on constituent cells rather than the organization in which they are arranged. Chapter 2 focuses on reviewing efforts to quantify adhesion mechanics from the subcellular to tissue level in developing embryos.

In Chapter 3, we directly test the hypothesis developed in Aim 1 regarding the contribution of tissue architecture to bulk modulus. We confirmed that tissue architecture is not an important mechanical feature in dorsal embryonic tissues by scrambling native architecture using a novel dissociation and reaggregation assay to generate brick-shaped tissues void of any coherent structures. Scrambled tissues also shed light on the robustness of developmental programs such as laminin and fibrillin synthesis and somite differentiation to altered microenvironments. We conclude that tissue architecture is not important for maintaining tissue

modulus in early and late stage dorsal isolate tissues, however tissue architecture is important for stiffening the embryo since scrambled tissues failed to stiffen to native levels in culture. The result that architecture is not important for modulus of embryonic tissues allowed us to confirm the central hypothesis of the CSM and move on to testing predictions about cell size and “cell-wall” thickness.

In Chapter 4, we develop approaches to generate tissues with larger and smaller cells by manipulating the cell cycle to directly test our Aim 2 hypothesis concerning the role of cell size on modulus. Tissues with controlled cell sizes exhibited moduli consistent with CSM predictions however we found that the stiffening during neurulation cannot be explained by decreasing cell size.

We concluded by testing our Aim 3 hypothesis about how the F-actin cortex contributes to mechanical properties in Chapter 5. The F-actin cortex represents the “cell-wall” and is predicted by the CSM to be a major contributor to bulk modulus. We measured a substantial increase in the abundance and stability of mesodermal F-actin between Stage 14 and 21. We modulated F-actin cortex composition by enhancing or diminishing crosslinking by α -actinin-1 and measured a significant increase or reduction in stiffness with levels of crosslinking. The CSM pointed us towards the F-actin cortex as the major contributor to stiffening however this approach simplifies the complex organization of the F-actin cortex. The mechanism of F-actin enhancement in the dorsal axis remains a mystery however factors such as g-actin expression levels, polymerization and depolymerization rate effectors and F-actin bundling proteins could be at play, none of which are mutually exclusive. Crosslinked F-actin networks can be organized into mesh-like gels, branched networks or parallel bundles, each with different mechanical responses. The degree to which F-actin networks are crosslinked is challenging to assess within

tissues using conventional confocal microscopy. Future studies are required to explore the role of other actin-binding proteins, including cross-linkers, end-cappers, polymerizing factors etc. and their effects on tissue- and stage-dependent changes in bulk modulus of embryonic tissues.

7.2 SIGNIFICANCE OF FINDINGS

Animal morphogenesis requires the deformation and displacement of tissues to form complex tissue architectures critical for shaping the embryo. These orchestrated tissue displacements rely on the regulation of embryonic tissue mechanical properties (Koehl 1990; Davidson 2011). For this reason, it is important to understand which features of the embryo are contributing to mechanical feedback, important for guiding development. Through the three specific aims presented, we tested how structural changes occurring during stages of stiffening contribute to bulk mechanical properties. We compared the mechanics of embryonic tissues to solid cellular foams and made predictions about mechanical properties based on the Cellular Solids Model.

First, we found that tissues devoid of their native architecture maintain the same bulk mechanical properties as unaltered native tissues and can also stiffen over time, albeit not to the full extent of native tissues. These findings suggest that tissue architecture, e.g. laminar organization and germ layer shape, may not provide additional mechanical resistance beyond the contribution of constituent cells. The source of bulk mechanical properties of tissues resides within intrinsic cells rather than any larger multi-cell micro anatomical features. The inability for scrambled tissues to stiffen to native levels remains a mystery, but potential explanations are explored below in Future Directions.

Second, we find that reductive cell division is not likely to be a mechanism of stiffening during neurulation. By manipulating cell cycle, we generated tissues with slightly larger and smaller cells compared with native tissues and found that these tissues confirm bulk stiffness predictions of the CSM but are only responsible for a modest 20% increase in stiffness from early to late neurulation. While we maintain that cell size may be a potent regulator of stiffness, the amount to which cells divide in the dorsal axis of *Xenopus laevis* embryos during neurulation is not sufficient to drive bulk mechanical changes.

We conclude that regulation of the F-actin cortex is a major contributor to tissue mechanical properties during neurulation and that specifically, F-actin crosslinking regulates stiffness of embryonic tissues. It will be critical to understand the composition of the F-actin cortex during development to understand how both stiffness and force generation are regulated during morphogenesis. Understanding the physical principles of embryonic tissues and the specific regulators of mechanical feedback will be important for engineering de novo tissues.

7.3 FUTURE DIRECTIONS

Through this work, we sought to elucidate structural and molecular factors that regulate tissue stiffening during neurulation. We have ruled out the contribution of changing tissue architecture and decreasing cell size to bulk tissue stiffening. We have demonstrated that F-actin is dramatically enhanced during neurulation, correlated with a 150% increase in stiffness and test the role of F-actin crosslinking on mechanics. This work has led to other questions that must be addressed to elucidate the mechanisms of stiffening:

How is the F-actin cytoskeleton regulated in the dorsal axis during neurulation?

More studies need to be carried out to understand the mechanism of F-actin enhancement and precisely how F-actin cortex composition contributes to bulk properties. Theoretical models and experiments in reconstituted F-actin gels prove that modulus depends on filament length (Kasza et al. 2010) and cross-linker density (Gardel et al. 2004). Since there are many F-actin crosslinkers that differentially bind and organize F-actin (Stossel et al. 1985), and potential redundancy (Rivero et al. 1999; Tseng et al. 2002), it is challenging to study how crosslinking generally influences stiffness of embryonic without choosing specific proteins to perturb. With the advent of increased spatio-temporal deep sequencing data (Session et al. 2016; Popov et al. 2017), it will be helpful to identify and compile a panel of proteins that increase in expression during stages of interest and test their contribution to stiffening.

How do bulk tissue-level mechanics influence cell level behavior?

Our mechanical measurements are based on whole tissue compression which is important for understanding tissue level feedback that integrates the mechanics of groups of cells. These measurements can be thought of as an average modulus across all tissues throughout the axis. Regulation of mechanical properties of specific regions of tissue may be important to development however bulk stiffness measurement would not reveal these changes. Microindentation (Filas et al. 2015; Zamir and Taber 2004) and microaspiration (von Dassow and Davidson 2009) are alternative techniques that have been used to obtain stiffness measurements in embryos on a smaller scale and may reflect the stiffness that cells sense. It remains unclear how changing bulk properties are regulated and sensed at the cellular level, however there have been proposed mechanisms. One example of a potential mechanical

feedback mechanism at the tissue level is the regulation of cell growth control within tissues (Shraiman 2005). For example, cells within a tissue that grow faster or slower than surrounding tissue are subject to increased pressure. This increased pressure may be sensed through mechanotransduction pathways (Hamill and Martinac 2001) and alter the cells behavior to correct for aberrant growth patterns. An interesting feature of the converging and extending (C&E) dorsal axis of the *Xenopus* embryo is that component germ layers, including neural ectoderm (Elul et al. 1997; Keller and Danilchik 1988) and mesoderm, are capable of driving C&E movements in isolation. To maintain integrity, there could be mechanical feedback that enables the individual C&E machines to remain coordinated. Investigating the mechanical coordination between germ layers at the tissue level and how these signals are transmitted to the cell level will be useful for understanding mechanical feedback systems in development.

What aspects of tissue architecture are important for mechanical maturation?

To elucidate the role of bulk tissue architecture on mechanical properties, we measured the stiffness of scrambled tissues devoid of large scale microanatomical structures. These experiments revealed that scrambling tissues at stage 14 and stage 21 had no influence on the bulk stiffness since they could recapitulate the stiffness of native stage-matched tissues. Scrambled tissues however were not able to reorganize or stiffen to the full extent of native tissues over time, suggesting that the organization of germ layers or germ layer tissue shape might be important for mechanical maturation. It remains unclear what aspects of architecture facilitate stiffening however could be organization of the ECM or facilitation of bulk morphogenesis movements. Fibronectin, the most abundant ECM protein during gastrulation and neurulation, does not directly contribute to mechanical properties (Zhou et al. 2009) however

proper signaling from the ECM may be important for mechanical maturation of the cytoskeleton. Additionally, since scrambled tissues do not undergo large-scale morphogenetic movements, they may be deprived of native stresses that serve to stiffen the tissues. I sought to test the role of convergence on the stiffening of a native tissue explant by embedding dorsal isolates in 1% agarose gels for several hours to inhibit convergence extension. Unfortunately, it was difficult to reliably remove explants from agarose gels without damaging them and was thus difficult to make stiffness measurements.

Understanding what aspects of the native cell microenvironment are important for guiding tissue form and function will be very informative for engineering novel tissues for regenerative medicine. Organoids made from iPSC's are currently being developed as an *in vitro* model of development and disease however it has been difficult to recreate biophysical and biochemical cues of the native microenvironment (Fatehullah et al. 2016). There are many components of the stem cell niche that are important for form and function including secreted factors, cell contacts, mechanical inputs and spatial cues (Jones and Wagers 2008). Efforts are underway to engineer materials used in stem cell culture to guide differentiation based on substrate stiffness, topography and chemical functionality (Murphy et al. 2014). Understanding how the embryo physically sculpts it form through the cross-talk between mechanics and molecular regulation within the cell microenvironment will teach us important principles for tissue engineering and regenerative medicine approaches.

APPENDIX A

PROTOCOLS AND IMAGE ANALYSIS

This appendix contains the protocol for generating scrambled tissues (Section 3.4.1) and Matlab codes for analyzing fluorescent recovery after photo bleaching (FRAP) experiments (Section 5.4.2) and cortex thickness measurements (Section 5.4.4).

A.1 GENERATING SCRAMBLED TISSUES

A.1.1 Fabricating Scrambled Tissue Chamber

Materials to fabricate X chambers:

- Hot plate with aluminum foil on it
- X number of yellow tips
- X number of 1.5ml ependorf tubes
- PDMS polymer and cross linking agent
- Scissors

1. Turn on hot plate to 5-6 and put aluminum foil on it.
2. Cut off top part of yellow tip with scissors
3. Once hot, melt the bottom of the tip to seal it shut (approx. 2cm in).
4. Make sure the tip fits inside the a closed ependorf tube (shorten if need be)
5. Repeat steps 2-4 for X number of chambers you want to create
6. Mix ($X * 0.5\text{ml}$) of PDMS with ($X * 0.05\text{ml}$) PDMS cross-linker and mix vigorously
7. De-gas the solution in the vacuum until no bubbles in the PDMS
8. Pour 0.5ml of liquid PDMS in each ependorf tube and then insert the yellow tip into each of them.
9. Close the ependorf tube (ideally so that the circle holder in the bottom of the ependorf tube cap holds the yellow tip upright).
10. Allow PDMS to cure for 2 days at room temperature (can be accelerated by putting them in the 37 degree incubator)
11. (Should be done day of experiment) Create 2% agarose solution and add 2ul of green dye. Micropipette 50ul of hot liquid agarose into yellow tip chamber and immediately move the chamber to the centrifuge and spin for 10 min at 5G. Note: Orient the ependorf tube in a repeatable way in the centrifuge because you will want to centrifuge the cells at the same orientation so that the disk of cells lies flat on the agarose.

A.1.2 Generating Scrambled Tissues

1. Isolate 12-14 dorsal isolate tissues at stage 14

2. Immediately transfer dorsal isolates in calcium and magnesium ion free (CMF) DFA solution for 5-7 minutes until epithelial layer begins to peel off then manually finish peeling off the epithelium and discard.
3. Manually ‘chop up’ the tissues with hair tools.
4. Transfer the dissociated tissues to the yellow tip chamber using a 50ul micropipette (cut the tip off so the diameter is not so small) in CMF DFA.
5. Lightly vortex the cells then lightly spin down using small microcentrifuge.
6. Replace CMF DFA with regular DFA 3x
7. Centrifuge at 5g for 10 min
8. Remove chamber and wiggle the tissue loose by micropipetting up and down using a 50ul micropipette. Once loose, physically tip the chamber upside down slowly to allow the tissue to flow to the top of the yellow tip and then aspirate it out with a transfer pipette.

A.2 FRAP IMAGE ANALYSIS CODE

For FRAP experiments, .csv files were directly saved from Leica software after each ROI acquisition. The following code was written in Matlab to analyze the ROI intensity after photobleaching. The user is prompted to select a directory which includes .csv files to analyze. The code analyzes each csv file within and outputs tau, immobile fraction, mobile fraction and half-life for each ROI in one variable titled “Results.”

```
clear  
clc
```

```

%%Results file output in columns: Tau    MobileFrac    ImmobileFrac    Half-Life
A    I0

%%% _1 means ROI1 --> ROI of interest
%%% _2 means ROI2 --> Whole ROI of imaging
folder_name = uigetdir('\rambai\DavidsonShare\Joe Shawky\140925- FRAP alpha-actinin','Pick Directory with files you want to analyze');
allFiles=dir(folder_name);

numFiles=size(allFiles);

for j = 1:numFiles(1)
    %if allFiles(j).isdir == 0
    if strfind(allFiles(j).name,'csv') > 2

        WholeSeries = csvread(strcat(folder_name,'/',allFiles(j).name),2,1);

        s= size(WholeSeries);

        %%find timepoints
        zeros= find(WholeSeries(:,1)==0);
        bleachpoints=size(zeros);

        a(j)= zeros(1)-1;
        b(j)= bleachpoints(1);
        c(j)= s(1)-a(j)-b(j);

        timepoints= [a(j) b(j) c(j)];

        %%how many seconds/timepoint?
        timescale= 0.391;

        %%Calculate the bleach due to Imaging
        preB_2= WholeSeries(1:timepoints(1),2);
        postB_2=
WholeSeries(timepoints(1)+timepoints(2)+1:sum(timepoints),2);
        PreandPostB_2= cat(1,(preB_2),(postB_2));
        howManyXPoints= size(PreandPostB_2);
        imagingBleach= polyfit(transpose(1:howManyXPoints(1)),
PreandPostB_2(:,1),1);

        %%Correct for bleaching due to imaging
        for i= 1:sum(timepoints)
            if WholeSeries(i) ~= 0
                WholeSeriesBleachCorrected(i)= WholeSeries(i) -
imagingBleach(1)*i;
            end
        end
        WholeSeriesBleachCorrected= transpose(WholeSeriesBleachCorrected);

        %%Normalize data
        preB_1= WholeSeriesBleachCorrected(1:timepoints(1),1);

```

```

baseline= mean(preB_1);
WholeSeriesBleachCorrectedNorm= WholeSeriesBleachCorrected/baseline;

%%Fit the postBleach ROI to exponential
postBleach_1=
WholeSeriesBleachCorrectedNorm(timepoints(1)+timepoints(2)+1:sum(timepoints),
1);

str=num2str(postBleach_1(1));
equation= strcat(str, '+a*(1-(exp(-b*(x-1))))');
f= fit(transpose(1:20),postBleach_1(1:20), equation);
coeffvals = coeffvalues(f);

%%worked out numbers for the fit
for k = 1:timepoints(3)
    fitnums(k)= postBleach_1(1) + coeffvals(1) * (1-(exp(-
coeffvals(2)*(k-1))));
end

fit = goodnessOfFit(transpose(fitnums),postBleach_1, 'MSE');

tau= coeffvals(2) * timescale;
A= coeffvals(1);

mobilefrac= A + postBleach_1(1);
immobilefrac= 1- mobilefrac;

halfA= coeffvals(1)/2 + postBleach_1(1);

halflife= 1.0 - (1.0*log(1.0 - (1.0*(halfA -
postBleach_1(1))/coeffvals(1)))/coeffvals(2));
halflife= halflife*timescale;

Results(j,:)= [ tau mobilefrac immobilefrac halflife A
postBleach_1(1) fit];

%     Names(j)= allFiles(j).name;

end
clearvars -EXCEPT Results folder_name allFiles numFiles Names a b c f
end

```

A.3 CORTEX THICKNESS CODES

For cortex thickness measurements, 3 sets of code are implemented:

1. *Fiji macro* to extract junction linescans in membrane, Lifeact and phalloidin channels.

Before running this code, the user manually draws line ROIs across junctions between labeled and unlabeled cells and saves each ROI in the ROI manager. The code generates perpendicular line segments for each line in the ROI manager at the specified line width and spacing. This code outputs .txt files for each line scan.

2. **Matlab code #1** to calculate cortex thickness for all linescans.

The user is prompted to select the directory with .txt files to analyze. Pixel scale must be specified for each experiment. The output of this code is a variable titled “ThicknessFinal” which includes cortex thickness, max intensity, goodness of gaussian fits and peak to background ratio for each channel.

3. **Matlab code #2** that sorts data based on exclusion criteria described in Section 5.4.4.

Before running this code, data from “Thickness Final” (Matlab code #1) is compiled and saved as a new variable titled All14 or All21, based on explant developmental stage. The output of this code is a data table with thresholded data based on exclusion criteria and plots of phalloidin intensity and cortex thickness.

Fiji macro:

```
//ALWAYS DRAW ROI LINES CLOCKWISE TO CELL CENTER SO THAT  
PERPENDICULAR LINESCANS BEGIN OUTSIDE CELL OF INTEREST
```

```
SingleID = getImageID();  
nrois=roiManager("count");  
run("Set Scale...", "distance=0 known=0 pixel=1 unit=pixel");  
SaveFolder=getDirectory("Choose a Directory");
```

```
spacing=5;  
length=25;  
thickness=10;  
for(i=0;i<nrois;i++)
```

```

{
//selectImage(SingleID);
roiManager("Deselect");
roiManager("Select", i );
JunctionName= Roi.getName;
print(JunctionName);
Roi.getCoordinates(Jx, Jy);

Jdist=newArray(Jx.length);
for (qq=0; qq<Jx.length ; qq++)
{
    Jdist[qq]= sqrt(pow((Jx[qq]-Jx[0]), 2) + pow((Jy[qq]-Jy[0]), 2));
}
Array.getStatistics(Jdist,Jmin,Jmax);
if (Jmax>spacing)

{
roiManager("Deselect");
roiManager("Select", i );
run("Set Measurements...", "area centroid fit redirect=None decimal=2");
run("Line to Area");
run("Measure");
junctionangle=getResult("Angle");
roiManager("Deselect");
roiManager("Select", i );
//run("Enlarge...", "enlarge=1");
run("Interpolate", "interval="+spacing);
roiManager("Update");
roiManager("Select", i );
    Roi.getCoordinates(e, f);
    setBatchMode(true);
    for (g=0; g<e.length-1; g++)
    {

        makeLine(e[g],f[g],e[g+1],f[g+1]);

        run("Set Measurements...", "area mean min centroid integrated redirect=None
decimal=3");
        run("Measure");
        x= getResult("X");
        y = getResult("Y");
        L = getResult("Length");
        pi=4*atan(1);
        segangle=getResult("Angle");
        if (segangle<0)
        {

```

```

        segangle=180+segangle;
    }

    angle=getResult("Angle")*pi/180;

    w= length*sin(angle);
    h =length*cos(angle);

    y1=y-h;
    x1=x-w;
    y2=y+h;
    x2=x+w;

    selectImage(SingleID);
    makeLine(x1,y1,x2,y2,thickness);
    run("Add to Manager");

    }
}

}
print(nrois);

/*
for(i=0;i<nrois;i++)
{
roiManager("Select", 0);
roiManager("Delete");
}
*/

////////////////////////////////////

num_roisNew=roiManager("count");
MemChan = 1;
ActChan = 2;
PhallChan= 3;

for (i=nrois; i<num_roisNew; i++) //starts with first orthogonal line
{
roiManager("Select", i );
roiName=getInfo("roi.name");
//Dialog.create("Which channel's which?");
//if (channels==2)
//{

```

```

//      Dialog.addChoice("Which channel is Membrane?", newArray("1", "2"));
//      Dialog.addChoice("Which channel is Actin?", newArray("1", "2"),"2");
//}
//
//else if (channels==3)
//{
//      Dialog.addChoice("Which channel is Membrane?", newArray("1", "2", "3"));
//      Dialog.addChoice("Which channel is Actin?", newArray("1", "2", "3"),"3");
//
//}
//Dialog.show();
//MemChan = Dialog.getChoice();
//ActChan = Dialog.getChoice();

Stack.setChannel(MemChan);
MemInt= getProfile();

Stack.setChannel(ActChan);
ActInt= getProfile();

Stack.setChannel(PhallChan);
PhallInt= getProfile();

Array.show("Results",MemInt,ActInt,PhallInt);

selectWindow("Results");

if(i<10)
{
    //save("C:\\Users\\Joe          Shawky\\Box          Sync\\From          DB\\Lab
Stuff\\Memthickness_Matlab\\0" + i + ".txt");
    save(SaveFolder+ "0" + (i-nrois) + "_" + roiName + ".txt");
}
else
{
    //save("C:\\Users\\Joe          Shawky\\Box          Sync\\From          DB\\Lab
Stuff\\Memthickness_Matlab\\" + i + ".txt");
    save(SaveFolder+ (i-nrois) + "_" + roiName + ".txt");
}
}
roiManager("Save", SaveFolder+"\\RoiSet.zip");

```

Matlab code #1:

```
clear
clc

%size of pixel in microns to nearest 1/100th
res= 0.08E-6;
PeakThresh= 2; %% used to threshold peaks. Only accepts peaks that are
greater than baseline mean + sd times this number

% J = dir('*.txt');
% SizeROIs= size(J);
% numROIs= SizeROIs(1);
folder_name = uigetdir('D:\Data\CortexThickness');
J = dir([folder_name, '*.txt']);
SizeROIs= length(J(not([J.isdir])));
mkdir (folder_name, 'Plots')
path = strcat(folder_name, '\Plots');
micron= round((1E-6/res))/2;

[upperPath, deepestFolder, ~] = fileparts(folder_name);

% SizeROIs= 5;

for i=0:SizeROIs-1
    filename= fullfile(folder_name, J(i+1).name);
    A = importdata(filename);

    MemInt= A.data(:,1);
    ActInt= A.data(:,2);
    PhallInt= A.data(:,3);

    length= numel(MemInt);
    xvar= 0:res:res*length-res;

    [MaxMem, MaxMemPos]= max(MemInt);
    [MaxAct, MaxActPos]= max(ActInt);
    [MaxPhall, MaxPhallPos]= max(PhallInt);

    BaselineMem= vertcat((MemInt(1:MaxMemPos-3)),
(MemInt(MaxMemPos+3:length)));
    BaselineAct= vertcat((ActInt(1:MaxActPos-3)),
(ActInt(MaxActPos+3:length)));
    BaselinePhall= vertcat((PhallInt(1:MaxPhallPos-3)),
(PhallInt(MaxPhallPos+3:length)));

    AverageBaselineMem= mean(BaselineMem);
    AverageBaselineAct= mean(BaselineAct);
    AverageBaselinePhall= mean(BaselinePhall);

    SDBaselineMem= std(BaselineMem);
    SDBaselineAct= std(BaselineAct);
```

```

MemIntDeconv = MemInt;
ActIntDeconv = ActInt;

[maxM, IM] = max(MemIntDeconv);
[maxA, IA] = max(ActIntDeconv);
[maxPh, IPh] = max(PhallInt);

if IM < micron+10 || IM > length-micron-10
    continue
elseif IA < micron+10 || IA > length-micron-10
    continue
elseif IPh < micron+10 || IPh > length-micron-10
end

Figure1= figure;
p1=plot(xvar,MemInt, '-r', 'LineWidth',1);
hold on;
plot(xvar,MemIntDeconv, '-r', 'LineWidth',3);
p2=plot(xvar,ActInt, '-g', 'LineWidth',1);
plot(xvar,ActIntDeconv, '-g', 'LineWidth',3);
plot(xvar,PhallInt, 'y', 'LineWidth',2);

MemGauss(1)= MemIntDeconv(IM-3);
MemGauss(2)= MemIntDeconv(IM-2);
MemGauss(3)= MemIntDeconv(IM-1);
MemGauss(4)= maxM;
MemGauss(5)= MemIntDeconv(IM+1);
MemGauss(6)= MemIntDeconv(IM+2);
MemGauss(7)= MemIntDeconv(IM+3);

ActGauss(1)= ActIntDeconv(IA-3);
ActGauss(2)= ActIntDeconv(IA-2);
ActGauss(3)= ActIntDeconv(IA-1);
ActGauss(4)= maxA;
ActGauss(5)= ActIntDeconv(IA+1);
ActGauss(6)= ActIntDeconv(IA+2);
ActGauss(7)= ActIntDeconv(IA+3);

[MemFit,MemGOF] = fit([xvar(IM-3);xvar(IM-2);xvar(IM-
1);xvar(IM);xvar(IM+1);xvar(IM+2);xvar(IM+3)],transpose(MemGauss),'gauss1');
[ActFit,ActGOF] = fit([xvar(IA-3);xvar(IA-2);xvar(IA-
1);xvar(IA);xvar(IA+1);xvar(IA+2);xvar(IA+3)],transpose(ActGauss),'gauss1');

plot(MemFit,[xvar(IM-3);xvar(IM-2);xvar(IM-
1);xvar(IM);xvar(IM+1);xvar(IM+2);xvar(IM+3)],MemGauss)
plot(ActFit,[xvar(IA-3);xvar(IA-2);xvar(IA-
1);xvar(IA);xvar(IA+1);xvar(IA+2);xvar(IA+3)],ActGauss)

legend OFF
xlabel('distance along line (microns)')
ylabel('Intensity (A.U.)');
if(i==0)
legend([p1,p2], 'Membrane', 'Actin');end

```

```

Memcoefs= coeffvalues(MemFit);
MemPos = Memcoefs(2);

Actcoefs= coeffvalues(ActFit);
ActPos = Actcoefs(2);

line([MemPos MemPos],[0 Memcoefs(1)]);
line([ActPos ActPos],[0 Actcoefs(1)]);

% %%Convert filename to num
% out=regexp(filename,'\d+','match');
% NumOut= size(out);
% filenameNumber= str2double(out(NumOut(2)))-1;

% filename = sprintf('%s_%d','filename.jpg',i);

% eval(['print -djpeg ' num2str(i) '.jpeg']);
saveas(gca, fullfile(path, strtok(J(i+1).name, '.')), 'jpg');
close;

% IAdivIB(i+1)= mean(IoutAct)/mean(IinAct);
thickness= (ActPos-MemPos)*2;

Thickness(1,i+1)= str2num(strtok(J(i+1).name, '_'));
Thickness(2,i+1)= thickness;
Thickness(3,i+1)= MaxAct;
Thickness(4,i+1)= MaxMem;
Thickness(5,i+1)= ActGOF.rsquare;
Thickness(6,i+1)= MemGOF.rsquare;
Thickness(7,i+1)= MaxMem / AverageBaselineMem;
Thickness(8,i+1)= MaxAct / AverageBaselineAct;
Thickness(9,i+1)= MaxPhall / AverageBaselinePhall;
Thickness(10,i+1)= MaxPhall;

if(i==SizeROIs)
    break
end
end

Thickness(:, ~any(Thickness,1) ) = []; %remove zero columns]
ThicknessFinal= transpose(Thickness); %%output in nanometers
ThicknessFinal= sortrows(ThicknessFinal,1);
ThicknessFinal(:,2)= ThicknessFinal(:,2) * 1E9;
xlswrite(fullfile(path, deepestFolder),ThicknessFinal);

figure;
hist(ThicknessFinal(:,2))
saveas(gca, fullfile(path, 'Thickness Histogram'), 'jpg');
close;

```

Matlab code #2:

```

clearvars -except All14 All21 ControlAll JaspAll

ActR2Thresh= .8;
MemR2Thresh= .8;
MemThreshVal= 4;
ActThreshVal= 4;
PhallThreshVal= 4;

Thresholded14(:,1)= transpose([All14([All14.ActR2]>ActR2Thresh &
[All14.MemR2]>MemR2Thresh & [All14.MemThresh]>MemThreshVal &
[All14.ActThresh]>ActThreshVal & [All14.PhallThresh]>PhallThreshVal).ROI]);
Thresholded14(:,2)= transpose([All14([All14.ActR2]>ActR2Thresh &
[All14.MemR2]>MemR2Thresh & [All14.MemThresh]>MemThreshVal &
[All14.ActThresh]>ActThreshVal &
[All14.PhallThresh]>PhallThreshVal).Thickness]);
Thresholded14(:,3)= transpose([All14([All14.ActR2]>ActR2Thresh &
[All14.MemR2]>MemR2Thresh & [All14.MemThresh]>MemThreshVal &
[All14.ActThresh]>ActThreshVal & [All14.PhallThresh]>PhallThreshVal).Phall]);
sz = 40;
Plot1=subplot(1,3,1,'FontSize','Arial','FontSize',20);
scatter(Thresholded14(:,2),Thresholded14(:,3),sz,[255,127,0]/255,'filled')
xlim([-200 500]); ylim([0 260]);
hold on;
xlabel('Thickness (um)','FontSize',20,'FontName','Arial')
ylabel('Phalloidin Intensity','FontSize',20,'FontName','Arial')

Thresholded21(:,1)= transpose([All21([All21.ActR2]>ActR2Thresh &
[All21.MemR2]>MemR2Thresh & [All21.MemThresh]>MemThreshVal &
[All21.ActThresh]>ActThreshVal & [All21.PhallThresh]>PhallThreshVal).ROI]);
Thresholded21(:,2)= transpose([All21([All21.ActR2]>ActR2Thresh &
[All21.MemR2]>MemR2Thresh & [All21.MemThresh]>MemThreshVal &
[All21.ActThresh]>ActThreshVal &
[All21.PhallThresh]>PhallThreshVal).Thickness]);
Thresholded21(:,3)= transpose([All21([All21.ActR2]>ActR2Thresh &
[All21.MemR2]>MemR2Thresh & [All21.MemThresh]>MemThreshVal &
[All21.ActThresh]>ActThreshVal & [All21.PhallThresh]>PhallThreshVal).Phall]);
scatter(Thresholded21(:,2),Thresholded21(:,3),sz,[55,126,184]/255,'filled')

meanPhallInt= [mean(Thresholded14(:,3)) mean(Thresholded21(:,3))];
stdPhallInt= [std(Thresholded14(:,3)) std(Thresholded21(:,3))];

meanThickness= [mean(Thresholded14(:,2)) mean(Thresholded21(:,2))];
stdThickness= [std(Thresholded14(:,2)) std(Thresholded21(:,2))];

PhallIntStatTest=ranksum(Thresholded21(:,3),Thresholded14(:,3))
ThicknessStatTest=ranksum(Thresholded21(:,2),Thresholded14(:,2))

Plot2=subplot(1,3,2,'FontSize',18,'FontName','Arial');

c = categorical({'St 14','St 21'});
Y= bar(meanPhallInt); set(Y,'FaceColor',[255,127,0]/255,'LineWidth',2);
hold on
O= bar(2,meanPhallInt(2)); set(O,'FaceColor',[55,126,184]/255,'LineWidth',2);

```

```

J=errorbar(c,meanPhallInt,[0 0],stdPhallInt, '.', 'LineWidth',2, 'Color', 'k');
e.Marker = '+'; e.MarkerSize = 10; e.Color = 'black'; e.CapSize = 5;
ylabel('Phalloidin Intensity', 'FontSize',20, 'FontName', 'Arial')
ylim([0 260]);
xlim([0 3]);
set(gca, 'XTickLabel', {'St 14', 'St 21'});

Plot3=subplot(1,3,3, 'FontSize',18, 'FontName', 'Arial', 'XTick', [1 2]);
Y2= bar(meanThickness); set(Y2, 'FaceColor', [255,127,0]/255, 'LineWidth',2);
hold on
O2= bar(2,meanThickness(2));
set(O2, 'FaceColor', [55,126,184]/255, 'LineWidth',2);
errorbar(c,meanThickness,[0 0],stdThickness, '.', 'LineWidth',2, 'Color', 'k');
% xlim([0 3]); ylim([0 600]);
ylabel('Thickness (um)', 'FontSize',20, 'FontName', 'Arial')
xlim([0 3]);
set(gca, 'XTickLabel', {'St 14', 'St 21'});

x0=10;
y0=10;
width=960;
height=320;
set(gcf, 'position', [x0,y0,width,height])

```

APPENDIX B

EPITHELIAL BLASTOPORE CLOSURE STRAIN MAPPING

The following describes my contribution to a publication co-first authored by Rafey Feroze and myself (Feroze et al. 2015) investigating the mechanics of blastopore closure in the *Xenopus* gastrula. In this manuscript, we describe the mechanics of blastopore closure at multiple scales and in different regions around the blastopore by characterizing large scale tissue deformations, cell level shape change and subcellular F-actin organization and by measuring tissue force production and structural stiffness of the blastopore during gastrulation. Prior to my involvement in the project, Rafey measured force of blastopore closure and mechanical resistance around the blastopore lip at various stages during gastrulation. Using a collection of time-lapse sequences collected by bright field stereoscopy by Mickey von Dassow, I analyzed the strain patterns of epithelial cells surrounding the blastopore during closure and identified stereotypic patterns.

B.1 RESULTS

B.1.1 Changing patterns of radial strain rate from mid- to late gastrulation

To understand the location and direction in which cellular forces are being generated, we analyzed mechanical strain rates in tissues surrounding the blastopore using digital image correlation on time-lapse sequences (Figure 37A, G, M; Supplementary Video S1). Strain rate is a scale- and geometry-free measure of tissue deformation over time that can be used to identify potential sources of force production or regions where mechanical properties change (see methods for a definition of strain (Blanchard et al. 2009; Davidson et al. 2009)). In contrast to simple deformation or trajectory maps, strain rate maps can indicate where tissues are expanding or contracting in radial and circumferential directions by comparing the displacement of multiple pixels together and calculating whether the distance between them is larger or smaller than in previous time frames. To calculate strain rate we estimate a displacement field or mathematical transform needed to align the two sequential images (Arganda-Carreras et al. 2006). The displacement field produced from this analysis consists of an array of two-dimensional (2D) vectors that bring each pixel in the first image into alignment with the second image. Displacement fields can be visualized by superimposing a subset of these vectors onto the original time lapse images (Figure 37B, H, N). Spatial gradients of these displacement vectors produce strain rate tensors which can be displayed as maps that reveal local variations in strain rate (Figure 37C-F, I-L, O-R). In principle, displacement and strain measured between images collected at different times represent the near-instantaneous velocity and the strain rate over a time interval. To recast the strain rates from image-coordinates onto embryonic axes we used a geometric transformation to calculate strains perpendicular to the blastopore (e.g. radial strain)

and strain parallel to the blastopore lip (e.g. circumferential strain) for each stage (see Methods). During early gastrulation, after dorsal lip formation, nearly all tissues surrounding the blastopore are expanding with the greatest expansive strain rate appearing dorsally (Figure 37E). As gastrulation progresses, that radial strain rate at the dorsal lip becomes contractile at stage 11 (Figure 37K) then expansive again by stage 12.5 (Figure 37Q). Figure 37 represents strain and displacement results of a single embryo to clearly illustrate our analyses. Median strains around the embryo at stages 10, 11 and 12.5 are consistent amongst 4 embryos and are summarized in Figure 38.

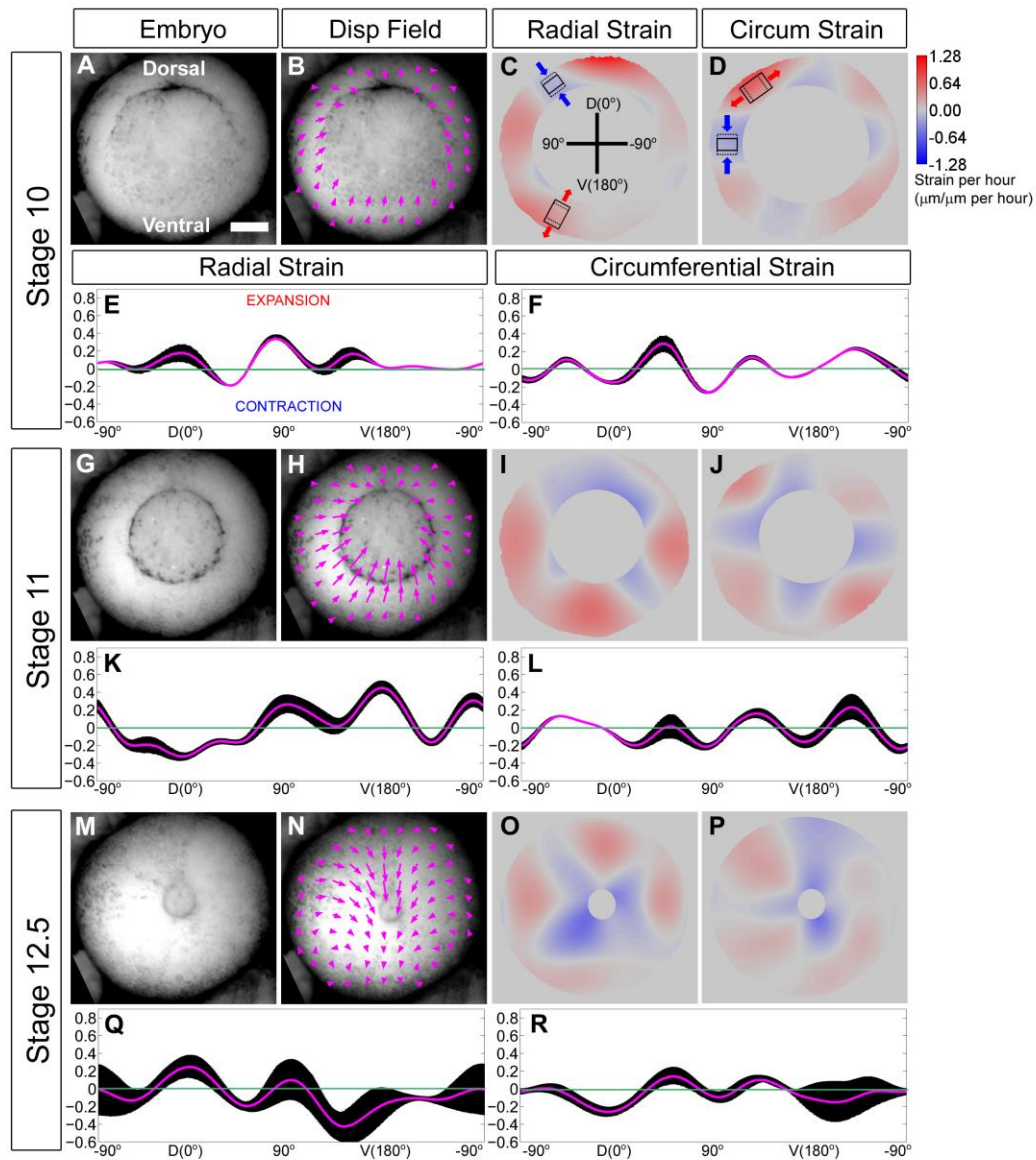


Figure 37. Strain Mapping of Blastopore Closure.

Strain and displacement analysis was done on stage 10 (A-F), stage 11 (G-L) and stage 12.5 (M-R) embryos. This figure shows analysis of a single embryo; however results from 4 other embryos are consistent and are summarized in Figure S1. Tissue net displacements (B,H,N) and strains were mapped using bUnwarpJ during BC (A,G,M). Radial and circumferential tissue strains are represented in polar (C,I,O & D,J,P) and cartesian (E,K,Q & F,L,R) coordinates during the beginning (A-F), middle (G-L) and end (M-R) of BC. The cartesian plots (E,K,Q & F,L,R) represent the median (magenta line) and 75 and 25% quartiles of pixel-by-pixel strain at specific angles around the blastopore, binned every 1 degree. Cartesian plots were calculated within the ‘flat region’ to avoid distorted strain

measurements from the embryo curvature. Displacement vectors are scaled 20x. Regions outside the embryo and within the yolk plug are manually shaded gray. Involution is occurring between -45 and 45 degrees at Stage 10; between -90 and 90 degrees at Stage 11; and all around the blastopore circumference at Stage 12.5. Scale bar in A represents 200 μ m.

During mid-gastrulation involution spreads from the dorso-anterior lip progressively reaching the ventral-posterior region of the blastopore by late-gastrulation and the surface contractility we observe correlates with these large scale involution movements. For instance, there is a high degree of radial contraction in posterior-ventral regions of the embryo as prospective posterior mesoderm and endoderm initiate involution (Figure 37Q).

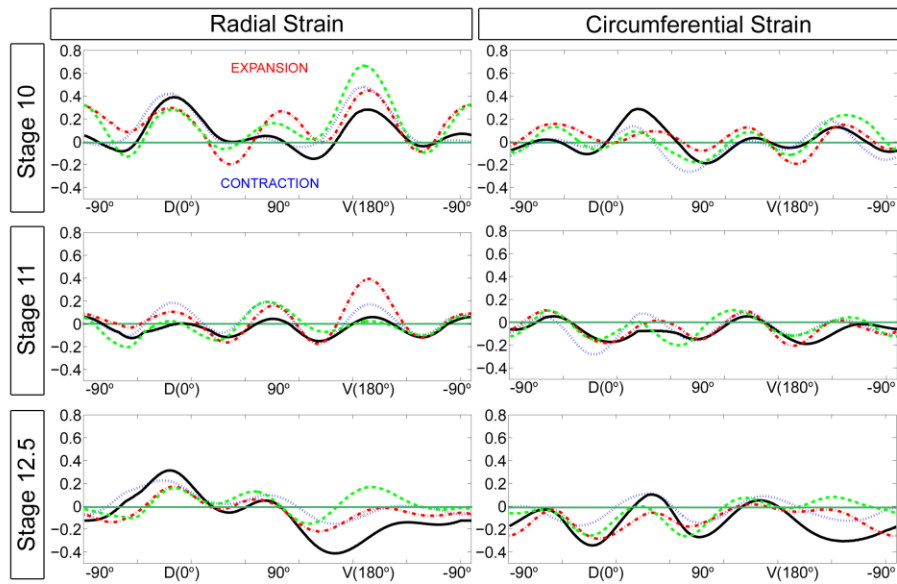


Figure 38. Mean strain values in 4 embryos over blastopore closure.

Strain analysis done in 4 embryos (black, blue, red, and green plots) at stages 10, 11 and 12.5. Y-axis represents strains per hour (μ m/ μ m per hour). Positive strains represent expansion and negative strains represent contraction. The horizontal green line indicates zero strain in all plots. Radial and circumferential strain rates were obtained by methods described in the *Strain Mapping* methods section. All 4 embryos were cultured at 26 deg C.

B.1.2 Strain patterns reflective of known tissue movements

Our multilevel description of blastopore closure reports complex patterns of strain rate (Figure 39), the integrative force of closure and structural stiffness of the blastopore, the irregular shapes of epithelial cells and the presence of aligned F-actin at their apical surface and suggests novel roles for the epithelial cells during amphibian gastrulation. At the level of the tissue we see complex patterns of contraction and expansion. At early stages we observe large regions surrounding the blastopore that exhibit strain rate patterns indicative of epiboly (e.g. radial and circumferential expansion). At late stages strain rates appear to reflect underlying processes of convergence and extension (e.g. radial expansion and circumferential contraction) and convergent thickening (e.g. radial and circumferential contraction). Interestingly, epithelial cells do not exhibit common tiling patterns seen in passive arrays of cells but instead exhibit complex, often torturous shapes, with strongly aligned apical arrays of F-actin. We propose these arrays develop in response to complex patterns of strain. Compressive strains in both direction may cause apical cell junctions to buckle. Anisotropic strain patterns may initiate the formation of aligned F-actin as is found at the basal surface of cells exposed to shear flows. These observations suggest epithelial cells are adapting to strain in the epithelium in unexpected ways and may either contribute to force production of blastopore closure or serve to guide movements of blastopore closure or later morphogenetic movements by offering anisotropic resistance.

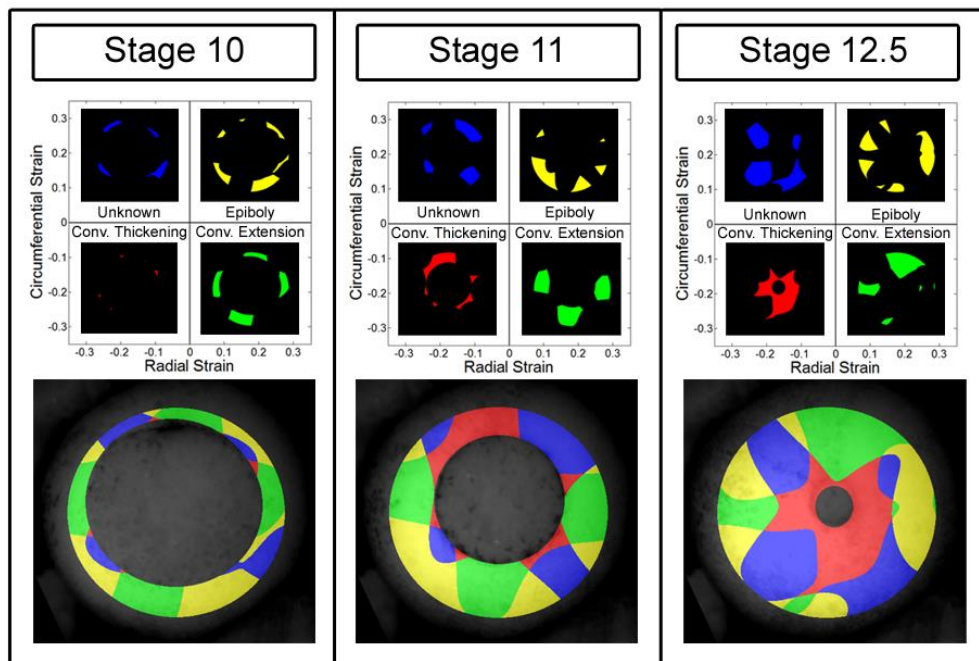


Figure 39. Strain patterns around the blastopore during gastrulation.

Regions of positive radial strain and positive circumferential strain (+R, +C; yellow) is suggestive of epiboly-like tissue movements. Regions with positive radial and negative circumferential strains suggest converging and extending tissues and regions with negative radial and negative circumferential may indicate tissues undergoing convergent thickening.

B.2 METHODS

B.2.1 Strain Rate Mapping

To characterize the strain rate in the embryo, image sequences were collected at 26° C and analyzed using an open source image analysis software (ImageJ; (Rueden and Eliceiri, 2007); available at <http://rsb.info.nih.gov/ij>; developed by Wayne Rasband, National Institutes of

Health, Bethesda, MD) and a custom plugin (bUnwarpJ)(Arganda-Carreras et al., 2006). This plugin allows us to calculate strain by using image registration of two images based on elastic deformations represented by B-splines. Custom macros were created to sequentially obtain strain maps throughout an image sequence. By tailoring our time interval for image registration we are able to uncover strain rates over short (< 2 minutes) and long time scales (> 30 minutes) throughout development. A colormap for the strain rate at each pixel was calculated and plotted, depicting blue as contraction and red as expansion. A custom ImageJ plugin was used to display the displacement as vectors superimposed on the original data. Radial (ϵ_r) and circumferential (ϵ_θ) strain rates were calculated by transforming the strain rate tensor, $\epsilon = [\epsilon_{xx} \ \epsilon_{xy} \ \epsilon_{yx} \ \epsilon_{yy}]$, to polar coordinates (Korukonda and Doyley, 2012). For each pixel,

$$\epsilon_r = \frac{1}{x^2 + y^2} [x^2 \epsilon_{xx} + xy(\epsilon_{xy} + \epsilon_{yx}) + y^2 \epsilon_{yy}]$$

$$\epsilon_\theta = \frac{1}{x^2 + y^2} [y^2 \epsilon_{xx} - xy(\epsilon_{xy} + \epsilon_{yx}) + x^2 \epsilon_{yy}]$$

where x = horizontal distance from blastopore centroid and y = vertical distance from blastopore centroid. Radial and circumferential sweep boxplots were calculated for regions within 5 to 10 cell diameters of the blastopore to avoid potential distortion from surface curvature (MATLAB, R2013; Mathworks Inc., Natick, MA).

APPENDIX C

NUCLEI TRACKING IN SPREADING ANIMAL CAP TISSUES

The following describes my contribution to a publication first authored by Jiho Song (Song et al. 2015) investigating how topological cues influence animal cap spreading. In this manuscript, I provided nuclear tracking of deep animal cap mesenchymal cells to obtain kinematic measurements of migration through different microenvironments.

C.1 INTRODUCTION

Single cell motility has been extensively studied with 3D topologies such as using microwell, micro-grooves and ridges, and micropillars (Mohr et al. 2006; Teixeira et al. 2003; Ghibaudo et al. 2011; Kim et al. 2014); however, little is known about collective cell migration within topologically controlled surfaces and especially in multi-cellular integrated systems during development. In this study, microfabricated micropost arrays (MPAs) provide a tool for studying biological responses to complex surfaces and topologies (Engler et al. 2006; Rossier et al. 2010; Dembo and Wang 1999; Burton et al. 1999).

C.2 RESULTS

C.2.1 Surface topographical cues influence individual cell movements within the tissue

To understand tissue spreading at an individual cell level in composite animal cap tissue explants, we expressed H2B-mRFP and tracked mRFP expressing mesenchymal nuclei in tissues spreading into 10 mm, 20 mm, and 40 mm MPAs (Figure 40A). To understand the difference between single cell movements that were random and those directed toward the edge of the explant, we calculated the angular deviation of the nuclei trajectory movements. The angular deviation ranged from 0 to 81°, and we found the angular deviation of cells in the center of explant was significantly greater than cells on the edge (Figure 40B,C; $p < 0.001$; One-way ANOVA). We found no significant differences in the angular deviation of either edge or center cells between MPAs of differing spacing or flat PDMS (Figure 40D).

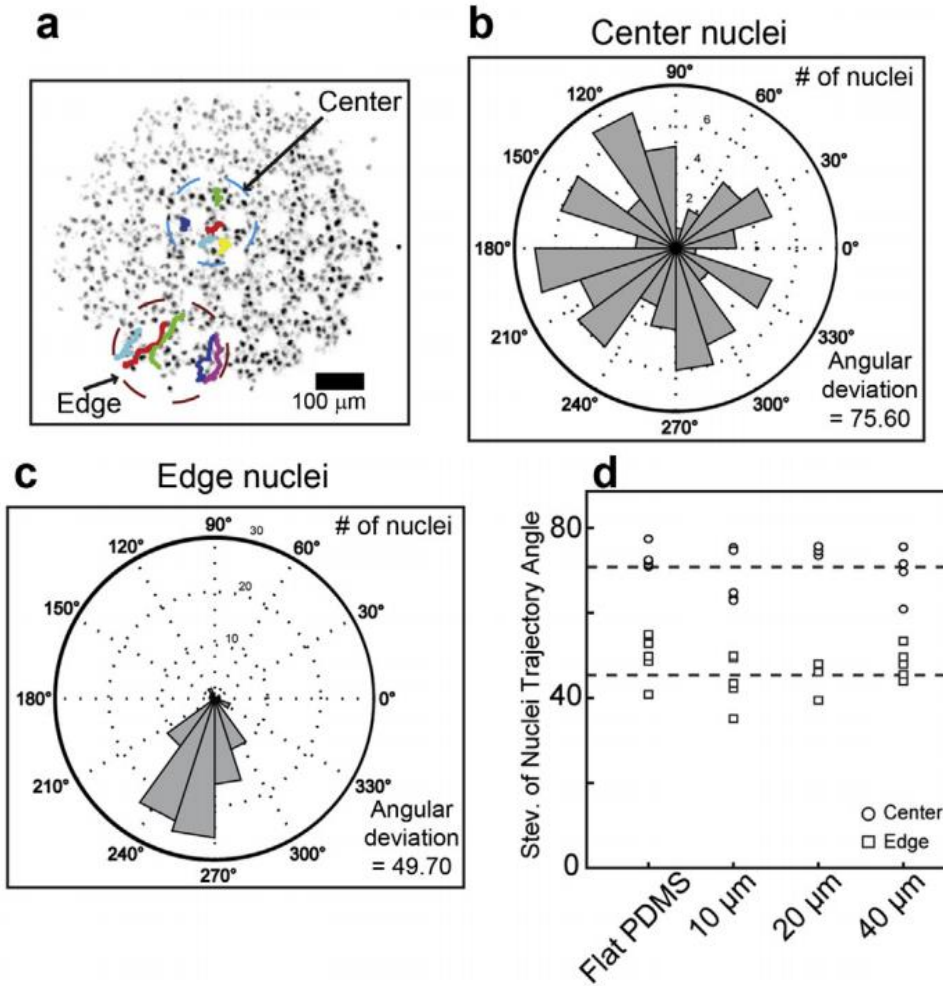


Figure 40. Cell motility within animal cap tissue spreading on 3D surfaces.

(a) Representative max z-projected confocal image of an AC with fluorescent nuclei (H2B-GFP) during spreading with example nuclei trajectories in center and edge nuclei. (b, c) Rose plot distribution of representative nuclei trajectory angles (initial position to final position) in center (b), and edge (c), nuclei of an AC spreading into a 40 mm MPA. One 200 by 200 μm region of edge and center nuclei was analyzed. The angular deviation is the spread of the nuclei trajectory angle data. Higher deviation is observed in center nuclei compared with edge nuclei (75.6 vs. 49.7). (d) Angular deviation of nuclei trajectories on flat PDMS and on MPAs surfaces (mean angular standard deviation in center and edge nuclei are 46.8 ± 5.18 and 71.32 ± 4.96 , respectively).

C.3 METHODS

C.3.1 Microscopy and imaging processing

We acquired time-lapsed images tissues spreading over micropost arrays surfaces on an inverted compound microscope (Zeiss Axiovert S100) XY-stage at the focus of a stereoscope mounted with a CCD camera (Scion Imaging Corp). Multiple positions were recorded from the same chamber using an XY motorized stage (Marzhauser and Ludl) controlled by a computer image acquisition system (ImageJ and Micromanager (Edelstein et al. 2010)). Time-lapse sequences were collected for up to 20 hours. The position of the leading edge was segmented using edge detection (MatLab, The Mathworks, Cambridge, MA). Segmentation of subsequent images allowed us to automatically track tissue areas and nuclei over time to track tissue spreading and cell nuclei movement.

Laser scanning microscopy was used to acquire high-resolution confocal image stacks of tissues expressing fluorescently labeled nuclei. Confocal time-lapse sequences were collected using a confocal laser scan head (SP5 Leica Microsystems) mounted on an inverted compound microscope (DMI6000, Leica Microsystems) using acquisition software (LASAF, Leica Microsystems). Samples were illuminated using a 488nm Argon laser. For time-lapse sequences of animal cap spreading, images were acquired with a 0.7 NA 20X objective every 3-4 minutes with an acquisition rate of 400Hz, resolution of 512 x 512 pixels and a pinhole setting of 1.2 A.U. For fixed samples, high-resolution images were acquired with a 0.95 NA 25X water-immersion plan apochromat objective.

Nuclei detection and tracking were carried out using the MOSAIC Particle 2D/3D plugin in ImageJ (available at <http://rsb.info.nih.gov/ij>; developed by Wayne Rasband, National Institutes of Health, Bethesda, MD). Ideal parameters for nuclei detection were manually set for each experiment (typically 6 pixels, 1.0 and 4% for radius, cutoff, and percentile, respectively). The link range for particle linking was set to 2 frames and the link displacement was set to 10 pixels. Nuclei trajectories were analyzed by custom scripts to calculate velocity, persistence, and directedness (MATLAB). Nuclei trajectories were considered for analysis only if they appeared in a minimum of 10 frames.

C.3.2 Cell Tracking Parameter Macro

The following macro was written to analyze the raw nuclear tracking data outputted from Moasic>Particle 2D/3D Tracker (built in Fiji). Nuclear velocity, persistence, directedness and direction were calculated based on trajectories.

```
% Particle Tracking Macro
% Joe Shawky
% Save previously obtained Data as Excel Data sheet (Mosaic-->Particle
Tracker 2D/3D)
% Excel Data sheet has 12 columns and however many trajectories- rows
% Column# Traj# Frame x y z m0 m1 m2 m3 m4 NPscore

% look up Vittorino and & Tobias Meyer(stanford)

%Direction of motion should be downward (-y)

clear
clc

%Asks user to find Excel data file
A=xlsread(uigetfile('*.xls','Select the Excel Particle Tracking Data file'));

prompt= ('Drift Distance','Drift Angle','How many frames must the cell be
in?','What is the Time Interval?','How many microns per pixel?','Angle
Corrector (for directedness)');
def=('0','0','10','180','0.84034','0');
Inputs = inputdlg(prompt, 'Input Parameters', 1,def);
```

```

m=size(A,1); %number of rows in whole data range

%%%%%%%%%%%%%%%%%%%%%%%%%%%%%%%%%%%%%%%%%%%%%%%%%%%%%%%%%%%%%%%%%%%%%%%%
Drift_Correction_Dist=str2double(Inputs(1));
Drift_Correction_Angle=str2double(Inputs(2));

Drift_X=Drift_Correction_Dist*cosd(Drift_Correction_Angle);
Drift_Y=Drift_Correction_Dist*sind(Drift_Correction_Angle);
time_points=81;
x_drift_pf=Drift_X/time_points;
y_drift_pf=Drift_Y/time_points;

%Drift Corrector
for a=1:1:m-1
    A(a,5)=A(a,5) - x_drift_pf*A(a,3);
    A(a,4)=A(a,4) - y_drift_pf*A(a,3);
end
%%%%%%%%%%%%%%%%%%%%%%%%%%%%%%%%%%%%%%%%%%%%%%%%%%%%%%%%%%%%%%%%%%%%%%%%

% y0 x0 z0 x y z Traj# FirstTimeFrame LastTimeFrame
CellPos=zeros([1400 9]);

% yDisp xDisp zDisp NetXYDisp XYDir XYZDisp XYrate(in um/hour)
Disps=zeros([1400 7]);

timeInterval= str2double(Inputs(4)); %Time interval between each frame in
seconds
pixelScale= str2double(Inputs(5)); % How many microns per pixel?

% TotalXY PersIndex PersScore(0-low, 4-high) Directedness
PathDis=zeros([1400 4]);

%only keeps trajectories that are in this many frames
traj= str2double(Inputs(3));

%Cell Time X Y PersColor
ImageJOutput=zeros([15000 4]);

NumCell=0;
trajCount=0;
p=0;

for i=1:1:m-1
    trajCount=trajCount+1;
    if A(i+1,2) ~= A(i,2)
        if trajCount>=traj
            NumCell=NumCell+1;
            CellPos(NumCell,1)= A(i-trajCount+1,4);
            CellPos(NumCell,2)= A(i-trajCount+1,5);
            CellPos(NumCell,3)= A(i-trajCount+1,6);
            CellPos(NumCell,4)= A(i,4);
        end
    end
end

```

```

CellPos (NumCell,5)= A(i,5);
CellPos (NumCell,6)= A(i,6);
CellPos (NumCell,7)= A(i,2);
CellPos (NumCell,8)= A(i-trajCount+1,3);
CellPos (NumCell,9)= A(i,3);
Disps (NumCell,1)= CellPos (NumCell,4)-CellPos (NumCell,1);
Disps (NumCell,2)= CellPos (NumCell,5)-CellPos (NumCell,2);
Disps (NumCell,3)= CellPos (NumCell,6)-CellPos (NumCell,3);
Disps (NumCell,4)=sqrt (Disps (NumCell,1)^2+Disps (NumCell,2)^2);

Disps (NumCell,5)=(atan2 (-Disps (NumCell,1), Disps (NumCell,2)));

Disps (NumCell,6)=sqrt (Disps (NumCell,1)^2+Disps (NumCell,2)^2);

for k=1:1:trajCount-1
    PathDis (NumCell,1)= PathDis (NumCell) + sqrt((A(i-
trajCount+k+1,4)-A(i-trajCount+k,4))^2 + (A(i-trajCount+k+1,5) - A(i-
trajCount+k,5))^2);
    p=p+1;
    ImageJOutput (p,1)= NumCell;
    ImageJOutput (p,2)= A(i-trajCount+k,3);
    ImageJOutput (p,3)= A(i-trajCount+k,5);
    ImageJOutput (p,4)= A(i-trajCount+k,4);
end
PathDis (NumCell,2)= Disps (NumCell,4)/PathDis (NumCell,1);
%persistence index

Disps (NumCell,7)=
(PathDis (NumCell,1)*pixelScale)/(trajCount*timeInterval/3600);
%Disps (NumCell,7)=
(Disps (NumCell,4)*pixelScale)/(trajCount*timeInterval/3600);
end
trajCount=0;
end
end

% puts a rank on Persistence
for i=1:NumCell
    if PathDis(i,2) <= .2
        PathDis(i,3)=0;
    elseif PathDis(i,2) <= .4 && PathDis(i,2) > .2
        PathDis(i,3)=1;
    elseif PathDis(i,2) <= .6 && PathDis(i,2) > .4
        PathDis(i,3)=2;
    elseif PathDis(i,2) <= .8 && PathDis(i,2) > .6
        PathDis(i,3)=3;
    elseif PathDis(i,2) <= 1 && PathDis(i,2) > .8
        PathDis(i,3)=4;
    end
end

%Puts Persistence rank in ImageJ Output file
j=1;
ImageJfilesize= 0;

```

```

for i=1:9999
    if ImageJOutput(i+1,1) == ImageJOutput(i,1)
        ImageJOutput(i,5)= PathDis(j,3);
    else
        ImageJOutput(i,5)= PathDis(j,3);
        j=j+1;
    end
    if ImageJOutput(i,1)==0
        break;
    end
end

dlmwrite('ImageJfromMatlab',ImageJOutput)

%Plots all trajectories on a circular plot emanating from the origin

%compass(Disps(1:NumCell,2),-Disps(1:NumCell,1))

% set(gcf,'FontSize',25); grid off;
%
set(gcf,'PaperPositionMode','Manual','PaperOrientation','Landscape','PaperPosition',[0 0 11 8.5]);
% set(gcf,'Position',[10 50 1300 700],'Color','w');
% saveas(gcf, 'C:\Users\Joe
Shawky\Dropbox\Journal_Figures\40umCenterComp','pdf')

J= [transpose(1:NumCell), PathDis(1:NumCell,1), Disps(1:NumCell,4),
Disps(1:NumCell,7), Disps(1:NumCell,5), PathDis(1:NumCell,2)];
disp(' cell# TotDisplacement NetDisplacement Speed(um/hr) Direction
PersistenceIndex ')
disp(' ')
%disp(J)

meanPI= mean(PathDis(1:NumCell,2))
stdevPI= std(PathDis(1:NumCell,2))
meanV= mean(Disps(1:NumCell,7))
stdevV= std(Disps(1:NumCell,7))

% figure;
% hist(PathDis(1:NumCell,2))
% ylabel('count')
% xlabel('Persistence Index')
%
% figure;
% hist(Disps(1:NumCell,7))
% ylabel('count')
% xlabel('Cell Velocity (um/hr)')

% figure;
% h=rose2(Disps(1:NumCell,5));

```

```

%Adjust angles of motion for new scale (new 0 = 270 degrees, new 180= 90
degrees)

AngCorrector= degtorad(str2double(Inputs(6)));

for i=1:NumCell
    if (Disps(i,5)>0 && AngCorrector>0) || (Disps(i,5)<0 && AngCorrector<0)
        Disps(i,5)=Disps(i,5)-AngCorrector;
    else
        Disps(i,5)=Disps(i,5)+AngCorrector;
    end
    PathDis(i,4)= cos(Disps(i,5));%Calc a 'directedness'
end

% for i=1:NumCell
%     if Disps(i,5)<1.57
%         Disps(i,5)=Disps(i,5)+pi/2;
%     else
%         Disps(i,5)=Disps(i,5)-3*pi/2;
%     end
%     PathDis(i,4)= cos(Disps(i,5));%Calc a 'directedness'
% end

% figure;
% hist(Disps(1:NumCell,5))
% ylabel('count')
% xlabel('Direction (rad)')
% axis([-pi pi 0 Inf])

% %spectrum for total displacement from 2-16
% nc = 17;
% offset = 1;
% c = PathDis(1:NumCell,1) - min(PathDis(1:NumCell,1));
% c = round((nc-1-2*offset)*c/max(c)+1+offset);

% %spectrum for net displacement from 2-16
% nc = 17;
% offset = 1;
% c = Disps(1:NumCell,4) - min(Disps(1:NumCell,4));
% c = round((nc-1-2*offset)*c/max(c)+1+offset);
%
%
% figure
% scatter(Disps(1:NumCell,7),PathDis(1:NumCell,2),80,c)
% xlabel('Speed (um/hr)')
% ylabel('Persistence Index')
%

```

```

% %spectrum for persistence index from 2-16
% nd = 17;
% offset = 1;
% d = PathDis(1:NumCell,2) - min(PathDis(1:NumCell,2));
% d = round((nc-1-2*offset)*d/max(d)+1+offset);

% %%%SUPERIMPOSE TRACKS ONTO TIF IMAGE
%
% FileTif=uigetfile('*.tif','Select the Image file to superimpose nuclei
on');
% InfoImage=imfinfo(FileTif);
% mImage=InfoImage(1).Width;
% nImage=InfoImage(1).Height;
% NumberImages=length(InfoImage);
% FinalImage=zeros(nImage,mImage,NumberImages,'uint8');
% RGBImage=zeros(nImage,mImage,NumberImages*3,'uint8');
%
% for i=1:NumberImages
%     FinalImage(:, :, i)=imread(FileTif,'Index',i,'Info',InfoImage); %grayscale
tif
%     RGBImage(:, :, i*2+(i-2):i*2+(i))=ind2rgb8(FinalImage(:, :, i),gray); %RGB
tif
% end
%
%
% blue = uint8([0 255 255]); % [R G B];
% green = uint8([0 247 0]); % [R G B];
% yellow = uint8([236 252 14]); % [R G B];
% orange = uint8([255 128 0]); % [R G B];
% red = uint8([255 0 0]); % [R G B];
%
%
% shapeInserterBlue =
vision.ShapeInserter('Shape','Circles','BorderColor','Custom','CustomBorderCo
lor',blue,'Fill',true,'FillColor','Custom','CustomFillColor',blue);
% shapeInserterGreen =
vision.ShapeInserter('Shape','Circles','BorderColor','Custom','CustomBorderCo
lor',green,'Fill',true,'FillColor','Custom','CustomFillColor',blue);
% shapeInserterYellow =
vision.ShapeInserter('Shape','Circles','BorderColor','Custom','CustomBorderCo
lor',yellow,'Fill',true,'FillColor','Custom','CustomFillColor',blue);
% shapeInserterOrange =
vision.ShapeInserter('Shape','Circles','BorderColor','Custom','CustomBorderCo
lor',orange,'Fill',true,'FillColor','Custom','CustomFillColor',blue);
% shapeInserterRed =
vision.ShapeInserter('Shape','Circles','BorderColor','Custom','CustomBorderCo
lor',red,'Fill',true,'FillColor','Custom','CustomFillColor',blue);
%
%
% %J=zeros(nImage,mImage,NumberImages,'uint8');
%
% %R= uint8([50,50,3;60,60,3]);
% PartSize=2; %size of circle drawing
%
% for i=0:4

```

```

% inThisFrame=0;
%   for j=1:NumCell
%       if CellPos(j,8) == 0 && PathDis(j,3)=0;
%           inThisFrame= inThisFrame+1;
%       end
%   end
%
%   if PathDis(j,3)=0
%       Rblue= uint8([CellPos(1:inThisFrame,2),CellPos(1:inThisFrame,1),
repmat(PartSize, inThisFrame,1 )]);
%       Jblue = step(shapeInserterBlue,RGBImage(:, :, 1:3),Rblue);
%   elseif PathDis(j,3)=1
%       Rblue= uint8([CellPos(1:inThisFrame,2),CellPos(1:inThisFrame,1),
repmat(PartSize, inThisFrame,1 )]);
%       Jblue = step(shapeInserterBlue,RGBImage(:, :, 1:3),Rblue);
%   end
%
%
%   imshow(J)

```

APPENDIX D

TISSUE STRAIN ENERGY

Since embryonic tissues are viscoelastic, the amount of force cells produce includes both the force needed to achieve morphogenetic movement and the force lost to viscous dissipation into the tissue. Dorsal isolates actively generate forces during convergent extension in which they elongate antero-posteriorly (AP) and converge in the orthogonal mediolateral (ML) direction. In this study, we sought to quantify energy storage and recovery within embryonic tissues. To test strain-energy storage over long timescales, we stalled the ability of these tissues to elongate by confining them in the AP direction. These tissues continue to generate stresses to elongate (Zhou et al. 2015) however are unable to deform. After constraint removal, we then measured how much elongation strain is recovered compared to unconfined control tissues. Tissue strain is quantified through time-lapse imaging of tissues.

Tissues were microsurgically isolated at stage 13, allowed to heal for 30 minutes and imaged for four hours under different conditions; freely extending, constrained, and constrained for 2.5 hours then released (Figure 41). Explants were constrained using two plastic shims on the anterior and posterior edges to restrict extension. We note two interesting results from this

experiment: 1. Convergence continues at reduced levels even when extension is constrained, and
2. Explants can store elastic strain energy and release it after constraints are removed.

The continued convergence of dorsal isolates after extension is inhibited is interesting because the question arises: where does the tissue go? In these experiments (Figure 41; Group 2) the explant is not only constrained anterior and posteriorly but also dorso-ventrally to restrict curling up. Tissues within the explant may be compacting into denser structures.

Secondarily, measuring strain energy storage within embryos will aid in understanding the interplay of force generation and material properties that drives embryonic morphogenesis and give further insights into how embryonic tissues adapt to their mechanical environment. Identifying the molecular- and cell-level features of tissues that permit elastic strain storage at long time scales is an interesting problem since the cytoskeleton, specifically actomyosin networks are known to turn over on the order of seconds to minutes. Beyond being an inherent property of tissues, strain energy storage may serve biological functions helping with shape recovery or movement efficiency.

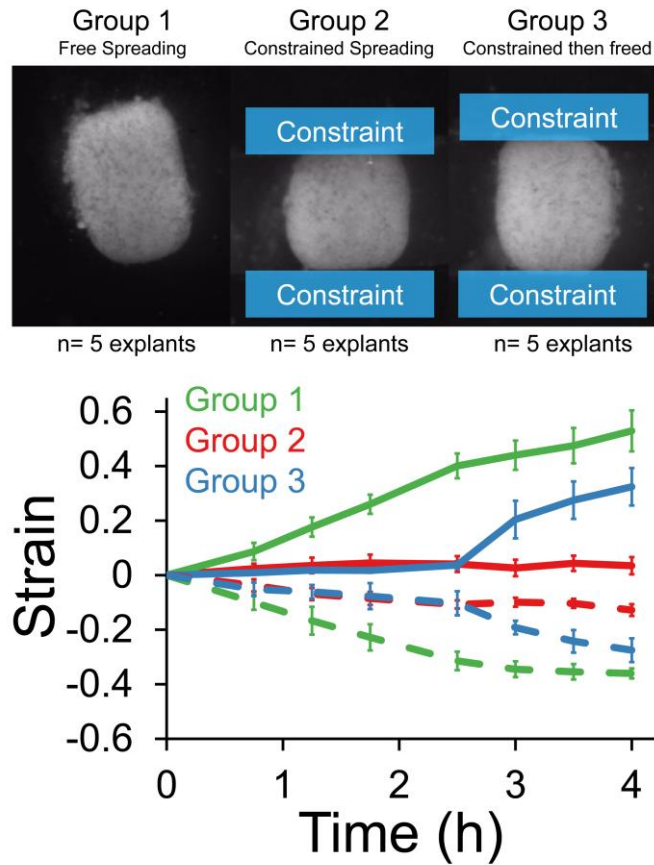


Figure 41. Recoil of dorsal isolates after release from constraint.

Time-lapse sequences of dorsal isolates under 3 different constraint conditions were collected. Solid lines on plot indicate extension while dashed lines indicate convergence. In group 3, the tissue constraint was removed at 2.5 hours. Note the recoil strain in group 3 after constraint removal.

BIBLIOGRAPHY

- Adams, D. S., R. Keller, and M. A. Koehl** (1990). The mechanics of notochord elongation, straightening and stiffening in the embryo of *Xenopus laevis*. *Development* **110**(1): 115-30.
- Aegerter-Wilmsen, T., A. C. Smith, A. J. Christen, C. M. Aegerter, E. Hafen, and K. Basler** (2010). Exploring the effects of mechanical feedback on epithelial topology. *Development* **137**: 499-506.
- Alberts, Bruce**. 2015. *Molecular biology of the cell* (Garland Science, Taylor and Francis Group: New York, NY).
- Aman, A., and T. Piotrowski** (2010). Cell migration during morphogenesis. *Dev Biol* **341**: 20-33.
- Arganda-Carreras, I., C. O. S. Sorzano, R. Marabini, J.M. Carazo, C. O. de Solorzano, and J. Kybic** (2006). Consistent and elastic registration of histological sections using vector-spline regularization. *CVAMIA: Computer Vision Approaches to Medical Image Analysis*: **4241**: 85-95.
- Barthes, J., H. Ozelik, M. Hindie, A. Ndreu-Halili, A. Hasan, and N. E. Vrana** (2014). Cell microenvironment engineering and monitoring for tissue engineering and regenerative medicine: the recent advances. *Biomed Res Int* **2014**: 921905.
- Bartles, J. R.** (2000). Parallel actin bundles and their multiple actin-bundling proteins. *Curr Opin Cell Biol* **12**: 72-8.
- Bayas, M. V., A. Leung, E. Evans, and D. Leckband** (2006). Lifetime measurements reveal kinetic differences between homophilic cadherin bonds. *Biophys J* **90**: 1385-95.
- Beaune, Grégory, Tomita Vasilica Stirbat, Nada Khalifat, Olivier Cochet-Escartin, Simon Garcia, Vasily Valériévitch Gurchenkov, Michael P Murrell, Sylvie Dufour, Damien Cuvelier, and Françoise Brochard-Wyart** (2014). How cells flow in the spreading of cellular aggregates. *Proceedings of the National Academy of Sciences* **111**: 8055-60.

- Belousov, L. V., and V. I. Grabovsky** (2007). Information about a form (on the dynamic laws of morphogenesis). *Biosystems* **87**: 204-14.
- Bhadriraju, K., M. Yang, S. Alom Ruiz, D. Pirone, J. Tan, and C. S. Chen** (2007). Activation of ROCK by RhoA is regulated by cell adhesion, shape, and cytoskeletal tension. *Exp Cell Res* **313**: 3616-23.
- Blanchard, G. B., A. J. Kabla, N. L. Schultz, L. C. Butler, B. Sanson, N. Gorfinkiel, L. Mahadevan, and R. J. Adams** (2009). Tissue tectonics: morphogenetic strain rates, cell shape change and intercalation. *Nat Methods* **6**: 458-64.
- Borghi, Nicolas, Maria Sorokina, Olga G Shcherbakova, William I Weis, Beth L Pruitt, W James Nelson, and Alexander R Dunn** (2012). E-cadherin is under constitutive actomyosin-generated tension that is increased at cell–cell contacts upon externally applied stretch. *Proceedings of the National Academy of Sciences* **109**: 12568-73.
- Brodland, G. W.** (2002). The Differential Interfacial Tension Hypothesis (DITH): a comprehensive theory for the self-rearrangement of embryonic cells and tissues. *J Biomech Eng* **124**: 188-97.
- Burton, K., J.H. Park, and D.L. Taylor** (1999). Keratocytes generate traction forces in two phases. *Mol. Biol. of the Cell* **10**: 3745-69.
- Chaigne, Agathe, Clément Campillo, Nir S. Gov, Raphaël Voituriez, Jessica Azoury, Claudia Umaña-Diaz, Maria Almonacid, Isabelle Queguiner, Pierre Nassoy, Cécile Sykes, Marie-Hélène Verlhac, and Marie-Emilie Terret** (2013). A soft cortex is essential for asymmetric spindle positioning in mouse oocytes. *Nat Cell Biol* **15**: 958-66.
- Chien, Y. H., N. Jiang, F. Li, F. Zhang, C. Zhu, and D. Leckband** (2008). Two stage cadherin kinetics require multiple extracellular domains but not the cytoplasmic region. *J Biol Chem* **283**: 1848-56.
- Choi, Y. S., R. Sehgal, P. McCrea, and B. Gumbiner** (1990). A cadherin-like protein in eggs and cleaving embryos of *Xenopus laevis* is expressed in oocytes in response to progesterone. *J Cell Biol* **110**: 1575-82.
- Chugh, Priyamvada, Andrew G. Clark, Matthew B. Smith, Davide A. D. Cassani, Kai Dierkes, Anan Ragab, Philippe P. Roux, Guillaume Charras, Guillaume Salbreux, and Ewa K. Paluch** (2017). Actin cortex architecture regulates cell surface tension. *Nat Cell Biol* **19**: 689-97.
- Churchman, L. S., and J. A. Spudich** (2012). Single-molecule high-resolution colocalization of single probes. *Cold Spring Harb Protoc* **2012**: 242-5.

- Claessens, M. M., M. Bathe, E. Frey, and A. R. Bausch** (2006). Actin-binding proteins sensitively mediate F-actin bundle stiffness. *Nat Mater* **5**: 748-53.
- Clark, A. G., K. Dierkes, and E. K. Paluch** (2013). Monitoring actin cortex thickness in live cells. *Biophys J* **105**: 570-80.
- Conway, Daniel E, Mark T Breckenridge, Elizabeth Hinde, Enrico Gratton, Christopher S Chen, and Martin A Schwartz** (2013). Fluid shear stress on endothelial cells modulates mechanical tension across VE-cadherin and PECAM-1. *Current Biology* **23**: 1024-30.
- Cunningham, C. C., J. B. Gorlin, D. J. Kwiatkowski, J. H. Hartwig, P. A. Janmey, H. R. Byers, and T. P. Stossel** (1992). Actin-binding protein requirement for cortical stability and efficient locomotion. *Science* **255**: 325-7.
- Dali, L., J. Gustin, K. Perry, and C. R. Domingo** (2002). Signals that instruct somite and myotome formation persist in *Xenopus laevis* early tailbud stage embryos. *Cells Tissues Organs* **172**: 1-12.
- Davidson, L. A.** (2008). Integrating morphogenesis with underlying mechanics and cell biology. *Curr Top Dev Biol* **81**: 113-33.
- Davidson, L. A., B. D. Dzamba, R. Keller, and D. W. Desimone** (2008). Live imaging of cell protrusive activity, and extracellular matrix assembly and remodeling during morphogenesis in the frog, *Xenopus laevis*. *Dev Dyn* **237**: 2684-92.
- Davidson, L. A., B. G. Hoffstrom, R. Keller, and D. W. DeSimone** (2002). Mesendoderm extension and mantle closure in *Xenopus laevis* gastrulation: combined roles for integrin alpha5beta1, fibronectin, and tissue geometry. *Dev Biol* **242**: 109-29.
- Davidson, L. A., R. Keller, and D. W. Desimone** (2004). Assembly and remodeling of the fibrillar fibronectin extracellular matrix during gastrulation and neurulation in *Xenopus laevis*. *Dev Dyn* **231**: 888-95.
- Davidson, L. A., M. A. Koehl, R. Keller, and G. F. Oster** (1995). How do sea urchins invaginate? Using biomechanics to distinguish between mechanisms of primary invagination. *Development* **121**: 2005-18.
- Davidson, L. A., G. F. Oster, R. E. Keller, and M. A. Koehl** (1999). Measurements of mechanical properties of the blastula wall reveal which hypothesized mechanisms of primary invagination are physically plausible in the sea urchin *Strongylocentrotus purpuratus*. *Dev Biol* **209**: 221-38.

- Davidson, L., and R. Keller** (2007). Measuring mechanical properties of embryos and embryonic tissues. *Methods Cell Biol* **83**: 425-39.
- Davidson, L., M. von Dassow, and J. Zhou** (2009). Multi-scale mechanics from molecules to morphogenesis. *Int J Biochem Cell Biol* **41**: 2147-62.
- Davidson, Lance A** (2011). 7 Embryo Mechanics: Balancing Force Production with Elastic Resistance During Morphogenesis. *Current topics in developmental biology* **95**: 215.
- Dembo, M., and Y.L. Wang** (1999). Stresses at the cell-to-substrate interface during locomotion of fibroblasts. *Biophys. J.* **76**: 2307-16.
- Douezan, S., K. Guevorkian, R. Naouar, S. Dufour, D. Cuvelier, and F. Brochard-Wyart** (2011). Spreading dynamics and wetting transition of cellular aggregates. *Proc Natl Acad Sci U S A* **108**: 7315-20.
- Dray, N., A. Lawton, A. Nandi, D. Julich, T. Emonet, and S. A. Holley** (2013). Cell-fibronectin interactions propel vertebrate trunk elongation via tissue mechanics. *Curr Biol* **23**: 1335-41.
- Edelstein, Arthur, Nenad Amodaj, Karl Hoover, Ron Vale, and Nico Stuurman.** 2010. *Computer Control of Microscopes Using μ Manager* (John Wiley & Sons, Inc.).
- Edlund, M., M. A. Lotano, and C. A. Otey** (2001). Dynamics of alpha-actinin in focal adhesions and stress fibers visualized with alpha-actinin-green fluorescent protein. *Cell Motility and the Cytoskeleton* **48**: 190-200.
- Eisenhoffer, G. T., P. D. Loftus, M. Yoshigi, H. Otsuna, C. B. Chien, P. A. Morcos, and J. Rosenblatt** (2012). Crowding induces live cell extrusion to maintain homeostatic cell numbers in epithelia. *Nature* **484**: 546-9.
- Elul, T., M. A. Koehl, and R. Keller** (1997). Cellular mechanism underlying neural convergent extension in *Xenopus laevis* embryos. *Dev Biol* **191**: 243-58.
- Engler, Adam J, Shamik Sen, H Lee Sweeney, and Dennis E Discher** (2006). Matrix elasticity directs stem cell lineage specification. *Cell* **126**: 677-89.
- Esue, O., Y. Tseng, and D. Wirtz** (2009). Alpha-actinin and filamin cooperatively enhance the stiffness of actin filament networks. *PLoS One* **4**: e4411.
- Fagotto, F., N. Rohani, A. S. Touret, and R. Li** (2013). A molecular base for cell sorting at embryonic boundaries: contact inhibition of cadherin adhesion by ephrin/ Eph-dependent contractility. *Dev Cell* **27**: 72-87.

- Farhadifar, R., J. C. Roper, B. Aigouy, S. Eaton, and F. Julicher** (2007). The influence of cell mechanics, cell-cell interactions, and proliferation on epithelial packing. *Curr Biol* **17**: 2095-104.
- Fatehullah, Aliya, Si Hui Tan, and Nick Barker** (2016). Organoids as an in vitro model of human development and disease. *Nat Cell Biol* **18**: 246-54.
- Feroze, Rafey, Joseph H Shawky, Michelangelo von Dassow, and Lance A Davidson** (2015). Mechanics of blastopore closure during amphibian gastrulation. *Dev Biol* **398**: 57-67.
- Fey, Jeanette, and Peter Hausen** (1990). Appearance and distribution of laminin during development of *Xenopus laevis*. *Differentiation* **42**: 144-52.
- Filas, B. A., G. Xu, and L. A. Taber** (2015). Probing regional mechanical properties of embryonic tissue using microindentation and optical coherence tomography. *Methods Mol Biol* **1189**: 3-16.
- Findley, William N., James S. Lai, and Kasif Onaran.** 1976. *Creep and relaxation of nonlinear viscoelastic materials, with an introduction to linear viscoelasticity* (North-Holland Pub. Co. : sole distributors for the U.S.A. and Canada, Elsevier/North Holland: Amsterdam ; New York).
- Foty, R. A., C. M. Pflieger, G. Forgacs, and M. S. Steinberg** (1996). Surface tensions of embryonic tissues predict their mutual envelopment behavior. *Development* **122**: 1611-20.
- Foty, R. A., and M. S. Steinberg** (2005). The differential adhesion hypothesis: a direct evaluation. *Dev Biol* **278**: 255-63.
- Foty, R.A., G. Forgacs, C.M. Pflieger, and M.S. Steinberg** (1994). Liquid properties of embryonic tissues: measurement of interfacial tensions. *Physical Review Letters* **72**: 2298-301.
- Gardel, M. L., K. E. Kasza, C. P. Brangwynne, J. Liu, and D. A. Weitz** (2008). Chapter 19: Mechanical response of cytoskeletal networks. *Methods Cell Biol* **89**: 487-519.
- Gardel, M. L., I. C. Schneider, Y. Aratyn-Schaus, and C. M. Waterman** (2010). Mechanical integration of actin and adhesion dynamics in cell migration. *Annu Rev Cell Dev Biol* **26**: 315-33.
- Gardel, M. L., J. H. Shin, F. C. MacKintosh, L. Mahadevan, P. Matsudaira, and D. A. Weitz** (2004). Elastic behavior of cross-linked and bundled actin networks. *Science* **304**: 1301-5.

- Ghibaudo, Marion, Jean-Marc Di Meglio, Pascal Hersen, and Benoit Ladoux** (2011). Mechanics of cell spreading within 3D-micropatterned environments. *Lab Chip* **11**: 805-12.
- Gibson, L. J., and M. F. Ashby.** 1997. *Cellular solids: structure and properties*. (Cambridge University Press: New York).
- Gibson, Lorna J., and M. F. Ashby.** 1988. *Cellular solids : structure & properties* (Pergamon Press: Oxford Oxfordshire ; New York).
- Ginsberg, D., D. DeSimone, and B. Geiger** (1991). Expression of a novel cadherin (EP-cadherin) in unfertilized eggs and early *Xenopus* embryos. *Development* **111**: 315-25.
- Gong, J., D. Zhang, Y. Tseng, B. Li, D. Wirtz, and B. W. Schafer** (2013). Form-finding model shows how cytoskeleton network stiffness is realized. *PLoS One* **8**: e77417.
- Grashoff, Carsten, Brenton D Hoffman, Michael D Brenner, Ruobo Zhou, Maddy Parsons, Michael T Yang, Mark A McLean, Stephen G Sligar, Christopher S Chen, and Taekjip Ha** (2010). Measuring mechanical tension across vinculin reveals regulation of focal adhesion dynamics. *Nature* **466**: 263-66.
- Grooman, B., I. Fujiwara, C. Otey, and A. Upadhyaya** (2012). Morphology and viscoelasticity of actin networks formed with the mutually interacting crosslinkers: palladin and alpha-actinin. *PLoS One* **7**: e42773.
- Gumbiner, B. M.** (1996). Cell adhesion: the molecular basis of tissue architecture and morphogenesis. *Cell* **84**: 345-57.
- Hamill, O. P., and B. Martinac** (2001). Molecular basis of mechanotransduction in living cells. *Physiological Reviews* **81**: 685-740.
- Harris, A. K.** (1976). Is Cell sorting caused by differences in the work of intercellular adhesion? A critique of the Steinberg hypothesis. *J Theor Biol* **61**: 267-85.
- Harris, William A., and Volker Hartenstein** (1991). Neuronal determination without cell division in *xenopus* embryos. *Neuron* **6**: 499-515.
- Hayashi, T., and R. W. Carthew** (2004). Surface mechanics mediate pattern formation in the developing retina. *Nature* **431**: 647-52.
- Heasman, J., D. Ginsberg, B. Geiger, K. Goldstone, T. Pratt, C. Yoshida-Noro, and C. Wylie** (1994). A functional test for maternally inherited cadherin in *Xenopus* shows its importance in cell adhesion at the blastula stage. *Development* **120**: 49-57.

- Hilgenfeldt, S., S. Erisken, and R. W. Carthew** (2008). Physical modeling of cell geometric order in an epithelial tissue. *Proc Natl Acad Sci U S A* **105**: 907-11.
- Holtfreter, J.** (1934). *Wilhelm Roux Arch Entwickl Mech Org* **132**: 225-306.
- Holtfreter, J.** (1939). *Wilhelm Roux Arch Entwickl Mech Org* **139**: 110-90.
- Huveneers, S., and E. H. Danen** (2009). Adhesion signaling - crosstalk between integrins, Src and Rho. *J Cell Sci* **122**: 1059-69.
- Jackson, T. R., H. Y. Kim, U. L. Balakrishnan, C. Stuckenholtz, and L. A. Davidson** (2017). Spatiotemporally controlled mechanical cues drive progenitor mesenchymal-to-epithelial transition enabling proper heart formation and function. *Current Biology*.
- Janmey, P. A., and C. A. McCulloch** (2007). Cell mechanics: integrating cell responses to mechanical stimuli. *Annu Rev Biomed Eng* **9**: 1-34.
- Jones, D. Leanne, and Amy J. Wagers** (2008). No place like home: anatomy and function of the stem cell niche. *Nat Rev Mol Cell Biol* **9**: 11-21.
- Joshi, S. D., M. von Dassow, and L. A. Davidson** (2010). Experimental control of excitable embryonic tissues: three stimuli induce rapid epithelial contraction. *Exp Cell Res* **316**: 103-14.
- Kafer, J., T. Hayashi, A. F. Maree, R. W. Carthew, and F. Graner** (2007). Cell adhesion and cortex contractility determine cell patterning in the Drosophila retina. *Proc Natl Acad Sci U S A* **104**: 18549-54.
- Kalantarian, A., H. Ninomiya, S. M. Saad, R. David, R. Winklbauer, and A. W. Neumann** (2009). Axisymmetric drop shape analysis for estimating the surface tension of cell aggregates by centrifugation. *Biophys J* **96**: 1606-16.
- Kasza, K. E., C. P. Broedersz, G. H. Koenderink, Y. C. Lin, W. Messner, E. A. Millman, F. Nakamura, T. P. Stossel, F. C. Mackintosh, and D. A. Weitz** (2010). Actin filament length tunes elasticity of flexibly cross-linked actin networks. *Biophys J* **99**: 1091-100.
- Kasza, K. E., and J. A. Zallen** (2011). Dynamics and regulation of contractile actin-myosin networks in morphogenesis. *Curr Opin Cell Biol* **23**: 30-8.
- Kato, K., and J. B. Gurdon** (1993). Single-cell transplantation determines the time when *Xenopus* muscle precursor cells acquire a capacity for autonomous differentiation. *Proc Natl Acad Sci U S A* **90**: 1310-4.

- Kay, B. K. and Peng, H. B.** . 1991. *Xenopus laevis: Practical Uses in Cell and Molecular Biology*. (Academic Press: New York).
- Keller, R.** (2000). The origin and morphogenesis of amphibian somites. *Curr Top Dev Biol* **47**: 183-246.
- Keller, R., and M. Danilchik** (1988). Regional expression, pattern and timing of convergence and extension during gastrulation of *Xenopus laevis*. *Development* **103**: 193-209.
- Keller, Ray, Lance A. Davidson, and David R. Shook** (2003). How we are shaped: The biomechanics of gastrulation. *Differentiation* **71**: 171-205.
- Kim, Kyung Suk, and N Aravas** (1988). Elastoplastic analysis of the peel test. *International Journal of Solids and Structures* **24**: 417-35.
- Kim, T., W. Hwang, H. Lee, and R. D. Kamm** (2009). Computational analysis of viscoelastic properties of crosslinked actin networks. *PLoS Comput Biol* **5**: e1000439.
- Kim, YongTae, Melis Hazar, Deepthi S Vijayraghavan, Jiho Song, Timothy R Jackson, Sagar D Joshi, William C Messner, Lance A Davidson, and Philip R LeDuc** (2014). Mechanochemical actuators of embryonic epithelial contractility. *Proc. Natl. Acad. Sci.* **111**: 14366-71.
- Kintner, C. R., and J. P. Brookes** (1984). Monoclonal antibodies identify blastemal cells derived from dedifferentiating limb regeneration. *Nature* **308**: 67-9.
- Koehl, M. A.** (1990). Biomechanical approaches to morphogenesis. *seminars in Developmental Biology* **1**: 367-78.
- Koehl, M. A. R., K. J. Quillin, and C. A. Pell** (2000). Mechanical design of fiber-wound hydraulic skeletons: The stiffening and straightening of embryonic notochords. *American Zoologist* **40**: 28-41.
- Kovacs, E. M., S. Verma, R. G. Ali, A. Ratheesh, N. A. Hamilton, A. Akhmanova, and A. S. Yap** (2011). N-WASP regulates the epithelial junctional actin cytoskeleton through a non-canonical post-nucleation pathway. *Nat Cell Biol* **13**: 934-43.
- Krens, S. F., S. Mollmert, and C. P. Heisenberg** (2011). Enveloping cell-layer differentiation at the surface of zebrafish germ-layer tissue explants. *Proc Natl Acad Sci U S A* **108**: E9-10; author reply E11.

- Krieg, M., Y. Arboleda-Estudillo, P. H. Puech, J. Kafer, F. Graner, D. J. Muller, and C. P. Heisenberg** (2008). Tensile forces govern germ-layer organization in zebrafish. *Nat Cell Biol* **10**: 429-36.
- Kunda, P., A. E. Pelling, T. Liu, and B. Baum** (2008). Moesin controls cortical rigidity, cell rounding, and spindle morphogenesis during mitosis. *Curr Biol* **18**: 91-101.
- Lauffenburger, Douglas A, and Alan F Horwitz** (1996). Cell migration: a physically integrated molecular process. *Cell* **84**: 359-69.
- Lawton, A. K., A. Nandi, M. J. Stulberg, N. Dray, M. W. Sneddon, W. Pontius, T. Emonet, and S. A. Holley** (2013). Regulated tissue fluidity steers zebrafish body elongation. *Development* **140**: 573-82.
- Lecuit, T., and L. Le Goff** (2007). Orchestrating size and shape during morphogenesis. *Nature* **450**: 189-92.
- Lee, Sung Haeng, and Roberto Dominguez** (2010). Regulation of Actin Cytoskeleton Dynamics in Cells. *Molecules and cells* **29**: 311-25.
- Leise, W., 3rd, and P. R. Mueller** (2002). Multiple Cdk1 inhibitory kinases regulate the cell cycle during development. *Dev Biol* **249**: 156-73.
- Leise, Walter F., III, and Paul R. Mueller** (2004). Inhibition of the Cell Cycle is required for convergent extension of the paraxial medoderm during *Xenopus* neurulation. *Development* **131**: 1703-15.
- Levayer, R., and T. Lecuit** (2013). Oscillation and polarity of E-cadherin asymmetries control actomyosin flow patterns during morphogenesis. *Dev Cell* **26**: 162-75.
- Litvinov, R. I., H. Shuman, J. S. Bennett, and J. W. Weisel** (2002). Binding strength and activation state of single fibrinogen-integrin pairs on living cells. *Proc Natl Acad Sci U S A* **99**: 7426-31.
- Liu, Z., J. L. Tan, D. M. Cohen, M. T. Yang, N. J. Sniadecki, S. A. Ruiz, C. M. Nelson, and C. S. Chen** (2010). Mechanical tugging force regulates the size of cell-cell junctions. *Proc Natl Acad Sci U S A* **107**: 9944-9.
- Lodish, Harvey, Arnold Berk, S Lawrence Zipursky, Paul Matsudaira, David Baltimore, and James Darnell** (2000). The actin cytoskeleton.
- Loring, J. F., and C. A. Erickson** (1987). Neural crest cell migratory pathways in the trunk of the chick embryo. *Dev Biol* **121**: 220-36.

- Low, S. H., S. Mukhina, V. Srinivas, C. Z. Ng, and M. Murata-Hori** (2010). Domain analysis of alpha-actinin reveals new aspects of its association with F-actin during cytokinesis. *Exp Cell Res* **316**: 1925-34.
- Luan, Y., O. Lieleg, B. Wagner, and A. R. Bausch** (2008). Micro- and macrorheological properties of isotropically cross-linked actin networks. *Biophys J* **94**: 688-93.
- Luu, O., R. David, H. Ninomiya, and R. Winklbauer** (2011). Large-scale mechanical properties of *Xenopus* embryonic epithelium. *Proc Natl Acad Sci U S A* **108**: 4000-5.
- Maitre, J. L., H. Berthoumieux, S. F. Krens, G. Salbreux, F. Julicher, E. Paluch, and C. P. Heisenberg** (2012). Adhesion functions in cell sorting by mechanically coupling the cortices of adhering cells. *Science* **338**: 253-6.
- Manning, M. L., R. A. Foty, M. S. Steinberg, and E. M. Schoetz** (2010). Coaction of intercellular adhesion and cortical tension specifies tissue surface tension. *Proc Natl Acad Sci U S A* **107**: 12517-22.
- Marheineke, K., and O. Hyrien** (2001). Aphidicolin triggers a block to replication origin firing in *Xenopus* egg extracts. *J Biol Chem* **276**: 17092-100.
- Maruthamuthu, V., Y. Aratyn-Schaus, and M. L. Gardel** (2010). Conserved F-actin dynamics and force transmission at cell adhesions. *Curr Opin Cell Biol* **22**: 583-8.
- Maruthamuthu, V., B. Sabass, U. S. Schwarz, and M. L. Gardel** (2011). Cell-ECM traction force modulates endogenous tension at cell-cell contacts. *Proc Natl Acad Sci U S A* **108**: 4708-13.
- Miller, Callie Johnson, and Lance Davidson** (2013). The interplay between cell signaling and mechanics in developmental processes. *Nat Rev Genet* **14**: 733.
- Mohr, Jeffrey C, Juan J de Pablo, and Sean P Palecek** (2006). 3-D microwell culture of human embryonic stem cells. *Biomater.* **27**: 6032-42.
- Moore, S. W., R. E. Keller, and M. A. Koehl** (1995). The dorsal involuting marginal zone stiffens anisotropically during its convergent extension in the gastrula of *Xenopus laevis*. *Development* **121**: 3131-40.
- Mukhina, S., Y. L. Wang, and M. Murata-Hori** (2007). Alpha-actinin is required for tightly regulated remodeling of the actin cortical network during cytokinesis. *Dev Cell* **13**: 554-65.

- Mullins, R Dyche, John A Heuser, and Thomas D Pollard** (1998). The interaction of Arp2/3 complex with actin: nucleation, high affinity pointed end capping, and formation of branching networks of filaments. *Proceedings of the National Academy of Sciences* **95**: 6181-86.
- Murakami, F., Y. Ando, A. Miyagi, S. Sugita, N. Ueno, and T. Matsumoto** (2017). Measurement of surface topography and stiffness distribution on cross-section of *Xenopus laevis* tailbud for estimation of mechanical environment in embryo. *Dev Growth Differ* **59**: 434-43.
- Murphy, William L., Todd C. McDevitt, and Adam J. Engler** (2014). Materials as stem cell regulators. *Nat Mater* **13**: 547-57.
- Nandadasa, S., Q. Tao, N. R. Menon, J. Heasman, and C. Wylie** (2009). N- and E-cadherins in *Xenopus* are specifically required in the neural and non-neural ectoderm, respectively, for F-actin assembly and morphogenetic movements. *Development* **136**: 1327-38.
- Nemer, M.** (2008). Genetic insights into normal and abnormal heart development. *Cardiovasc Pathol* **17**: 48-54.
- Nerurkar, Nandan L, L Mahadevan, and Clifford J Tabin** (2017). BMP signaling controls buckling forces to modulate looping morphogenesis of the gut. *Proceedings of the National Academy of Sciences* **114**: 2277-82.
- Nieuwkoop, P. D. and Faber, J.** 1967. *Normal tables of Xenopus laevis (Daudin)* (Elsevier North-Holland Biomedical Press: Amsterdam).
- Ninomiya, H., R. David, E. W. Damm, F. Fagotto, C. M. Niessen, and R. Winklbauer** (2012). Cadherin-dependent differential cell adhesion in *Xenopus* causes cell sorting in vitro but not in the embryo. *J Cell Sci* **125**: 1877-83.
- Odell, G. M., G. Oster, P. Alberch, and B. Burnside** (1981). The mechanical basis of morphogenesis. I. Epithelial folding and invagination. *Dev Biol* **85**: 446-62.
- Paluch, E., and C. P. Heisenberg** (2009). Biology and physics of cell shape changes in development. *Curr Biol* **19**: R790-9.
- Pan, Y., I. Heemskerk, C. Ibar, B. I. Shraiman, and K. D. Irvine** (2016). Differential growth triggers mechanical feedback that elevates Hippo signaling. *Proc Natl Acad Sci U S A*.
- Papan, C., and J. A. Camposortega** (1994). On the Formation of the Neural Keel and Neural-Tube in the Zebrafish *Danio (Brachydanio) Rerio*. *Roux's Archives of Developmental Biology* **203**: 178-86.

- Parsons, J. T., A. R. Horwitz, and M. A. Schwartz** (2010). Cell adhesion: integrating cytoskeletal dynamics and cellular tension. *Nat Rev Mol Cell Biol* **11**: 633-43.
- Perret, E., A. Leung, H. Feracci, and E. Evans** (2004). Trans-bonded pairs of E-cadherin exhibit a remarkable hierarchy of mechanical strengths. *Proc Natl Acad Sci U S A* **101**: 16472-7.
- Popov, I. K., T. Kwon, D. K. Crossman, M. R. Crowley, J. B. Wallingford, and C. Chang** (2017). Identification of new regulators of embryonic patterning and morphogenesis in *Xenopus* gastrulae by RNA sequencing. *Dev Biol* **426**: 429-41.
- Puech, P. H., A. Taubenberger, F. Ulrich, M. Krieg, D. J. Muller, and C. P. Heisenberg** (2005). Measuring cell adhesion forces of primary gastrulating cells from zebrafish using atomic force microscopy. *J Cell Sci* **118**: 4199-206.
- Rauzi, M., U. Krzic, T. E. Saunders, M. Krajnc, P. Zihler, L. Hufnagel, and M. Leptin** (2015). Embryo-scale tissue mechanics during *Drosophila* gastrulation movements. *Nat Commun* **6**: 8677.
- Riedl, J., A. H. Crevenna, K. Kessenbrock, J. H. Yu, D. Neukirchen, M. Bista, F. Bradke, D. Jenne, T. A. Holak, Z. Werb, M. Sixt, and R. Wedlich-Soldner** (2008). Lifeact: a versatile marker to visualize F-actin. *Nat Methods* **5**: 605-7.
- Rivero, F., R. Furukawa, M. Fechheimer, and A. A. Noegel** (1999). Three actin cross-linking proteins, the 34 kDa actin-bundling protein, alpha-actinin and gelation factor (ABP-120), have both unique and redundant roles in the growth and development of *Dictyostelium*. *J Cell Sci* **112** (Pt **16**): 2737-51.
- Rossier, O.M., N. Gauthier, N. Biais, W. Vonnegut, M.A. Fardin, P. Avigan, E.R. Heller, A. Mathur, S. Ghassemi, and M.S. Koeckert** (2010). Force generated by actomyosin contraction builds bridges between adhesive contacts. *EMBO J.* **29**: 1055-68.
- Rozario, T., B. Dzamba, G.F. Weber, L. A. Davidson, and D. W. DeSimone** (2009). The physical state of fibronectin matrix differentially regulates morphogenetic movements in vivo. *Developmental biology* **327**: 386-98.
- Ruoslahti, E., and M. D. Pierschbacher** (1987). New perspectives in cell adhesion: RGD and integrins. *Science* **238**: 491-7.
- Saeger, John, Vesa P Hytönen, Enrico Klotzsch, and Viola Vogel** (2012). GFP's mechanical intermediate states. *PLoS One* **7**: e46962.

- Saka, Y., and J. C. Smith** (2001). Spatial and temporal patterns of cell division during early *Xenopus* embryogenesis. *Dev Biol* **229**: 307-18.
- Savin, T., N. A. Kurpios, A. E. Shyer, P. Florescu, H. Liang, L. Mahadevan, and C. J. Tabin** (2011). On the growth and form of the gut. *Nature* **476**: 57-62.
- Schotz, E. M., R. D. Burdine, F. Julicher, M. S. Steinberg, C. P. Heisenberg, and R. A. Foty** (2008). Quantitative differences in tissue surface tension influence zebrafish germ layer positioning. *HFSP J* **2**: 42-56.
- Selman, G.G.** (1955). Studies on the forces producing neural closure in amphibia. *Proceedings of the Royal Physical Society of Edinburgh* **24**: 24-27.
- Selman, G.G.** (1958). The forces producing neural closure in amphibia. *Journal of Embryology and Experimental Morphology* **6**: 448-65.
- Session, A. M., Y. Uno, T. Kwon, J. A. Chapman, A. Toyoda, S. Takahashi, A. Fukui, A. Hikosaka, A. Suzuki, M. Kondo, S. J. van Heeringen, I. Quigley, S. Heinz, H. Ogino, H. Ochi, U. Hellsten, J. B. Lyons, O. Simakov, N. Putnam, J. Stites, Y. Kuroki, T. Tanaka, T. Michiue, M. Watanabe, O. Bogdanovic, R. Lister, G. Georgiou, S. S. Paranjpe, I. van Kruijsbergen, S. Shu, J. Carlson, T. Kinoshita, Y. Ohta, S. Mawaribuchi, J. Jenkins, J. Grimwood, J. Schmutz, T. Mitros, S. V. Mozaffari, Y. Suzuki, Y. Haramoto, T. S. Yamamoto, C. Takagi, R. Heald, K. Miller, C. Haudenschild, J. Kitzman, T. Nakayama, Y. Izutsu, J. Robert, J. Fortriede, K. Burns, V. Lotay, K. Karimi, Y. Yasuoka, D. S. Dichmann, M. F. Flajnik, D. W. Houston, J. Shendure, L. DuPasquier, P. D. Vize, A. M. Zorn, M. Ito, E. M. Marcotte, J. B. Wallingford, Y. Ito, M. Asashima, N. Ueno, Y. Matsuda, G. J. Veenstra, A. Fujiyama, R. M. Harland, M. Taira, and D. S. Rokhsar** (2016). Genome evolution in the allotetraploid frog *Xenopus laevis*. *Nature* **538**: 336-43.
- Shawky, J. H., and L. A. Davidson** (2015). Tissue mechanics and adhesion during embryo development. *Dev Biol* **401**: 152-64.
- Shewan, A. M., M. Maddugoda, A. Kraemer, S. J. Stehbens, S. Verma, E. M. Kovacs, and A. S. Yap** (2005). Myosin 2 is a key Rho kinase target necessary for the local concentration of E-cadherin at cell-cell contacts. *Molecular Biology of the Cell* **16**: 4531-42.
- Shih, J., and R. Keller** (1992a). Cell motility driving mediolateral intercalation in explants of *Xenopus laevis*. *Development* **116**: 901-14.
- Shih, J., and R. Keller** (1992b). Patterns of cell motility in the organizer and dorsal mesoderm of *Xenopus laevis*. *Development* **116**: 915-30.

- Shin, J. H., M. L. Gardel, L. Mahadevan, P. Matsudaira, and D. A. Weitz** (2004). Relating microstructure to rheology of a bundled and cross-linked F-actin network in vitro. *Proc Natl Acad Sci U S A* **101**: 9636-41.
- Shraiman, B. I.** (2005). Mechanical feedback as a possible regulator of tissue growth. *Proc Natl Acad Sci U S A* **102**: 3318-23.
- Shyer, Amy E, Tyler R Huycke, ChangHee Lee, L Mahadevan, and Clifford J Tabin** (2015). Bending gradients: how the intestinal stem cell gets its home. *Cell* **161**: 569-80.
- Sit, S. T., and E. Manser** (2011). Rho GTPases and their role in organizing the actin cytoskeleton. *J Cell Sci* **124**: 679-83.
- Sivasankar, S., W. Briehner, N. Lavrik, B. Gumbiner, and D. Leckband** (1999). Direct molecular force measurements of multiple adhesive interactions between cadherin ectodomains. *Proc Natl Acad Sci U S A* **96**: 11820-4.
- Skoglund, P., B. Dzamba, C. R. Coffman, W. A. Harris, and R. Keller** (2006). Xenopus fibrillin is expressed in the organizer and is the earliest component of matrix at the developing notochord-somite boundary. *Developmental Dynamics* **235**: 1974-83.
- Song, Jiho, Joseph H. Shawky, YongTae Kim, Melis Hazar, Philip R. LeDuc, Metin Sitti, and Lance A. Davidson** (2015). Controlled Surface Topography regulates Collective 3D Migration by Epithelial-Mesenchymal Composite Embryonic Tissues. *Biomaterials* **58**: 1-9.
- Steinberg, M. S.** (1963). Reconstruction of tissues by dissociated cells. Some morphogenetic tissue movements and the sorting out of embryonic cells may have a common explanation. *Science* **141**: 401-8.
- Steinberg, M. S.** (1970). Does differential adhesion govern self-assembly processes in histogenesis? Equilibrium configurations and the emergence of a hierarchy among populations of embryonic cells. *J Exp Zool* **173**: 395-433.
- Steinberg, M. S., and M. Takeichi** (1994). Experimental specification of cell sorting, tissue spreading, and specific spatial patterning by quantitative differences in cadherin expression. *Proc Natl Acad Sci U S A* **91**: 206-9.
- Stemple, D. L.** (2005). Structure and function of the notochord: an essential organ for chordate development. *Development* **132**: 2503-12.

- Stossel, TP, C Chaponnier, RM Ezzell, JH Hartwig, PA Janmey, DJ Kwiatkowski, SE Lind, DB Smith, FS Southwick, and HL Yin** (1985). Nonmuscle actin-binding proteins. *Annual review of cell biology* **1**: 353-402.
- Taber, L. A., D. A. Voronov, and A. Ramasubramanian** (2010). The role of mechanical forces in the torsional component of cardiac looping. *Ann N Y Acad Sci* **1188**: 103-10.
- Takeichi, M.** (1988). The cadherins: cell-cell adhesion molecules controlling animal morphogenesis. *Development* **102**: 639-55.
- Tao, Q., S. Nandadasa, P. D. McCrea, J. Heasman, and C. Wylie** (2007). G-protein-coupled signals control cortical actin assembly by controlling cadherin expression in the early *Xenopus* embryo. *Development* **134**: 2651-61.
- Teixeira, Ana I, George A Abrams, Paul J Bertics, Christopher J Murphy, and Paul F Nealey** (2003). Epithelial contact guidance on well-defined micro- and nanostructured substrates. *J. of Cell Sci.* **116**: 1881-92.
- Thompson, R. E., D. R. Larson, and W. W. Webb** (2002). Precise nanometer localization analysis for individual fluorescent probes. *Biophys J* **82**: 2775-83.
- Townes, Philip L., and Johannes Holtfreter** (1955). Directed movements and selective adhesion of embryonic amphibian cells. *Journal of Experimental Zoology* **128**: 53-120.
- Trinkaus, J. P.** (1973). Surface activity and locomotion of *Fundulus* deep cells during blastula and gastrula stages. *Dev Biol* **30**: 68-103.
- Tseng, Y., B. W. Schafer, S. C. Almo, and D. Wirtz** (2002). Functional synergy of actin filament cross-linking proteins. *J Biol Chem* **277**: 25609-16.
- Valiev, Ruslan Z, NA Krasilnikov, and NK Tsenev** (1991). Plastic deformation of alloys with submicron-grained structure. *Materials Science and Engineering: A* **137**: 35-40.
- Varner, V. D., D. A. Voronov, and L. A. Taber** (2010). Mechanics of head fold formation: investigating tissue-level forces during early development. *Development* **137**: 3801-11.
- Vijayraghavan, D. S., and L. A. Davidson** (2016). Mechanics of neurulation: from classical to current perspectives on the physical mechanics that shape, fold, and form the neural tube. *Birth Defects Res A Clin Mol Teratol*.
- von Dassow, M., and L. A. Davidson** (2009). Natural variation in embryo mechanics: gastrulation in *Xenopus laevis* is highly robust to variation in tissue stiffness. *Dev Dyn* **238**: 2-18.

- Wachsstock, D. H., W. H. Schwarz, and T. D. Pollard** (1994). Cross-linker dynamics determine the mechanical properties of actin gels. *Biophys J* **66**: 801-9.
- Wagner, B., R. Tharmann, I. Haase, M. Fischer, and A. R. Bausch** (2006). Cytoskeletal polymer networks: the molecular structure of cross-linkers determines macroscopic properties. *Proc Natl Acad Sci U S A* **103**: 13974-8.
- Weaire, Denis L, and Stefan Hutzler**. 2001. *The physics of foams* (Oxford University Press).
- Weber, G. F., M. A. Bjerke, and D. W. DeSimone** (2011). Integrins and cadherins join forces to form adhesive networks. *J Cell Sci* **124**: 1183-93.
- Wiebe, C., and G. W. Brodland** (2005). Tensile properties of embryonic epithelia measured using a novel instrument. *J Biomech* **38**: 2087-94.
- Wilson, HV** (1907). On some phenomena of coalescence and regeneration in sponges. *Journal of Experimental Zoology Part A: Ecological Genetics and Physiology* **5**: 245-58.
- Wilson, P., and R. Keller** (1991). Cell rearrangement during gastrulation of *Xenopus*: direct observation of cultured explants. *Development* **112**: 289-300.
- Winklbauer, R.** (1990). Mesodermal cell migration during *Xenopus* gastrulation. *Dev Biol* **142**: 155-68.
- Xu, J., Y. Tseng, and D. Wirtz** (2000). Strain hardening of actin filament networks. Regulation by the dynamic cross-linking protein alpha-actinin. *J Biol Chem* **275**: 35886-92.
- Xu, J., D. Wirtz, and T. D. Pollard** (1998). Dynamic cross-linking by alpha-actinin determines the mechanical properties of actin filament networks. *J Biol Chem* **273**: 9570-6.
- Zamir, E. A., and L. A. Taber** (2004). Material properties and residual stress in the stage 12 chick heart during cardiac looping. *J Biomech Eng* **126**: 823-30.
- Zhou, J, H. Y. Kim, and L. A. Davidson** (2009). Actomyosin stiffens the vertebrate embryo during critical stages of elongation and neural tube closure. *Development* **136**: 677-88.
- Zhou, J., H. Y. Kim, J. H. Wang, and L. A. Davidson** (2010). Macroscopic stiffening of embryonic tissues via microtubules, RhoGEF and the assembly of contractile bundles of actomyosin. *Development* **137**: 2785-94.
- Zhou, J., S. Pal, S. Maiti, and L. A. Davidson** (2015). Force production and mechanical accommodation during convergent extension. *Development* **142**: 692-701.

Zhu, C., G. Bao, and N. Wang (2000). Cell mechanics: mechanical response, cell adhesion, and molecular deformation. *Annu Rev Biomed Eng* **2**: 189-226.